SYNTHESIS AND CHARACTERIZATION OF PATTERNED SURFACES AND CATALYTICALLY RELEVANT BINARY NANOCRYSTALLINE INTERMETALLIC COMPOUNDS

A Dissertation

by

ROBERT E. CABLE

Submitted to the Office of Graduate Studies of
Texas A&M University
in partial fulfillment of the requirements for the degree of

DOCTOR OF PHILOSOPHY

December 2007

Major Subject: Chemistry

SYNTHESIS AND CHARACTERIZATION OF PATTERNED SURFACES AND CATALYTICALLY RELEVANT BINARY NANOCRYSTALLINE INTERMETALLIC COMPOUNDS

A Dissertation

by

ROBERT E. CABLE

Submitted to the Office of Graduate Studies of
Texas A&M University
in partial fulfillment of the requirements for the degree of

DOCTOR OF PHILOSOPHY

Approved by:

Co-Chairs of Committee,	Raymond E. Schaak
	James D. Batteas
Committee Members,	Kim R. Dunbar
	Daniel F. Shantz
Head of Department,	David H. Russell

December 2007

Major Subject: Chemistry

ABSTRACT

Synthesis and Characterization of Patterned Surfaces and Catalytically
Relevant Binary Nanocrystalline Intermetallic Compounds.

(December 2007)

Robert E. Cable, B.A., Knox College

Co-Chairs of Advisory Committee: Dr. Raymond E. Schaak
Dr. James D. Batteas

As devices and new technologies continue to shrink, nanocrystalline multi-metal compounds are becoming increasingly important for high efficiency and multifunctionality. However, synthetic methods to make desirable nanocrystalline multi-metallics are not yet matured. In response to this deficiency, we have developed several solution-based methods to synthesize nanocrystalline binary alloy and intermetallic compounds. This dissertation describes the processes we have developed, as well as our investigations into the use of lithographically patterned surfaces for template-directed self-assembly of solution dispersible colloids.

We used a modified polyol process to synthesize nanocrystalline intermetallics of late transition and main-group metals in the *M*-Sn, Pt-*M*’, and Co-Sb systems. These compounds are known to have interesting physical properties and as nanocrystalline materials they may be useful for magnetic, thermoelectric, and catalytic applications. While the polyol method is quite general, it is limited to metals that are somewhat easy to reduce. Accordingly, we focused our synthetic efforts on intermetallics comprised of highly electropositive metals. We find that we can react single-metal nanoparticles with zero-valent organometallic Zinc reagents in hot, coordinating amine solvents via a thermal decomposition process to form several intermetallics in the *M''*-Zn system. Characterization of the single-metal intermediates and final intermetallic products shows a general retention of morphology throughout the reaction, and changes in optical properties are also observed. Following this principle of conversion chemistry, we can employ the high reactivity of nanocrystals to reversibly convert between intermetallic phases within the Pt-Sn system, where $PtSn_2 \leftrightarrow PtSn \leftrightarrow Pt_3Sn$. Our conversion chemistry occurs in solution at temperatures below 300 °C and within 1 hour, highlighting the high reactivity of our nanocrystalline materials compared to the bulk. Some evidence of the generality for this process is also presented.

Our nanocrystalline powders are dispersible in solution, and as such are amenable to solution-based processing techniques developed for colloidal dispersions. Accordingly, we have investigated the use of lithographically patterned surfaces to control the self-assembly of colloidal particles. We find that we can rapidly crystallize 2-dimensional building blocks, as well as use epitaxial templates to direct the formation of interesting superlattice structures comprised of a bidisperse population of particles.

ACKNOWLEDGEMENTS

I would like to thank my research advisor, Dr. Raymond Schaak, for enthusiastically mentoring and teaching me over the last four years, as well as for his support. I would also like to thank my committee members, Dr. Batteas, Dr. Dunbar, Dr. Goodman, and Dr. Shantz for the help and advice they have provided. Other Texas A&M Chemistry faculty (past and present) I would like to thank include Dr. Clearfield, Dr. Crooks, Dr. D. Darensbourg, Dr. Gabbai, Dr. Hall, and Dr. Hughbanks. In addition, I would like to thank Dr. Nattamai Bhuvanesh and Dr. William Lackowski for sharing their respective expertise during my studies.

Many thanks go to the members of the Schaak research group for their help over the years. I would also like to individually thank Dr. Mason Haneline, Brian Leonard, Nam Hwan Chou, Dr. Lindsay Roy, Nathan Henderson, and Farah Dawood, for their help, advice, and friendship.

I would like to thank my Chemistry professors at Knox College for their mentoring and teaching. In particular, I would like to thank Dr. Linda Bush for her advice, support, and encouragement.

I would like to express my most sincere love and appreciation for Mary, my best friend and future wife, for her constant love, support, and understanding through the good times and bad, and for inspiring me to slow down and enjoy life.

I would like to thank my family for all their love, support, and encouragement throughout the years, without which I would not be where I am today. Thank you!

Additional thanks go to the tradition of the Samuels family of Loretto, KY.

TABLE OF CONTENTS

Page

CHAPTER

LIST OF FIGURES

FIGURE Page

FIGURE Page

FIGURE Page

FIGURE Page

LIST OF TABLES

CHAPTER I

INTRODUCTION*

The search for new technologies, energy sources, and smaller, more efficient devices is driving a major research effort focused on the synthesis and controlled assembly of micro and nanoparticulate materials. In particular, the synthesis of inorganic nanomaterials desired for specific applications can be very complicated, as their physical and chemical properties are dependent upon many physical and chemical parameters such as composition,[1] crystal structure,[2-4] particle size,[5] and particle morphology,[6] all of which need to be controlled during synthesis to accurately control material properties. Furthermore, as nanomaterials are integrated into devices, the nano- or micro-structure of assembled particles can affect the bulk properties of a device such as its efficiency, property strength, and durability.[7] For example, colloidal crystals (extended solids of spherical particles with a repeating packing order) are of high interest for optoelectronic applications, and both crystal structure and particle composition highly influence the overall optical properties of the crystal.[8] If being used as catalysts,

---

This dissertation follows the style and format of the *Journal of the American Chemical Society.*

* Reprinted in part with permission from *J. Am. Chem. Soc., 127* Schaak, R. E.; Sra, A. K.; Leonard, B. M.; Cable, R. E.; Bauer, J. C.; Han, Y.-F.; Means, J.; Teizer, W.; Vasquez, Y.; Funck, E. S. "Metallurgy in a Beaker: Nanoparticle Toolkit for the Rapid Low-Temperature Solution Synthesis of Functional Multimetallic Solid-State Materials," 3506, Copyright 2005 by the American Chemical Society.

the composition,[9] crystal structure[4] and surface chemistry[10] of nanomaterials are critically important, however their morphology[11] and interactions with a catalyst support[12] can have a profound impact on catalytic activity as well. Accordingly, robust and general methods are required for the synthesis and assembly or supporting of nanomaterials.

Many methods have been developed that successfully access inorganic nanomaterials. These methods can be broadly classified as either top-down approaches, involving the fractionating of bulk materials, or bottom-up approaches, involving the growth of nanomaterials from atomic-scale components. Generally, top-down approaches involve mechanical grinding[13,14] or a high-energy process such as laser ablation of bulk materials.[15] These approaches can require long reaction times and/or high energy input, and while they may allow for control over size of the final product, there is generally little control over other important physical and chemical parameters such as product composition, crystal structure, and particle morphology. Alternatively, bottom-up approaches can allow for greater control over multiple physical parameters of the final products. These approaches include vapor-phase routes such as chemical vapor deposition (CVD),[16] sputtering,[17] and molecular beam epitaxy,[18] or soft wet-chemical routes such as sol-gel,[19,20] hydrothermal[21,22] and colloidal synthesis.[1,2,3,5-7,10] The bottom-up approaches have been well studied and developed for semiconductor,[7,18] metal oxide,[23,24] and single-metal nanomaterials.[6,10,11] Multi-metallic alloys and intermetallics exhibit very useful physical and chemical properties, yet methods which access them as nanomaterials have been largely limited to top-down approaches until fairly recently.

Alloys and intermetallic compounds have long been linked to technological development due to their wide range of properties from the relatively simple, such as structural strength and corrosion resistance,[25] to more advanced properties such as ferromagnetism,[2,3] thermoelectricity,[14,26,27] shape-memory,[28] superconductivity,[29] solid-state hydrogen storage,[30] and high catalytic activity.[4] More interestingly, atomically ordered intermetallics often exhibit enhanced physical or chemical properties in comparison to their atomically disordered alloy analog, which may be though of as metal solid solutions. Examples include FePt, which exhibits paramagnetism as a face-centered cubic (fcc) alloy and ferromagnetism as a face-centered tetragonal (fct) ordered intermetallic (Figure 1.1),[2,3] and PtBi, which in its intermetallic structure exhibits electrocatalytic activity superior to pure Pt, and unlike pure Pt is virtually immune to CO poisoning (Figure 1.2).[4] While the atomically ordered crystal structure plays a fundamental role in the enhanced properties of intermetallics, compositions of intermetallic phases generally have fixed atomic ratios that may vary over a narrow range, and as a result tailoring the properties of intermetallics by composition control is not always feasible. However, as nanometer-scale materials, the properties of intermetallics may be further tailored by controlling particle size and morphology.[27,31]

Traditional solid-state metallurgical synthesis of alloys and intermetallics initially involves high temperature processing, such as arc-melting or heating to temperatures in excess of 1000 °C, in order to melt the constituent elemental powders

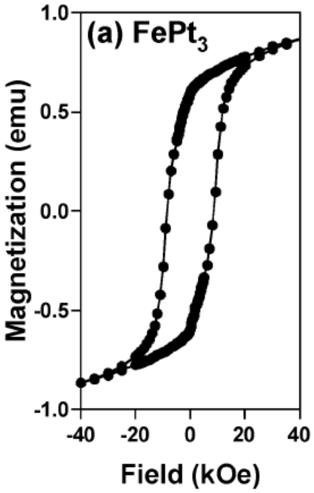

Figure 1.1 Hysteresis loop with a coercivity of 8000 Oe at 10 K for a sample of $FePt_3$ synthesized as a nanocomposite, then thermally annealed at 600 °C for 60 min. (Source: Schaak, *et al.*, 2005)

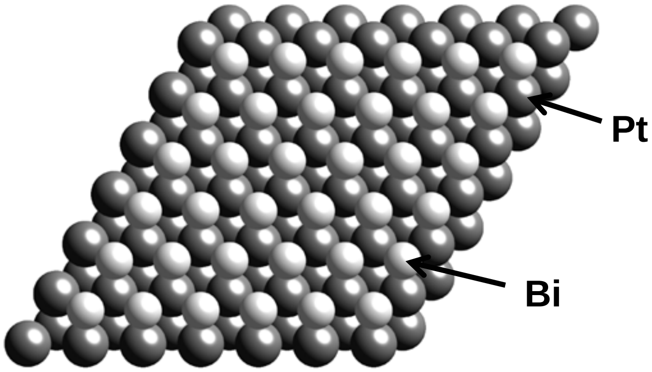

Figure 1.2 PtBi intermetallic structure as viewed from the (001) plane. The large, dark atoms are Pt, while the small, light atoms are Bi.

together to ensure uniform mixing. After melting, the reaction temperature is reduced in order to solidify the mixture and if an ordered intermetallic phase is desired, a low-temperature annealing is required to nucleate the thermodynamically stable product at the appropriate temperature. While this method has been extremely successful in forming many intermetallic structures, it has several shortcomings. First, a large amount of energy is required to induce solid-solid diffusion of bulk powder reagents which are usually on the order of at least several microns. Second, the high temperatures required can make it very difficult to access metastable or low-temperature phases, as thermodynamically structures usually tend to nucleate first upon cooling from a melt, and reaction times can span from days to weeks or longer. Finally, there is little to no control of crystal size or particle morphology, and nanomaterials are generally inaccessible. Methods which can access nanomaterials such as ball milling, metal-flux, and CVD improve upon control over many of the aforementioned variables, however these methods still require long reaction times, expensive instrumentation, or specialized chemical precursors.

Alternative synthetic routes to alloy and intermetallic nanomaterials are necessary to efficiently produce them on a large scale for use in new, smaller devices. Drastically reducing the particle sizes of elemental precursors to nanometer length scales can lower the energy barrier to solid-solid diffusion, which can translate into faster and lower temperature reactions. This approach is not a new concept to solid-state chemists, as co-precipitation of insoluble precursors such as metal carboxylates and hydroxides has been employed to yield more thoroughly mixed synthetic reagents than could normally be prepared by mechanical grinding.[32] Because the resulting powders are so fine and homogenously mixed, solid-solid diffusion is no longer a rate-limiting step, allowing for lower temperature reactions and greater kinetic control over final products.

However, until very recently this approach has not been applied to nanoscale elemental metal reagents to form alloys and intermetallics.[33]

Solution synthesis, or colloidal synthesis, is a highly versatile bottom-up approach to accessing nanocrystalline metallic materials. These reactions generally involve the reduction or thermal decomposition of metal salt, metal oxide or organometallic precursors, and alloys and intermetallics can usually be synthesized from 100 to 300 °C. As with traditional approaches, product composition can generally be controlled simply via reagent concentration. More importantly, the controllable reaction kinetics of solution routes can allow for control over particle size, morphology, and crystalline phase.[34,35] Indeed, many solution chemistry strategies exist which extend control over particle sizes for single-metal and metal-oxide materials,[6,36-38] and shape control for single-metal,[34,35,39,40] metal-oxide,[37] and multi-metal products[41,42] is also well established. In addition, there are a few reports of accessing new and metastable crystal structures in nanocrystals via solution routes which were not previously known in bulk materials.[43-45] Control over these factors is critical to expanding the utility of multimetallic nanomaterials. Finally, the nanometer-scale particles synthesized via solution routes are dispersable in solution and highly amenable to solution based processing and are usually compatible with known colloidal processing methods such as spin coating and templating.[3,46-48]

The following chapters detail the development of several solution-based routes to nanocrystalline binary alloy and intermetallic materials with a wide range of interesting and useful physical and chemical properties. The first method, referred to as the nanocomposite route, involves the precipitation of phase-separated, bimetallic nanocrystalline particles from aqueous metal-salt solutions which may be converted to alloys or intermetallics upon subsequent solid-state heating (Figure 1.3). This method was pioneered by Sra and Schaak for the synthesis of intermetallic AuCu and $AuCu_3$ from Au (III) and Cu (II) salts.[49] It is important to note that this was not the first report of converting nanoparticulate alloys or composites into atomically ordered intermetallics. Sun and Murray reported the solution-based synthesis of fcc FePt alloy nanocrystals which could be spun-cast into a film and annealed at high temperatures (550 °C), nucleating the ferromagnetic fct FePt intermetallic.[2,3] Similarly, Teng and Yang were able to exploit the high reactivity of nanocrystals to convert a thin-film of core-shell Pt-Fe_2O_3 nanoparticles to FePt by high-temperature heating in a reducing atmosphere.[50] While these methods were successful in accessing intermetallic compounds from nanocrystal precursors, the final products had experienced a high degree of sintering during annealing and were no longer discrete nanocrystals. The Au-Cu intermetallics synthesized by Sra, using the low-temperature nanocomposite method, were the first solution re-dispersable atomically ordered nanocrystals to be reported. In Chapter II, we describe how the nanocomposite route is used to access nanocrystalline Au-Pd alloys of variable composition to establish the utility of the method in controlling the final alloy composition. Au-Pd alloys are also useful heterogeneous catalysts,[51-54] and through collaboration we have tested these materials for their catalytic activity in the direct synthesis of H_2O_2 from hydrogen and oxygen gases, as well as the synthesis of

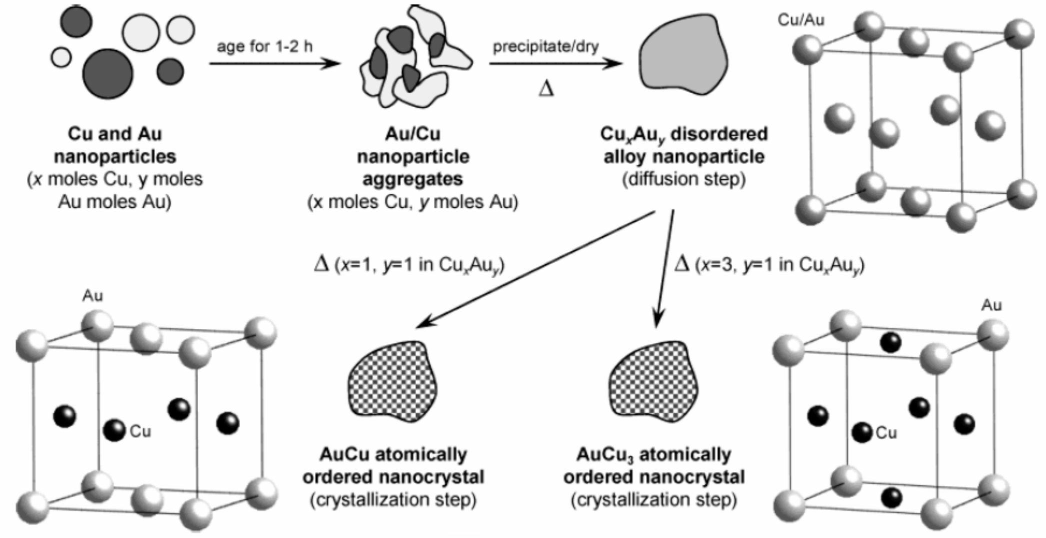

Figure 1.3 This cartoon schematic outlines the multi-step approach of the nanocomposite method to forming AuCu and AuCu3 intermetallics from phase-segregated nanocomposites. (Source: Schaak, *et al.*, 2005)

vinyl acetate (an important monomer used in the manufacture of several commercial polymers[55]) from acetic acid and ethylene and report their catalytic activities.

The second method used herein to access intermetallic nanocrystals is a modification of the polyol process. The polyol process uses high boiling point polyalcohol solvents, which can also act as mild reducing agents when heated, to precipitate nanocrystalline metal powders from metal salt and metal oxide precursors. When the process was initially introduced , single-metal and bimetallic alloy particles of the late transition metals were accessible ranging from several-hundred nanometer to micron scale dimensions.[56,57] More recently, the process has been modified by many groups to produce size- and shape-controlled nanocrystals of a variety of elements and alloys, yielding nanomaterials with important magnetic, catalytic and optical properties.[34,36,39-41,58,59] Upon modification by the Schaak group, the polyol process has proven to be very useful for the direct synthesis of nanocrystalline intermetallics,[35,45,48] as this approach bypasses the high-temperature melting required for bulk metallurgical techniques and shortens reaction times to several minutes. Additionally, Leonard *et. al.* have shown the process can produce nanocrystals of new ternary intermetallic compounds with structures not originally discovered using traditional bulk syntheses.[43] In Chapter III, we show that the polyol process is quite general for the synthesis of intermetallic nanocrystals, specifically in the systems *M*-Sn (*M* = Ag, Au, Co, Cu, Fe, Ni), Pt-*M'* (*M'* = Bi, Pb, Sb, Sn), and Co-Sb, many of which have important properties with applications in magnetic,[22] catalytic,[4] high-capacity battery electrode,[60] and thermoelectric materials.[14,26,31]

The third method, referred to as the organometallic route, is based upon the conversion of single-metal nanocrystals to *M*-Zn intermetallics via reaction with zero-valent organozinc compounds in long hydrocarbon-chain amine solvents which can also function as surface stabilizers.[2,3] Zinc alloys are desirable materials for their mechanical hardness and corrosion resistance,[61] and *M*-Zn intermetallic compounds are also important materials because of their advanced chemical and physical properties, such as catalytic production of H_2 [62] and methanol,[63] magnetism,[64] shape-memory effects,[65-67] and tunable surface plasmon resonance (SPR) in colloids.[1] Several strategies have been developed for preparing nanoscale zinc/transition metal alloys and intermetallic compounds, such as ball-milling,[68] annealing a ZnO-supported transition metal in a reducing atmosphere,[69] electroplating,[70] and laser ablation of bulk *M*-Zn intermetallics.[15] These approaches have yielded nanocrystalline materials, but phase-pure products are difficult to achieve, reaction times can be long, and particle size and morphology are essentially uncontrollable. Several different solution chemistry routes have also been used to access nanocrystalline *M*-Zn compounds, however, they have involved the use of harsh and powerful reducing agents to reduce zinc (II),[71] the thermal decomposition of a complex single-source precursor followed by high-temperature reduction under H_2,[72] and electrochemical deposition into porous anodic alumina templates.[64]

While these solution methods have yielded nanoscale *M*-Zn solids, it remains challenging to rigorously control their morphology (in comparison to capabilities for many single-metal systems), and the synthetic development has largely been limited to the Cu-Zn system. Through the thermolysis of a specially prepared Cu(II) reagent with Et_2Zn, alloy and intermetallic nanocrystals of various Cu-Zn compositions were prepared with some degree of morphological control.[1] Unfortunately, it can be challenging to apply similar chemistry to other *M*-Zn systems without the need for significant new synthetic development. This issue is part of a broader problem in nanocrystal synthesis is the ability to routinely incorporate electropositive metals or metals whose precursors are not easy to reduce into nanocrystals with the ability to simultaneously control their morphology. Some examples of nanocrystalline alloys and intermetallic compounds containing Al and Mg are accessible using solution chemistry techniques.[73-75,76] However, very few other examples have been reported, and none have shown evidence of extensive generality or significant morphological control. Generalized strategies for incorporating hard-to-reduce metals into intermetallic nanocrystals using robust solution chemistry techniques could impact several areas of modern materials research that rely on these elements for their properties, including catalysis, structural materials, superconductivity, hydrogen storage, and magnetic materials.

We shown in Chapter IV that the organometallic route is a generalized strategy to access *M''*-Zn intermetallic compounds (*M''* = Au, Cu, Pd) via the chemical conversion of metal nanoparticles upon reaction with zero-valent organometallic zinc precursors.[77] Using commercially available reagents, transition-metal nanocrystals are made in hot coordinating organoamine solvents, which can be further reacted with diethylzinc or diphenylzinc to form intermetallic AuZn, Au_3Zn, Cu_5Zn_8, and PdZn. The reaction pathway from the single-metal to the intermetallic is confirmed, and overall particle morphology is often conserved throughout the conversion. This method offers a general and robust strategy to zinc-based intermetallics with known catalytic,[62,63] shape-memory,[65-67] and corrosion resistant properties.[61]

The concept of solid-state conversion chemistry in solution is very interesting and potentially very powerful. In addition to the *M*-Zn nanocrystals we have synthesized, it has been shown that shape-controlled *M*-Sn intermetallics may be synthesized through the reaction of β-Sn nanocrystals with metal salt solutions under reducing conditions,[42] and metal phosphides can be formed by reacting single-metal nanoparticles with trioctylphosphine.[78,79] We have expanded upon our established conversion chemistry by conducting analogous studies with alloys and intermetallic precursors, which can be structurally and compositionally more complex. Using the polyol method, we show in Chapter V that nanocrystalline intermetallics can undergo conversion to derivative phases within 1 hour by reacting them with metal salt reagents at temperatures below 300 °C.[80] Surprisingly, these conversions are cyclic, which has never been demonstrated before for nanocrystalline metal compounds and would not be expected for bulk intermetallics, although we show evidence that this reaction with nanocrystalline precursors may be robust and more general than anticipated. This cyclic interconversion of nanocrystalline intermetallics nicely highlights the high reactivity of metallic nanocrystals in solution, as well as the power of our conversion chemistry approach to nanocrystal synthesis. This method may open the door to intermetallic compounds which are difficult to access as nanocrystals, as well as new and metastable low-temperature compounds.

Finally, all of the solution routes we have employed to access alloys and intermetallics produce colloidal dispersions, and accordingly we explore some new approaches to colloidal crystal self-assembly in Chapter VI. Our approach is based on template directed assembly, in which spherical colloids with sizes ranging from visible to IR wavelengths spontaneously crystallize in lithographically patterned features.[81] This approach allows us to quickly and easily fabricate hexagonally close-packed structures from polystyrene and silica spheres, and more complex structures are also accessible through the use of epitaxial templates. We show that some of these structures can be removed from the template intact, and may be useful as 2-dimensional building blocks. Our template-assisted method may be relevant for the design and fabrication of colloidal crystals for photonic band-gap materials, for which both particle size and crystal structure can significantly influence optical properties. Further advances in shape and size controlled synthesis of alloy and intermetallic nanocrystals may lead to the unification of our micron-scale self-assembly strategies with the nanometer-scale synthetic work described in earlier chapters.

CHAPTER II

Au-Pd ALLOY SYNTHESIS: NANOCOMPOSITE ROUTE, MODIFIED POLYOL ROUTE, AND CATALYST DESIGN*

2.1 Introduction

Au-Pd alloys have been widely studied for their catalytic applications. They have demonstrated catalytic activity for reactions such as the oxidation of small alcohols,[51] hydrogenation of alkenes and aromatics,[52] and the hydrodesulfurzation of petroleum feedstock.[53] Perhaps one of the most important catalytic applications for a Au-Pd alloy is the acetoxylation of ethylene to vinyl acetate,[54] a highly important monomer used to manufacture a wide variety polymers.[55] Au-Pd has also been shown to have good activity for the oxidation of CO,[82,83] which is highly relevant for fuel cell operation. It is true that Pd alone can catalyze many of these reactions, however Pd-Au alloys have generally demonstrated higher activites, selectivities and stabilities.[51,53,83,84] For example, recent reports from the Goodman group have shed light upon the nature of the active site on the alloy surface for vinyl acetate synthesis.[85] Detailed analyses of catalytically active surface sites are usually performed on thin films created under high vacuum via vapor deposition, however industrial heterogeneous catalysts and those in

---

* Reprinted in part with permission from *J. Am. Chem. Soc., 127* Schaak, R. E.; Sra, A. K.; Leonard, B. M.; Cable, R. E.; Bauer, J. C.; Han, Y.-F.; Means, J.; Teizer, W.; Vasquez, Y.; Funck, E. S. "Metallurgy in a Beaker: Nanoparticle Toolkit for the Rapid Low-Temperature Solution Synthesis of Functional Multimetallic Solid-State Materials," 3506, Copyright 2005 by the American Chemical Society.

devices are generally supported or unsupported nanocrystalline powders.

Nanocrystalline powders are of interest as industrial catalysts for several reasons. If particle sizes are small enough, they can have extremely high surface-area-to-volume ratios, which theoretically translates to more catalytically active surface sites per unit of material. In addition, the large ratio of unsaturated surface atoms can increase the reactivity of nanocrystals compared to bulk, and therefore may enhance catalytic activity. Consequently, nanocrystalline powders are economically advantageous from a materials cost perspective, but they may also be made through quick and low-temperature techniques which can lower synthetic costs. Hoping to develop more industrially applicable materials, we synthesized both supported and unsupported nanocrystalline Au-Pd alloy powders using techniques partly developed in the Schaak group.[47,49]

The methods discussed herein to create the nanocrystalline Au-Pd powders are solution-based routes involving the reduction of dissolved metal salts. The first process involves the aqueous synthesis of a bimetallic nanocomposite in the presence of a surface stabilizing agent, and after isolation, the powders may be extracted from solution and alloyed through a quick, low-temperature annealing step.[47,49] The second is a modification of the polyol process, in which metal salts are reduced and then refluxed in a high boiling-point polyalcohol solvent to facilitate solid-solid diffusion.[2,3,35] Using these basic synthetic techniques, we have found that Au-Pd alloys can be accessed in-situ, even at room temperature, by controlling the reaction conditions. The synthesized nanocrystalline alloy powders have been characterized by X-ray diffraction (XRD) for their bulk crystal structure, transmission electron microscopy (TEM) for their particle size and morphology and energy dispersive X-ray spectroscopy (EDS) for their elemental composition. Through collaboration with the Goodman and Lunsford groups, their catalytic activities were investigated for the reactions of vinyl acetate and hydrogen peroxide synthesis,[47] respectively.

2.2 Experimental details

2.2.1 *Nanocomposite route synthesis*

The Au-Pd nanocomposites were synthesized in an aqueous solution similarly to our previous reports.[47,49] All chemicals were used as received from Alfa Aesar unless otherwise noted, and all aqueous solutions were prepared using distilled, deionized water (18.2 MΩ). A typical 1:1 molar ratio Au-Pd nanocomposite can be made from a 30 mL aqueous starting solution of $PdCl_2$ (6.0 mg, 0.035 mmol; 99.9%) and $HAuCl_4{\bullet}3H_2O$ (13.7 mg, 0.035 mmol; 99.99%) in the presence of a stabilizing agent such as poly(vinylpyrrolidone) (PVP; MW = 40,000, 0.140 g). After stirring under bubbling Ar for 30 min, the solution is co-reduced by the addition of 25 mL of a freshly prepared 0.01 M solution of $NaBH_4$ (98%). This final mixture is allowed to stir from 2 hours to overnight, after which the nanocomposite powders are isolated from solution by high-speed centrifugation at 13,000 rpm, washed several times with CH_3CH_2OH (EtOH) and allowed to dry in ambient conditions. The dried powders were annealed in a well-purged quartz-tube furnace under flowing Ar from 100-600 °C at 100 degree intervals for 90 minutes each. The following different stabilizing agents were also used with this technique: polyethylene oxide (PEO; MW = 100,000), poly(styrenesulfonic acid) sodium salt (PSS; MW = 70,000), polyethylene glycol (PEG; MW = 20,000), poly(2-ethyl-2-oxazoline) (P2E2O; MW = 50,000), and sodium acetate trihydrate ($CH_3COONa{\bullet}3H_2O$, EM Science).

2.2.2 *Supported nanocrystalline $AuPd_4$ preparation*

$AuPd_4$ was made on two different types of supports, i.e., silica spheres with an average diameter of roughly 500 nm, and high surface area porous SiO_2 (Aldrich, 230-400 mesh) with a surface area of 600 m^2/g and a pore volume of 1.1 mL/g. To prepare $AuPd_4$ on SiO_2 spheres, a 40 mL aqueous solution of $PdCl_2$ (0.076 mmol), $HAuCl_4{\bullet}3H_2O$ (0.021 mmol), and PVP (140 mg) was stirred at room temperature under bubbling Ar for 30 min. A fresh 5 mL solution of $NaBH_4$ (90.0 mM) was added to co-reduce the metals, turning the solution dark black/purple, and stirring under bubbling Ar was continued. After 30 min, a dry powder of SiO_2 spheres (roughly 100 mg) was added, and the solution was stirred under bubbling Ar for 1 hour longer, then it was capped and stirring continued overnight. $AuPd_4$ on porous SiO_2 support (5 % by weight) was prepared slightly differently on a larger scale. A 30 mL aqueous solution of $PdCl_2$ (0.16 mmol) and $HAuCl_4{\bullet}3H_2O$ (0.039 mmol) with 10.0 g $CH_3COONa{\bullet}3H_2O$, which acted as the surface stabilizer, was stirred under bubbling Ar for 30 min. The solution was co-reduced by the quick addition of 1 mL of a freshly prepared aqueous $NaBH_4$ solution (0.22 M), followed by the quick sequential addition of 0.475 g SiO_2 catalyst support and another 1 mL portion of $NaBH_4$ solution. After stirring under bubbling Ar for 1 hour, the final mixture was stirred vigorously overnight. All supported $AuPd_4$ products were isolated by centrifugation, washed three times with EtOH, and dried at 50 °C. 440 mg of $AuPd_4$ on porous SiO_2 catalyst supported was recovered after centrifugation and the calculated yield found was 88 %.

2.2.3 *Modified polyol synthesis*

$AuPd_4$ nanocrystalline alloy powders were made by a modified polyol process similar to previous reports.[35,48] Reactions were carried out in either pure polyalcohol solvents or a mixture of polyol and water. Typically, $AuPd_4$ alloy was synthesized in pure polyol by dissolving $PdCl_2$ (0.077 mmol) in 40 mL triethylene glycol (TrEG; 99%, bp 284-288 °C) with the aid of 2 drops of concentrated HCl. After the $PdCl_2$ was completely dissolved, PVP (140 mg) and $HAuCl_4{\bullet}3H_2O$ (0.02 mmol) were added and stirred to dissolve. The solution was then stirred under Ar for 30 min, and the metal cations were then co-reduced by the addition of a fresh solution of $NaBH_4$ in TrEG (5 mL, 9.1 mmol). The solution was then heated to a boil for 1.5 hours under bubbling Ar.

$AuPd_4$ alloy was also synthesized in a mixture of polyol and water (40 mL polyol, 5 mL H_2O) by first dissolving $PdCl_2$ (0.073 mmol) with the aid of 1 drop of conc. HCl. Both TrEG and diethylene glycol (DEG; 99%, bp 245 °C) were used as the polyalcohol co-solvent. After the $PdCl_2$ is dissolved, PVP (140 mg) and $HAuCl_4{\bullet}3H_2O$ (0.02 mmol) were added and stirred to dissolve. The solution was stirred under Ar for 30 min, and the metal cations were then co-reduced by the addition of a fresh solution of $NaBH_4$ in H_2O (5 mL, 8.7 mmol). The solution was then heated to a boil for 1.5 to 2 hours under bubbling Ar. All powders were isolated by centrifugation, washed several times in EtOH and allowed to dry in ambient conditions.

2.2.4 *Characterization and catalytic property measurements*

Powder X-ray diffraction (XRD) data were collected on a Bruker GADDS three-circle X-ray diffractometer using Cu Kα radiation. Transmission electron microscopy (TEM) images, selected area electron diffraction (SAED) patterns, and energy-dispersive X-ray analysis (EDS) were collected using a JEOL JEM-2010 TEM. Samples were prepared by sonicating the nanocrystalline intermetallic powders in ethanol and dropping a small volume onto a carbon-coated nickel grid. Differential scanning calorimetry (DSC) data were collected on a TA Instruments Q600 SDT under Ar.

Catalytic reactions for vinyl acetate (VA) synthesis and CO oxidation were carried out in a fixed bed reactor comprised of a quartz tube with an inner diameter of 0.8 cm and a 1-2 cm length catalyst bed packed with Au-Pd catalyst at atmospheric pressure. The incoming reactant gases were regulated by mass flow controllers, and the reactor temperature was regulated by a MICROMEGA temperature controller (CN77000 series). The products were analyzed by an online gas cromatograph (HP 5890 GC) connected to a computing integrator (HP 3393 A), using He as the inert carrier gas. A HayeSep-R column (100/120 mesh) and a flame ionization detector (FID) were used to detect VA and AcOH, while a Porapak-R column (80/100 mesh), with a thermal conductance detector (TCD), was used to measure CO and CO_2. The catalysts were pretreated by a thermal oxidation step in O_2 (10 % in N_2, 20 mL/min) at 400 °C for 30 min, followed by a thermal reduction in H_2 (5% in Ar, 20 mL/min) at 300 °C for 30 min. VA synthesis reactions were carried out at 150 °C by feeding the following reagent gases into the reactor at a total flow rate of 60 mL/min in N_2: ethylene (C_2H_4, 7.5 kPa), O_2 (1.0 kPa), and acetic acid (AcOH, 2.0 kPa). CO oxidation reactions were carried out at variable temperatures from 25-200 °C by feeding CO_2 (2.0 kPa) and O_2 (1.0 kPa) into the reactor in N_2.

Catalytic reactions for H_2O_2 synthesis were carried out at atmospheric pressure and at 10 °C in the reactor described in ref. 86. The experiment was carried out using a 4:1 O_2/H_2 gas mixture at a total flow rate of 50 mL/min in a 0.24 N H_2SO_4/ethanol solution. *Since the 4:1 O_2/H_2 gas mixture is in the explosive regime, care was taken to avoid contact of the gas mixture with a dry catalyst*. This was achieved by first mixing 5 mg of the catalyst with 10 mL of the solution and returning this slurry to the solution that remained in the reactor. Even with this precaution, *explosions did occur* with ethanol as the liquid phase. The use of methanol was even more hazardous because of its higher vapor pressure. The reagent gases were introduced into the reactors via a fine glass frit, and the slurry containing the catalyst was stirred to minimize diffusion limitations. The reactor was connected to a gas chromatograph so that the concentration of H_2 exiting the reactor could be periodically determined. Improved accuracy in the H_2 analysis was achieved by using a H_2/N_2 mixture that contained 10% N_2. The H_2O_2 formed during the reaction was analyzed colorimetrically after complexation with a $TiOSO_4/H_2SO_4$ reagent. The selectivity for H_2O_2, $S_{H_2O_2}$, was determined from the rate of H_2O_2 formation and the rate of H_2 conversion using equation 2.1.

$$S_{\mathrm{H_2O_2}} = \frac{\text{rate of } \mathrm{H_2O_2} \text{ formation (mol/min)}}{\text{rate of } \mathrm{H_2} \text{ conversion (mol/min)}} \times 100 \qquad (2.1)$$

2.3 Nanocomposite route synthesis and characterization

A variety of Au-Pd nanocrystalline bimetallic alloys have been synthesized by the nanocomposite route through stoichiometric control of the metal salt reagents. As explained in the experimental section, the co-reduction of Pd^{2+} and Au^{3+} salts in the presence of a surface stabilizing agent, such as PVP, yields a Au-Pd nanocomposite. These nanocomposites were thermally annealed at low temperatures under Ar to induce solid-solid diffusion, and the results were observed by powder XRD. The room-temperature product for a reaction with a 1:1 molar ratio of Au and Pd reagents appears to be a simple fcc pattern (Figure 2.1), however the peaks are very broad and upon inspection they appear to have shoulders, implying the presence of Au-Pd alloy, as well as phase-separated Au and Pd. Upon annealing at 100 °C for 90 min, the peaks clearly split and an Au-Pd alloy and Au appear to be present. The alloy peaks shift to higher angles as the product is annealed at higher temperatures, reflecting the diffusion of Au and Pd into each other. The sample remains phase-separated until it is annealed at 400 °C, and the XRD pattern for that temperature shows an single-phase fcc pattern with a lattice constant between those of Au (4.072 Å) and Pd (3.89 Å). Using Vegard's law,[32] an estimate of the final composition of the alloy is roughly 55 at. % Pd.

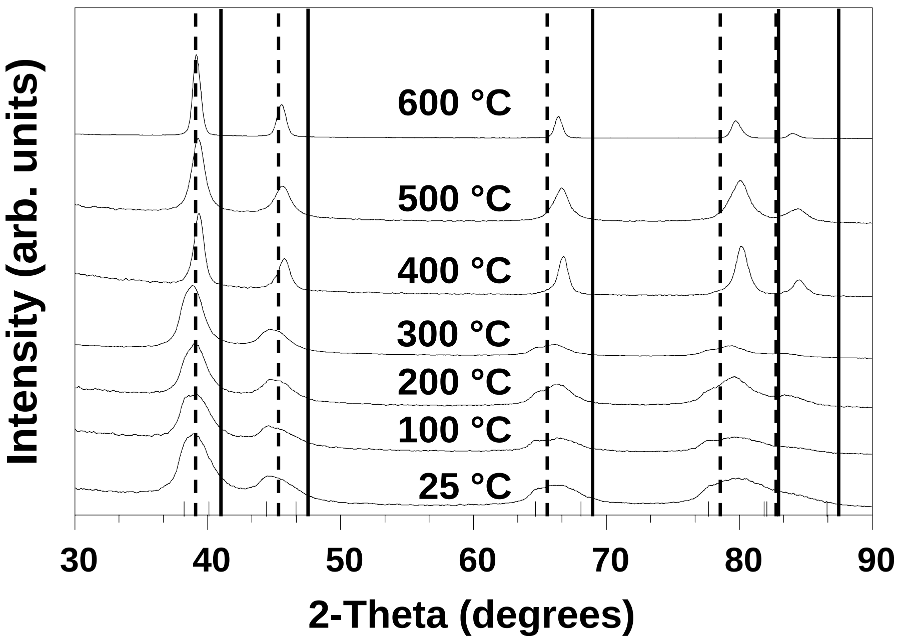

Figure 2.1 Powder XRD patterns of Au-Pd nanocomposite products for a 1:1 molar starting composition, analyzed post-reduction as well as post-annealing in Ar from 100 to 600 °C. Dashed lines indicate positions of Au reflections and solid indicate those for Pd.

A series of experiments were conducted with initial stoichiometries Au_4Pd, Au_3Pd, Au_2Pd, $AuPd_2$, and $AuPd_4$ in order to determine the relationship between the nominal and final stoichiometries. Figure 2.2 shows the relationship between the nominal composition in at. % Pd and the lattice constants of the products after annealing to at least 400 °C for 90 min as determined by XRD. There is a fairly linear relationship between the nominal and actual alloy composition, and the lattice constant it predicts for pure fcc Au is 4.102 Å, a difference of 0.03 Å from the bulk.[87] The difference may be due in large part to experimental error in weighing the milligram-scale amounts of reagents required for the reactions. Two of the as-made nanocomposites were

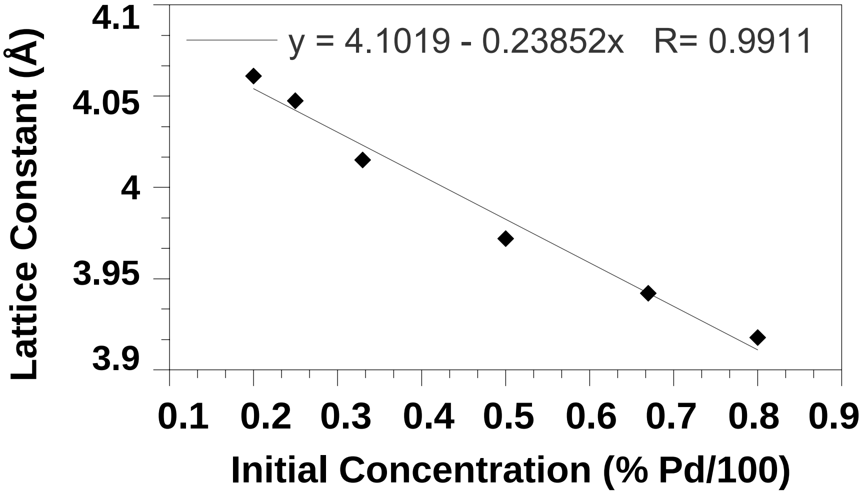

Figure 2.2 Plot of the relationship between the initial molar concentration and lattice constant of Pd in Au-Pd products formed by the nanocomposite route. Lattice constants calculated by Bragg's Law.

analyzed by transmission electron microscopy (TEM). As-made Au_3Pd (Fig. 2.3a) shows particle sizes ranging from roughly 10 to 30 nm, although the XRD shows extremely sharp peaks which can be indexed to Au (Fig. 2.4). It may be that the larger particles are Au-rich, while the smaller particles may be Pd-rich and may be amorphous or their XRD diffraction intensity is drowned out by the Au. Energy-dispersive X-ray analysis (EDS) confirms that Pd is present in a 18 at.% Pd, and the low Pd content may be due to the incomplete precipitation of Pd, which may explain the light brown color of the supernatant often seen after centrifuging the reaction solution. Figure 2.3b shows as-made $AuPd_4$ particles which range from roughly 3 to 6 nm which is consistent with the broad XRD peaks (Fig. 2.4), and EDS analysis gives an atomic ratio of 80:20 Pd:Au. It is clear from the XRD of Au_3Pd and $AuPd_4$ that the as-made samples are not phase-pure,

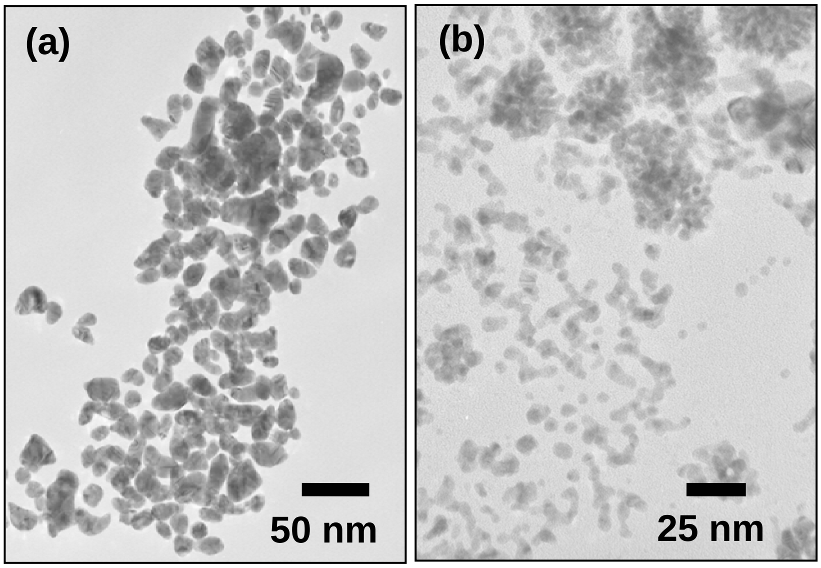

Figure 2.3 TEM images of (a) Au_3Pd and (b) $AuPd_4$ as-made by the nanocomposite route.

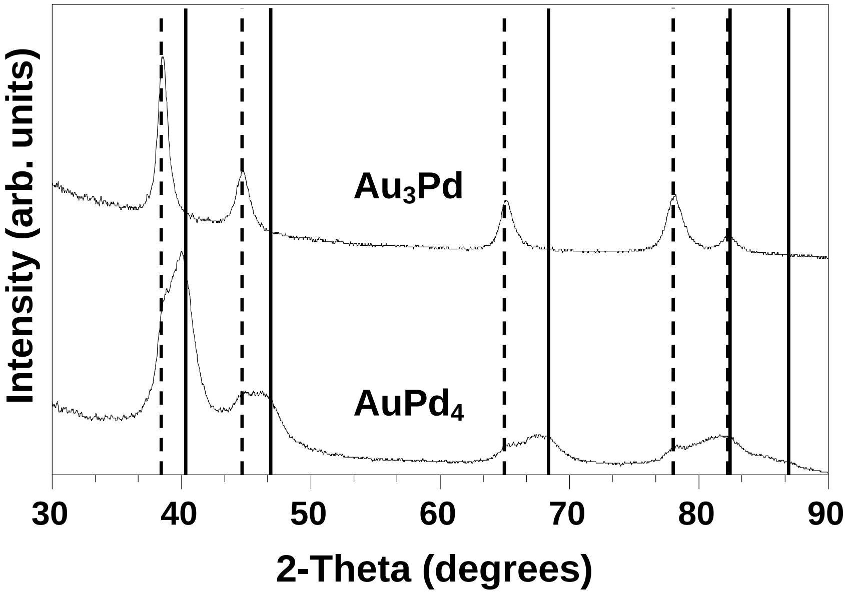

Figure 2.4 Powder XRD data of Au_3Pd and $AuPd_4$ as-made by the nanocomposite route. Dashed lines indicate positions of Au reflections and solid indicate those for Pd.

but appear to be a mixture of Au or Pd and a Au-Pd alloy. In summary, the co-reduction nanocomposite route with PVP stabilizer seems to provide good control over the final composition of the products when combined with an annealing step.

The nanocomposite route was also tested with a variety of other polymeric surface stabilizing agents. $AuPd_4$ was synthesized according to the experimental above with 0.076 mmol Pd, replacing PVP with the same mass of PSS, PEO, PEG and P2E2O with interesting results. The powder XRD pattern for the room-temperature as-made products (Fig. 2.5) for the PEO, PEG, and P2E2O trials all appear to be single phase, as the fcc peaks are at an intermediate position between Au and Pd, while the PSS and PVP

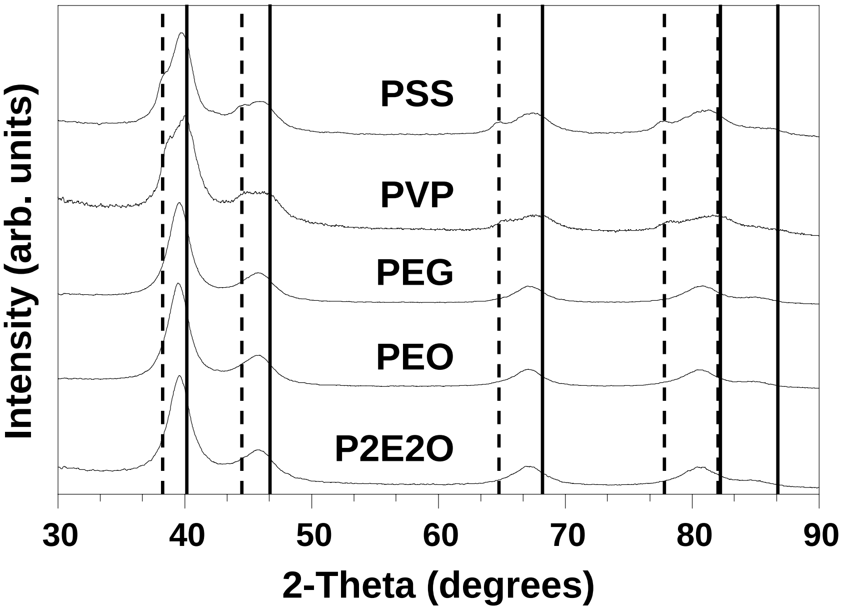

Figure 2.5 Powder XRD data of $AuPd_4$ as-made by the nanocomposite route with different surface stabilizing agents. Dashed lines indicate positions of Au reflections and solid indicate those for Pd.

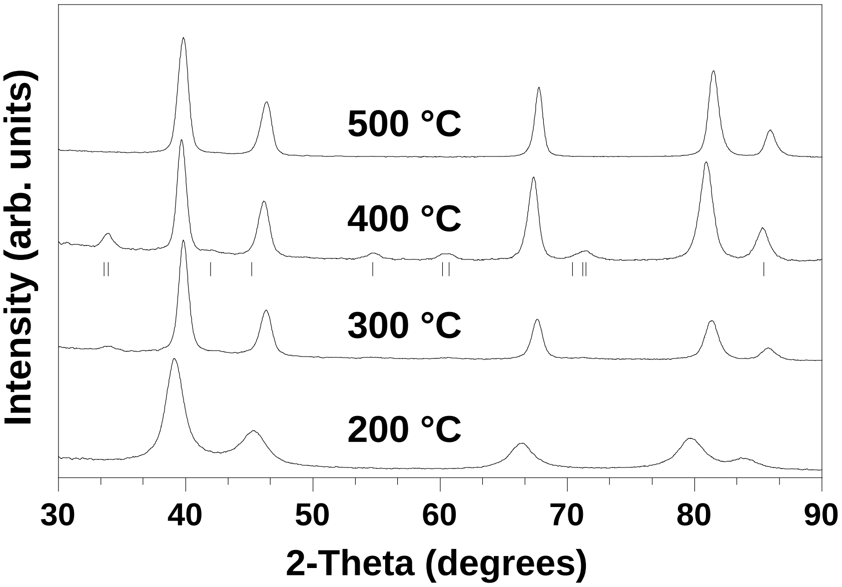

Figure 2.6 Powder XRD data of $AuPd_4$, stabilized by P2E2O, made by the nanocomposite route and annealed at different temperatures in Ar. Tick marks indicate allowed PdO reflections.

trials are clearly phase-separated, showing Au, Pd and a Au-Pd alloy. It is not possible, however, to assume that the PEO, PEG, and P2E2O stabilized products are a pure single phase product at room-temperature because the peaks are extremely broad and shoulders may not be resolvable with the powder diffractometer used. Upon annealing, the alloy peaks shift to higher angles in all samples as diffusion occurs, and the calculated lattice constant shifts closer to the nominal. At 300 °C, a new phase appears in the PEO, PEG, and P2E2O XRD patterns with major reflections at 33.9, 54.7, 60.5, and 71.4 degrees 2θ. Figure 2.6 shows the P2E2O system annealed from 200 to 500 °C with tick marks corresponding to the allowed reflections of tetragonal PdO, showing that this impurity appears by 300 °C remains until the sample is annealed at 500 °C. The PdO impurity was not seen in the PSS and PVP stabilized trials, so it may be possible that the previous polymer stabilizers are decomposing and reacting with the alloy powders upon annealing. By taking an average of the calculated lattice constants for the nanocrystalline powders made with each of the polymer stabilizers and annealed at 400, 500, and 600 °C (Table 2.1), it is clear that the PEG stabilized product most closely matches the nominal alloy composition at 81 at. % Pd. It seems that PEG and P2E2O may be the most labile stabilizing polymers,[89] allowing for more complete solid-solid diffusion in the nanocrystalline powders upon reduction. This is consistent with the fact that the as-made PSS and PVP stabilized products show two phases by powder XRD, while the PEG and P2E2O stabilized products appear to be single phase alloys.

Table 2.1 Averages of the lattice constants for $AuPd_4$ alloys synthesized with different stabilizing polymers, and final atomic percent Pd as calculated by Vegard's Law.

Polymer	Lattice Constant (Å)	Final %Pd
PSS	3.944	71
PEO	3.935	76
PEG	3.925	81
P2E2O	3.920	85
PVP	3.918	86

2.4 Modified polyol synthesis of $AuPd_4$

Two approaches were taken to synthesize nanocrystalline $AuPd_4$ powders via the modified polyol synthesis. The first involved the room-temperature co-reduction of Au^{3+} and Pd^{2+} in the presence of PVP in a polyol solvent and a small amount of water, followed by the addition of either diethylene glycol (DEG) or triethylene glycol (TrEG) and subsequent heating to reflux for 1 hr. The role of the water was to facilitate the dissolution of $PdCl_2$, which has a much lower solubility in the polyol solvents than water. The second approach was to use pure TrEG as the solvent with or without a stabilizing agent. The XRD for the powders refluxed in DEG and TrEG are shown in Figure 2.7. The $AuPd_4$ powders refluxed in DEG appear to have much smaller particle sizes by XRD analysis due to the much broader peaks than seen for the powders refluxed in TrEG. The difference may be due in part to the fact that DEG refluxes at about 250 °C while TrEG refluxes at about 290 °C, which may justify the assumption that the TrEG refluxed powders underwent more particle sintering than those refluxed in DEG. However, there is also a clear difference in the peak positions, as the DEG refluxed powders appear to be more Au rich than the TrEG refluxed powders. On the basis of Vegard's law, the DEG refluxed powders have a composition of about 54 at. % Pd, while the TrEG refluxed powders have a composition of 74 at. % Pd, much closer to the nominal composition. It is difficult to tell from the XRD if the DEG refluxed $AuPd_4$ is single phase due to the peak broadening, however because of the estimated composition it is likely that there is incomplete solid-solid diffusion and that there are local areas that are Au or Pd rich in the powder. In order to gain more information about the DEG and TrEG refluxed powders, they were analyzed by TEM. Figure 2.8a shows the $AuPd_4$ powders refluxed in DEG. The particles are spherical to elliptical in shape, and range from 3 to 5 nm, although some extremely small particles can be seen which are as small as 1 nm. Although no determination can be made from the TEM image regarding the

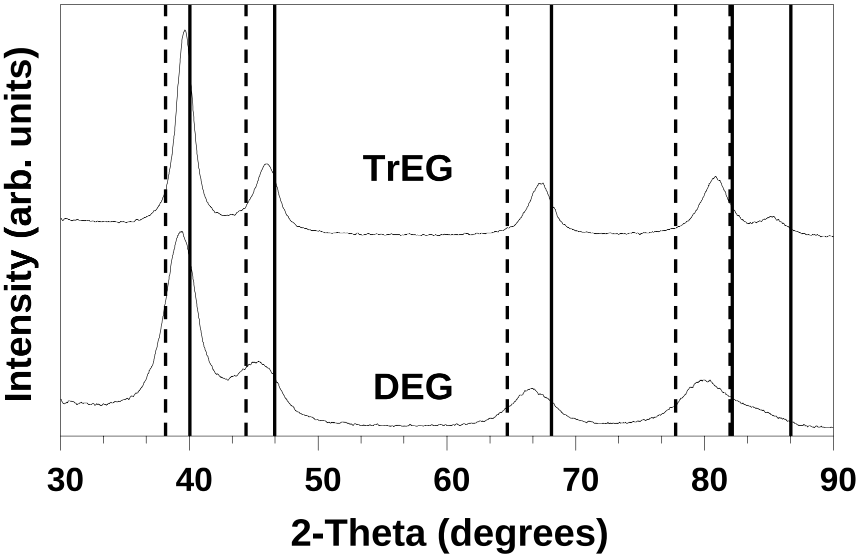

Figure 2.7 Powder XRD data of $AuPd_4$ made by the polyol process in diethyleneglycol (DEG) and triethyleneglycol (TrEG). Dashed lines indicate positions of Au reflections and solid indicate those for Pd.

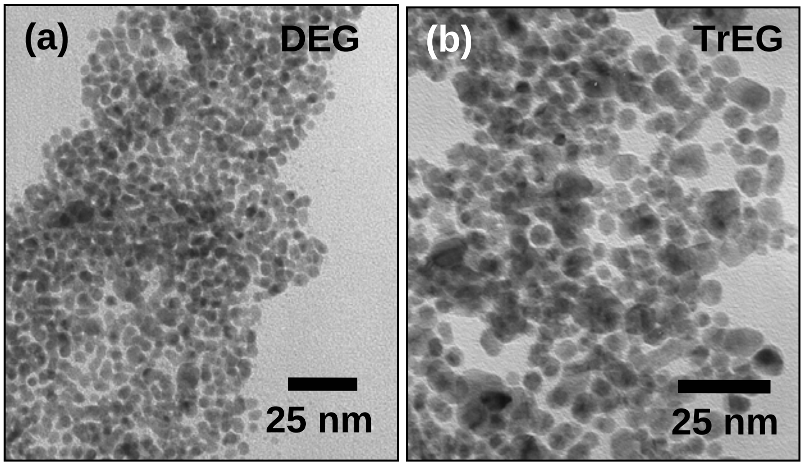

Figure 2.8 TEM images of $AuPd_4$ made by the polyol process in (a) diethyleneglycol (DEG), and (b) triethyleneglycol (TrEG).

composition of each particle, the small particle sizes are consistent with the broad XRD peaks. Figure 2.8b shows the $AuPd_4$ powders refluxed in TrEG, and it is clear that there is a broad particle size distribution. The particles are still generally spherical, however there are many larger faceted particles and many particles which seem to be sintered together, and sizes range from 3 to 15 nm which is consistent with the sharper XRD peaks. It is possible that the combination of DEG and PVP stabilize the particle surfaces more effectively than TrEG and PVP, resulting in smaller particles. It may also be possible that the higher temperature reflux of TrEG is responsible for particle growth and sintering. The very small particles seen in the DEG sample are not seen in the TrEG sample, which could support either hypothesis explaining the large difference in particle size and size dispersity between the two experiments.

The second approach to making nanocrystalline $AuPd_4$ powders was the use of only TrEG as a solvent. In addition, the room-temperature reduction with $NaBH_4$ followed by refluxing method was compared with the direct polyol process wherein the hot solvent acts as the reducing agent. Initially, a TrEG solution of $NaBH_4$ was used to co-reduce Au^{3+} and Pd^{2+} in a 1:4 molar ratio in the presence of PVP at room temperature, followed by refluxing for 1.5 hr. The precipitated powders clearly appear to be a mixture of Pd and an Au-Pd alloy (Fig. 2.9 bottom). Judging from the positions of the higher angle alloy peaks, the alloy is likely more Au-rich than the nominal $AuPd_4$ stoichiometry. In order to determine the role of PVP in the solution route synthesis of $AuPd_4$ in TrEG, the previous experiment was repeated without the use of any surface stabilizing agent. Briefly, a TrEG solution of $NaBH_4$ was used to co-reduce Au^{3+} and Pd^{2+} at room temperature, followed by refluxing for 1.5 hr. The XRD of the precipitated

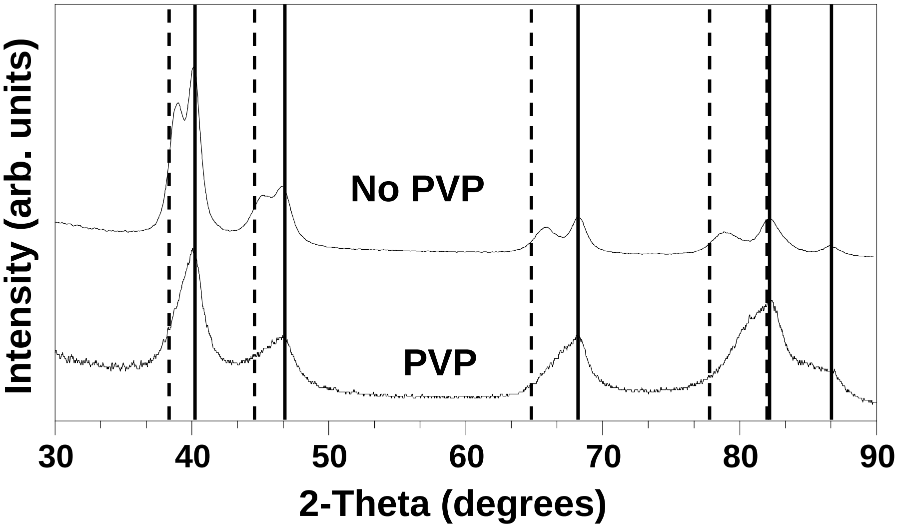

Figure 2.9 Powder XRD data of $AuPd_4$ synthesized in TrEG with and without the use of the surface stabilizing agent PVP. Dashed lines indicate positions of Au reflections and solid indicate those for Pd.

powders shows a two-phase product, the peaks of all reflections being clearly split and matching the lines pure Pd reflections (Fig. 2.9 top).

Phase-separate Pd seems to be a common product in the synthetic procedures carried out in pure TrEG, which may be a result of the stoichiometric excess, the less positive reduction potential of Pd (0.951 V) as compared to Au (1.498 V), and possibly the high viscosity of the solvent compared to water. However, co-reduction without PVP results in a phase separated product with narrow peaks resolvable by XRD, which likely means that less Pd is alloyed and the final particles are much larger. The use of PVP seems to promote alloy formation, an effect which has been experimentally observed to promote alloying in the Co-Pt system.[88] PVP has been reported to bind to metal cations and form coordination complexes,[89,90] and accordingly it may help to keep

Au^{3+} and Pd^{2+} cations in close proximity before reduction, which may translate into low-temperature alloy formation.

If a direct polyol process is used in which there are no added reducing agents or stabilizing agents, the product again appears phase-separated, however to a further extent. Figure 2.10 shows the XRD pattern of the direct polyol product which appears to be a composite of Au-Pd alloy and Pd, however the intensity of the Pd peaks is quite high and the peaks are much more narrow than in the previous experiment. In this case, because the reagents are added to the solution at room temperature and then heated, the Au is likely reducing before Pd, and the lack of any surface stabilizer allows aggregation and sintering of the powders, which is consistent with the sharper diffraction peaks. While some alloying is seen, the continued sintering may significantly slow solid-solid diffusion, and a large amount of pure Pd in the product is the result.

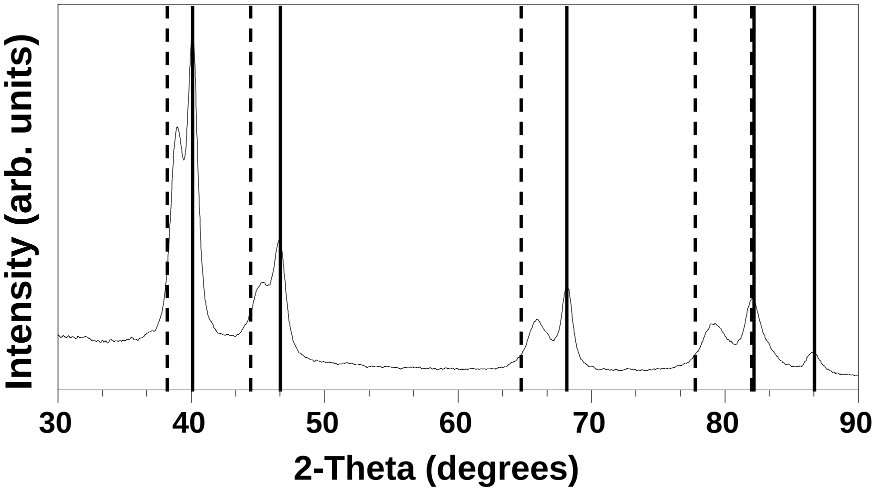

Figure 2.10 Powder XRD data of $AuPd_4$ synthesized by the direct polyol process in TrEG without the addition of PVP or $NaBH_4$. Dashed lines indicate positions of Au reflections and solid indicate those for Pd.

2.5 $AuPd_4$ catalyst design and catalytic activity

The documented catalytic activity of $AuPd_4$ alloy[82] inspired our investigation into the preparation of $AuPd_4$ powders. Our solution-based methods are advantageous for the preparation of catalytic materials because of their innate capacity to form nanocrystalline powders with high surface-area-to-volume ratios. Many reactions have shown that alloying with Au has demonstrated a significant promoter effect, increasing activity and selectivity,[53,83,85] and resistance to forming unwanted palladium carbides.[84] The catalytic activity of $AuPd_4$ was tested through collaboration with Yi-Fan Han in the Lunsford research group for the direct synthesis of H_2O_2 from H_2 and O_2, and also in collaboration with Praveen Boopalachandran in the Goodman research group for the vinyl acetate synthesis and CO oxidation reactions. While the surface chemistry of our nanocrystalline powder products is unknown, there is clear evidence that they can be useful active and selective catalysts.

Catalytic testing for the direct synthesis of H_2O_2 was conducted with $AuPd_4$ prepared by the aqueous co-reduction method with PVP. Pd clusters supported on SiO_2 are known to catalyze the formation of H_2O_2 from H_2 and O_2, and evidence exists that colloidal Pd is leached from the support and may become involved in the catalytic cycle.[91] Figure 2.11 shows the catalytic conversion and selectivity for H_2O_2 formation over our as-made colloidal $AuPd_4$ alloy catalyst.[47] The results show that H_2O_2 is produced from H_2 and O_2 using the PVP-stabilized alloy, which is clear evidence that surface sites are readily accessible on our colloidal materials. Importantly, the selectivity for H_2O_2 formation is 65% for our unsupported $AuPd_4$ catalyst. This is

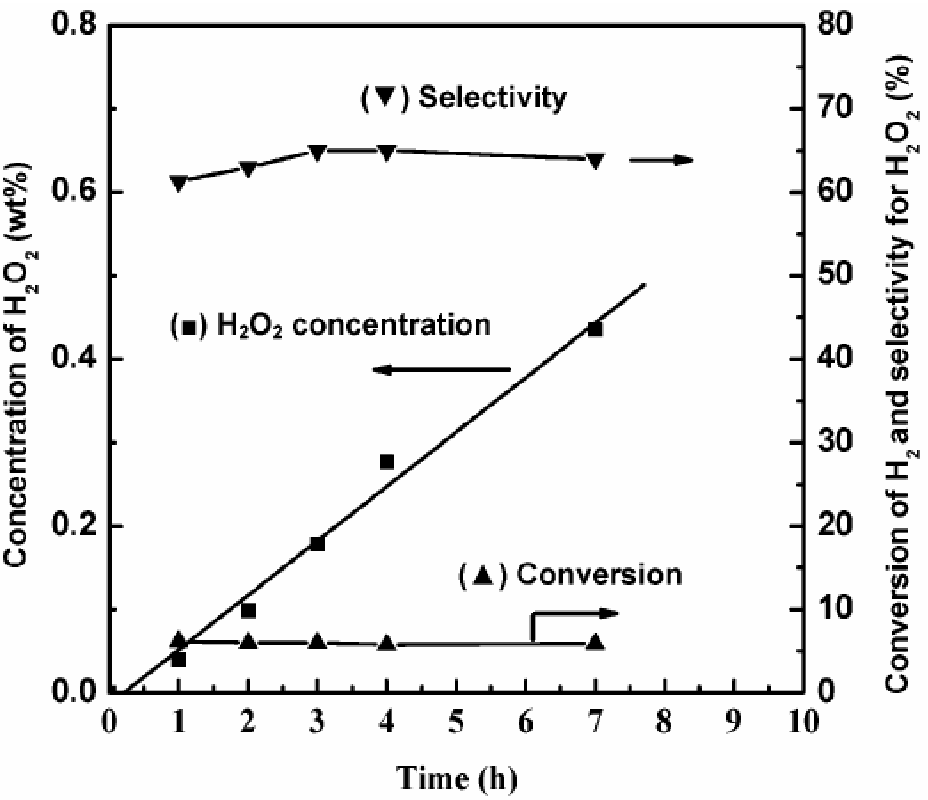

Figure 2.11 Catalytic formation of H_2O_2 at 10 °C in 0.24 N H_2SO_4/ethanol (60 mL) over a PVP-stabilized $AuPd_4$ catalyst (5 mg). The O_2:H_2 ratio was 4:1, and the flow rate was 50 mL/min. (Source: Schaak, *et al.*, 2005)

significantly larger than the 45% selectivity obtained from standard Pd/SiO_2-supported catalysts.[91] From this data, it is clear that the surface chemistries of our alloys are truly different from pure Pd and that they provide a clear advantage for catalytic purposes.

PVP stabilized $AuPd_4$ powders were also tested for the vinyl acetate (VA) synthesis and CO oxidation reactions, however the demonstrated activities and selectivities were less than satisfactory. Several factors may have influenced the poor catalytic results such as low surface area due to aggregation and PVP inhibition of surface site accessibility. Addressing the problem of aggregation first, we attempted to prepare supported nanocrystalline $AuPd_4$. Amorphous SiO_2 spheres (500 nm) were initially used as a support, and $AuPd_4$ was synthesized through the aqueous co-reduction method in the presence of PVP. Figure 2.12 shows the XRD patterns associated with adding the support to the reaction solution (a) before reduction with $NaBH_4$, (b) immediately after reduction, (c) 30 min after reduction, and (d) 2 hrs after reduction, followed by stirring overnight. The Au-Pd alloy product is seen only when the support is added at least 30 min after the co-reduction of Au^{3+} and Pd^{2+}, and a phase-separated product is seen when the support is added before or immediately after reduction. The fact that the support interrupts chemical alloying indicates that it may also prevent particle aggregation.

TEM analysis of the supported alloys from the 30 min and 2 hr additions show that particle aggregation is not completely avoided, but is limited. Figure 2.13 shows the supported Au-Pd alloy after adding the support (a) 30 min post-reduction, and (b) 2 hrs post-reduction. It appears in both cases that there are particle aggregates, however the two samples are distinctly different. Adding the support 30 min post-reduction results in spherical aggregates with a wide size dispersity, ranging from 20 to 80 nm, but also much smaller aggregates and possibly even single particles on the order of less that 5 nm to over 10 nm. Almost all the particles and aggregates are adsorbed to the surface of the SiO_2 support, most likely through van der Waals interactions. Upon investigation, there is a low coverage of the single particles and very small aggregates on the surface of the support spheres. Adding the support just 2 hrs post-reduction yields a distinctly different

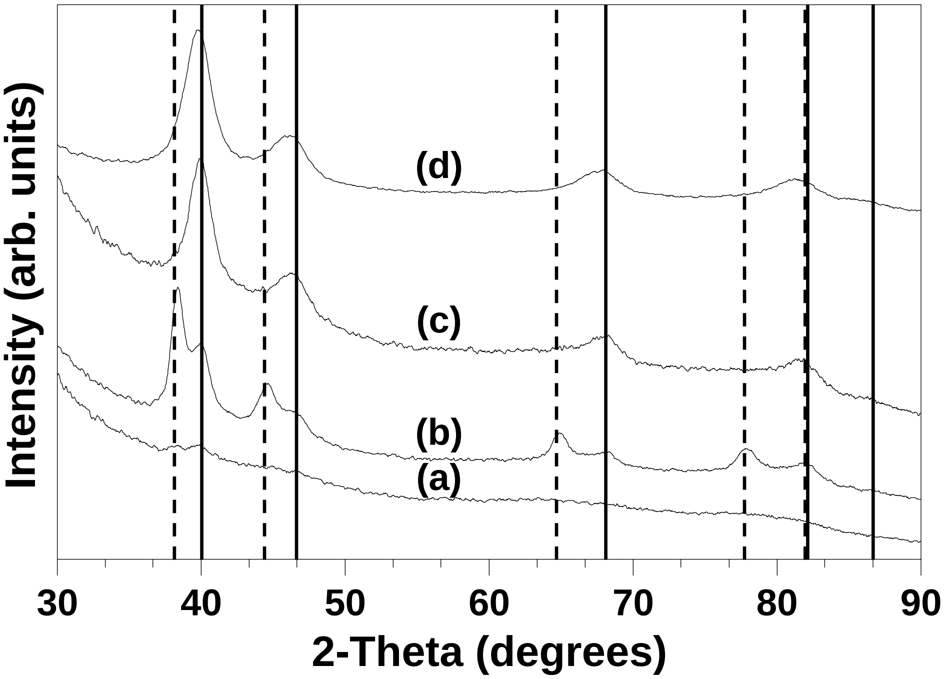

Figure 2.12 Powder XRD data of $AuPd_4$ synthesized by the nanocomposite route and supported on SiO_2 spheres. Diffraction patterns correspond to adding the support to the reaction solution (a) before reduction with $NaBH_4$, (b) immediately after reduction, (c) 30 min after reduction, and (d) 2 hrs after reduction. Dashed lines indicate positions of Au reflections and solid indicate those for Pd.

product, as the particle aggregates are much larger on average, with most ranging from 80 to 120 nm, however a few are as small as 30 nm. In contrast to the 30 min addition sample, the 2 hr addition lacks very few aggregates below 30 nm, and virtually no single particles are seen, as the particles likely had much more time to aggregate before adsorbing to the support surface. Selected area electron diffraction (SAED) of the 2 hr addition shows a simple fcc diffraction pattern (Fig. 2.13b inset), however it is difficult to tell if there is phase-separation due to the proximity of the d-spacings of the elemental metals.

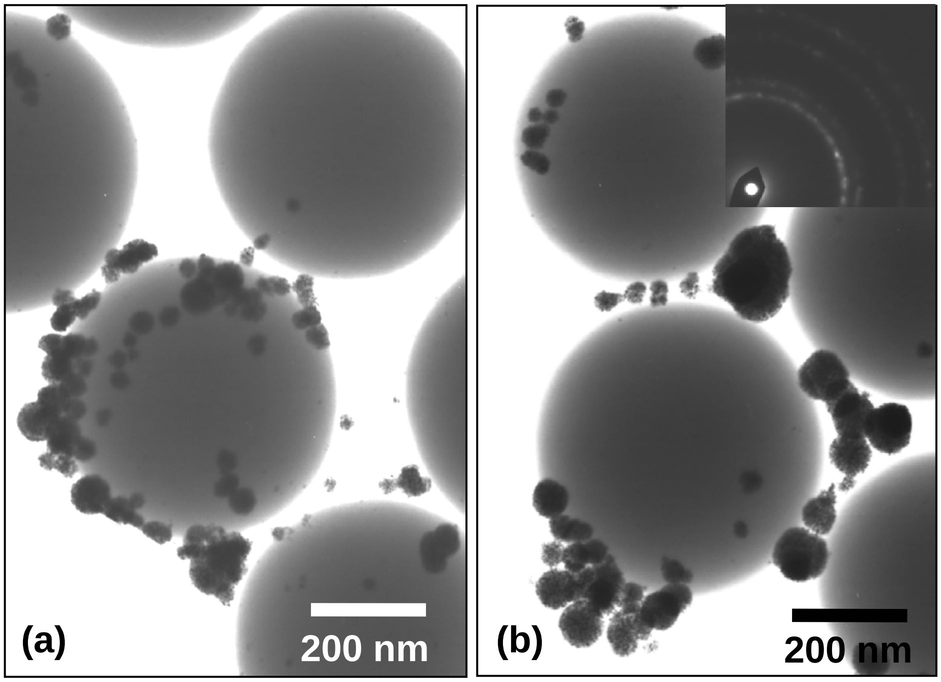

Figure 2.13 TEM images of $AuPd_4$ made by the nanocomposite route and supported on SiO_2 spheres that were added to the reaction solution (a) 30 min post-reduction, and (b) 2 hrs post-reduction. The SAED pattern inset in (b) shows the fcc structure of $AuPd_4$.

$AuPd_4$ was also synthesized in the presence of a non-polymeric stabilizer, sodium acetate (NaOAc). There are many examples of anion-stabilized colloidal synthetic techniques,[93] and potassium acetate is one of the components in industrial Au-Pd catalysts used for vinyl acetate synthesis.[94] Sodium acetate stabilized $AuPd_4$ was synthesized in aqueous solution by the $NaBH_4$ co-reduction method. Powder XRD of the product (Fig. 2.14) shows a simple fcc pattern with diffraction peaks at positions between those expected for Pd and Au. The peaks are quite broad, and therefore make it difficult to tell if the product is phase-pure. TEM analysis of the product (Fig 2.15) shows an interconnected mesh-like structure similar to that formed in TrEG without PVP

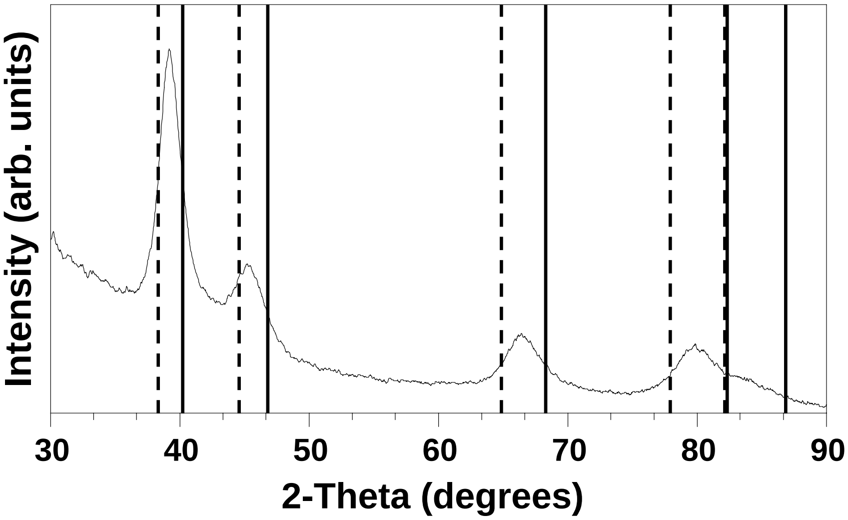

Figure 2.14 Powder XRD data of $AuPd_4$ synthesized by the nanocomposite route in the presence of sodium acetate. Dashed lines indicate positions of Au reflections and solid indicate those for Pd.

stabilizer. EDS analysis confirms that the atomic Pd:Au ratio is 79:21, indicating that Pd and Au are present in the correct ratio, however this does not verify that the product is a homogenous alloy. Interestingly, the particle sizes appear to range from 20 to 50 nm which is inconsistent with the broad XRD peaks. As a result, it is reasonable to hypothesize that the particles are either highly polycrystalline with small grain sizes, or that only a fraction of the sample is crystalline.

To increase prevent particle aggregation and increase particle surface area, acetate-stabilized $AuPd_4$ was synthesized in the presence of microporous SiO_2 catalyst support. The support was added to the aqueous reaction solution immediately before co-reduction, and was either allowed to stir or sit undisturbed for 3 days. The powder XRD (Fig. 2.16) shows very weak reflections for the products, although for each the 111 and

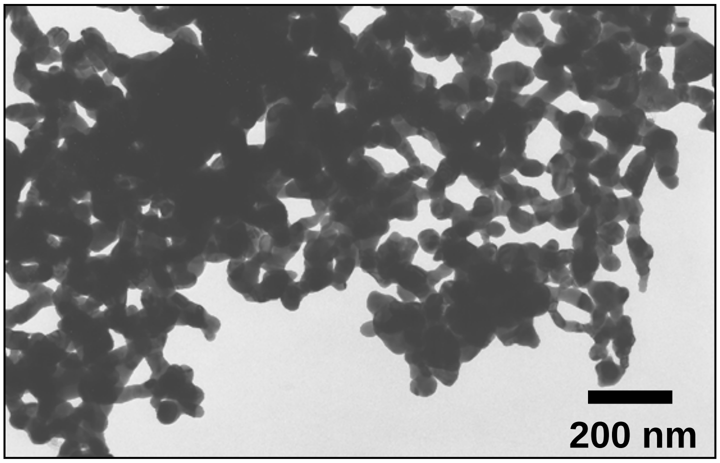

Figure 2.15 TEM image of $AuPd_4$ synthesized by the nanocomposite route in the presence of sodium acetate. EDS analysis yields an atomic Pd:Au ratio of 79:21.

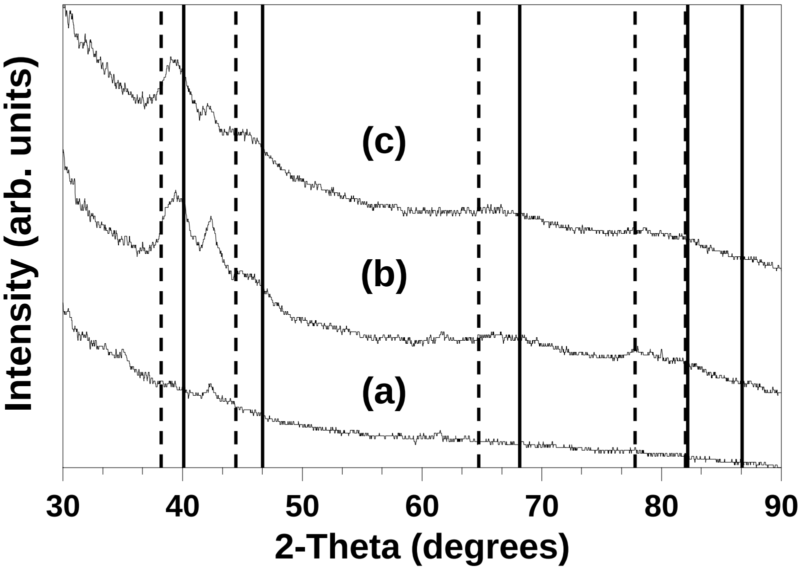

Figure 2.16 Powder XRD data of $AuPd_4$ synthesized by the nanocomposite route in the presence of sodium acetate and supported on porous SiO_2 catalyst support. Dashed lines indicate positions of Au reflections and solid indicate those for Pd. Peaks from the support can be seen at about 42 and 62 degrees 2θ.

200 reflections of an fcc diffraction pattern can be seen at intermediate angles between those expected for pure Au and Pd, indicating that Au-Pd alloy is present. TEM images of the supported particles made by allowing the solution to sit show particles of roughly 5 to 15 nm (Fig. 2.17), and the loading appears to be much higher than 5 wt%. The composition of the alloy cannot be determined from the XRD data, and EDS data was inconclusive as well due to the small signal of Au and Pd compared to the SiO_2 support. More powerful techniques such as XPS may be necessary to accurately determine the alloy composition.

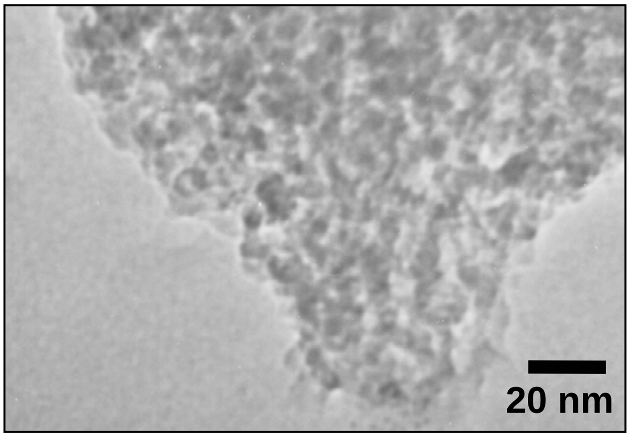

Figure 2.17 TEM images of $AuPd_4$ made by the nanocomposite route and supported on porous SiO_2 catalyst support.

The catalytic activity of nanocrystalline Pd and $AuPd_4$ stabilized by PVP was compared to SiO_2 supported $AuPd_4$, all formed via the aqueous nanocomposite route, for VA synthesis with good results. While PVP-stabilized $AuPd_4$ was much more active than PVP-stabilized Pd, the activity was still low. The reaction rates of $AuPd_4$ supported on SiO_2 spheres and porous catalyst support proved to be up to 4 times higher than unsupported PVP-stabilized $AuPd_4$ powder, and selectivities were increased as well. These results are consistent with the idea that the catalyst support prevents particle aggregation, keeping their surface area high and increasing the overall activity. PVP-stabilized $AuPd_4$ also showed activity for CO oxidation, with onset activity starting at roughly 100 °C and full conversion by 150 °C. Here, the activity was found to be dependent on the rate of temperature increase, where a faster rate results in lower onset temperature and full conversion temperature.

2.6 Summary

This chapter has presented several solution-based techniques to create both colloidal and supported Au-Pd alloy powders which may be useful catalysts for reactions such as direct H_2O_2 synthesis, VA synthesis and CO oxidation. The aqueous nanocomposite route relies upon the room-temperature co-reduction of Au and Pd chloride salts in the presence of the polymeric surface stabilizers PVP, PSS, PEO, PEG and P2E2O. The as-made products are generally nanocomposites with Au- and Pd-rich regions, however solid-solid diffusion can be induced via low temperature annealing (below 500 °C) in a tube furnace to yield single-phase alloys. The composition of the final alloy can be controlled quite well through careful synthesis, and final compositions calculated by way of Vegard’s Law are very close to the nominal stoichiometry of the initial reaction solution. Our results also show that the surface stabilizer has a clear effect on the chemical nature of the as-made product. By synthesizing $AuPd_4$ with a variety of polymeric surface stabilizers, phase-separated nanocomposites were produced with PSS and PVP, while the products produced with PEO, PEG and P2E2O appear to be single-phase alloys within the resolution of the X-ray diffraction data. Interestingly, upon annealing the alloys prepared with the latter three stabilizers have the closest calculated compositions to the nominal stoichiometry of 80 at.% Pd. These results may indicate that PEO, PEG and P2E2O are the weakest binding stabilizers[89] and may allow for more complete solid-solid diffusion upon reduction, which may translate into a more predictable final alloy composition.

We focused on the synthesis of $AuPd_4$ by different methods due to its known catalytic activity and selectivity. We have shown that $AuPd_4$ can be synthesized by the co-reduction of Au and Pd chloride salts in TrEG with a small amount of water at room temperature in the presence of PVP, followed by refluxing for 1-2 hrs. While DEG was also used as a solvent, the final composition of the alloy was Au-rich, and accordingly TrEG seems to be the most successful solvent for forming an $AuPd_4$ single-phase alloy. The use of $NaBH_4$ seems to be favorable, as it likely induces more simultaneous reduction of Au^{3+} and Pd^{2+} which aids in alloy formation. The use of PVP seems to be favorable as well, as it may inhibit particle growth and hold Au^{3+} and Pd^{2+} cations in close proximity prior to reduction, promoting alloy formation. The use of water as a co-solvent to aid in the dissolution of Pd is not necessary if using TrEG as the solvent, however adding water was successful in forming $AuPd_4$ alloy powders. The role of excess water in the reaction is unknown, but it may be insignificant with regard to the final alloy composition as refluxed glyol solvents are known to go through a dehydration step prior to the reduction of metal cations. Interestingly, the particles formed through the reaction with added water are discrete and fairly small, while those formed in pure TrEG are large and seem to be highly sintered.

Through collaboration, it was determined that the PVP stabilized $AuPd_4$ powders are catalytically active and are chemically different from pure Pd, as the formation of both H_2O_2 and VA showed increased activity and/or selectivity over pure Pd. However, due to the low activity of our powders compared to supported industrial standards, we hypothesized that particle aggregation may be decreasing the surface area and PVP may significantly passivate the surface, and the effects of each of these problems would result in decreased catalytic activity. In response, we designed supported $AuPd_4$ catalysts to prevent aggregation and replaced PVP with sodium acetate, which we hoped would act as a surface stabilizer as well as a catalytic promoter much like potassium acetate is known to. Using SiO_2 spheres as a support with PVP stabilized $AuPd_4$, we have shown that the support does reduce particle aggregation in comparison to unsupported powders, although the time at which the support is added to the reaction solution can have a significant effect upon the degree of aggregation. Adding the support 30 min after co-reduction seems to allow enough time for alloy formation while still maintaining several single particles or only very small aggregates. Replacing PVP with NaOAc, we were able to produce nanocrystalline powders that do contain Au-Pd alloy, however they may not be phase-pure. As hoped, catalytic activity of supported $AuPd_4$ powders were in fact increased, which is consistent with the ideas of increasing surface area and active surface sites. Because of the known catalytic activities of Au-Pd alloys, the ability to produce supported and unsupported nanocrystalline Au-Pd alloy powders through solution routes with controlled composition is an important step to rationally designing catalysts with high activity and selectivity.

CHAPTER III

MODIFIED POLYOL SYNTHESIS AND CHARACTERIZATION OF NANOCRYSTALLINE *M*-Sn & Pt-*M'* INTERMETALLICS*

3.1 Introduction

Intermetallic compounds are important materials for their diverse range of physical and chemical properties,[95] and accordingly, intermetallic compounds are desirable for wide range of applications. Examples of applied atomically ordered intermetallic materials include Nb_3Sn, a superconducting material (T_C = 18 K)[96] being produced on an industrial scale for devices. FePt is an important compound for the magnetic recording industry because of its high magnetocrystalline anisotropy and stability.[2,3] PtBi and PtPb have been studied as catalytic materials for fuel cells, and both have shown enhanced electrocatalytic activity compared to pure Pt and are virtually immune to CO poisoning.[4] Intermetallics are also highly relevant for magnetic,[2,3] shape-memory,[27] magnetoresistant,[97] thermoelectric,[14,26,31] and corrosion resistant applications,[25,61,95] as well as solid-state hydrogen storage.[29] Future technologies will require materials with unique and efficient properties, and continued research and development on functional intermetallic compounds is crucial.

---

* Reprinted in part with permission from *Chem. Mater., 17* Cable, R. E.; Schaak, R. E. "Low-Temperature Solution Synthesis on Nanocrystalline Binary Intermetallic Compounds Using the Polyol Process," 6835, Copyright 2005 by the American Chemical Society.

There are many successful techniques available for the synthesis of bulk intermetallic compounds, however they generally require high temperatures and long reaction times which may span from days to weeks. To continue using intermetallics in new technologies for devices that continue to decrease in size, nanocrystalline or low-dimensional materials will be necessary for their processability. Unfortunately, traditional solid-state routes to intermetallics usually form only thermodynamically stable phases and yield large particles, which are impractical for integration into many new and emerging technologies. Low-temperature and metastable compounds may have new structures and new or enhanced properties, and forming these compounds through traditional methods can be very challenging. It is also clear that the size and morphology of nanomaterials can significantly influence their physical and chemical properties,[1,5,6,11] and traditional high-temperature metallurgical synthetic methods make it difficult to control these critical factors.

Solution-based routes to intermetallics are highly advantageous relative to traditional synthetic methods for several reasons, including providing straightforward access to nanocrystalline powders. There are many solution chemistry strategies for controlling particle sizes for single- and multi-metallic materials,[6,36] and shape control for single-metal and metal-oxide products is well known.[34,36,37,39,40] Nanomaterials produced through solution routes are also often dispersable in solution, allowing them to be processed into thin films[46] or templated to adopt highly specific structures.[47,48] While there are many known strategies for the preparation of nanocrystalline single metals, chalcogenides,[97] and metal-oxides,[20,22] very little has been reported for solution-based routes to nanocrystalline intermetallic compounds.

One very common solution-based route to nanocrystalline metal powders, known as the polyol process, uses high boiling point polyalcohol solvents to precipitate nanocrystalline metal powders from metal salt and metal oxide precursors.[56,57] Using the polyol process, we have found that intermetallics can be accessed directly in solution in a short amount of time and at low temperatures.[35,48] Work in the Schaak group has also shown that metastable and new phases can be synthesized by the polyol process,[42,45] demonstrating its utility in controlling reaction kinetics. Here, we show that the polyol process is general for the rapid low-temperature synthesis of nanocrystalline intermetallics, successfully yielding phase-pure binary intermetallics in the *M*-Sn (*M* = Ag, Au, Co, Cu, Fe, Ni), Pt-*M'* (*M'* = Bi, Pb, Sb, Sn), and Co-Sb systems. These systems were chosen because (a) the Sn-based systems show a variety of interesting magnetic, electronic, and electrochemical properties,[22,60,95-97] (b) the Pt-based systems are of interest for their catalytic properties,[4] and (c) the Co-Sb system has known size-dependent thermoelectric properties.[31] In addition to the known phases that can be formed, these results have important implications for possibly synthesizing new and metastable intermetallics using low-temperature solution methods. Also, since a variety of modifications to the polyol process are known to yield well-formed monodisperse nanocrystals,[2,34] it is reasonable to anticipate similar morphological control for intermetallic systems. This would impact fields such as magnetic information storage, nanoscale electronics, self-assembled nanocomposites, and catalysis, for which the limited number of existing intermetallic nanocrystals are known to yield superior properties.

3.2 Experimental details

3.2.1 *Materials*

The following metal reagents were used: $SnCl_2$ (anhydrous, 99% min.), $Sn[CH_3(CH_2)_3CH(C_2H_5)CO_2]_2$, $Cu(C_2H_3O_2)_2·H_2O$ (98.0-102.0%), $HAuCl_4·3H_2O$ (99.99%), $AgNO_3$ (99.9+%), K_2PtCl_6 (40.11% Pt), $Ni(C_2H_3O_2)·xH_2O$ (99+%), $SbCl_3$ (99.9%), $Co(C_2H_3O_2)_2·4H_2O$ (98.0-102.0%), $Fe(acac)_3$, $Pb(C_2H_3O_2)_2·3H_2O$ (99.0-103.0%), and $Bi(NO_3)_3·5H_2O$ (Mallinckrodt Chemical Works). The reducing agent, surface stabilizer, and solvent were $NaBH_4$ (98%), poly(vinyl pyrrolidone) (PVP, MW = 40 000), and tetraethylene glycol (TEG, 99+%), respectively. All chemicals were purchased from Alfa Aesar unless otherwise noted.

3.2.2 *Synthesis*

The nanocrystalline intermetallic powders were synthesized by a modified polyol process, which has been previously reported.[30,38] For the *M*-(Sn,Pt) systems, the metal reagent was dissolved in 20 mL of TEG by sonication and magnetic stirring. $SnCl_2$, $Sn[CH_3(CH_2)_3CH(C_2H_5)CO_2]_2$ (for *M*-Sn) or K_2PtCl_6 (for *M'*-Pt), and PVP (170 mg) were then sequentially dissolved in a similar manner (see Table 1 for details). After the solution was vigorously stirred at room temperature under bubbling Ar for at least 45 min, 25 mg of $NaBH_4$ freshly dissolved in 5 mL TEG was added slowly. Upon reduction, the solution usually turned a dark brown or black color, and was then heated to the desired temperature (see Table 1). During the course of the reaction, 1.0 mL aliquots of the heated solution were collected to determine the appropriate reaction temperatures for intermetallic phase formation. Powders were precipitated from solution by centrifugation and were washed thoroughly with ethanol.

3.2.3 *Characterization*

Powder X-ray diffraction (XRD) data were collected on a Bruker GADDS three-circle X-ray diffractometer (Cu Kα radiation). XRD data were also acquired using a Bruker AXS D8 Advance powder X-ray diffractometer (Cu Kα radiation). Transmission electron microscopy (TEM) images, selected area electron diffraction (SAED) patterns, and energy-dispersive X-ray analysis (EDS) were collected using a JEOL JEM-2010 TEM. Samples were prepared by sonicating the nanocrystalline intermetallic powders in ethanol and dropping a small volume onto a carbon-coated nickel grid. Scanning electron microscopy (SEM) images were acquired using a JEOL JSM-6400 SEM. X-ray photoelectron spectroscopy (XPS) data were collected on a Kratos Ultra Axis Hsi 165 XPS using an Al anode set at 15 mA and 15 kV. Samples were prepared by sonicating the powder in ethanol and drop-coating a small volume onto a clean Si wafer. Differential scanning calorimetry (DSC) data were collected on a TA Instruments Q600 SDT under Ar. CHN analysis was performed by Atlantic Microlabs (Norcross, GA). Further solid-state composition analysis was carried out on a four spectrometer Cameca SX50 electron microprobe.

3.3 Synthesis of nanocrystalline binary intermetallic powders

TEG was used as a high-boiling solvent (T_{BP} = 310 °C) to allow for the one-pot solution synthesis of nanocrystalline binary intermetallic compounds.[34] The intermetallics are synthesized by dissolving the reagents in TEG, reducing them at room temperature with $NaBH_4$, and heating them to various temperatures between 100 and 300 °C. Control experiments were conducted in which the metal salt solutions were heated without the addition of $NaBH_4$, and the products observed were phase-separated composites or alloys, confirming the necessity of $NaBH_4$ reduction for intermetallic formation. Aliquots taken at regular intervals provide information about phase formation, and often several distinct phases are observed during the reaction, depending on the temperature and time. The products formed upon reduction and prior to heating are generally multi-phase, and the intermetallic phases are usually formed by 120 °C. The reaction times are typically very short, often requiring only the amount of time necessary to reach the final reaction temperature. The final products tend to contain 2 – 5 wt% of polymer residue, as determined by CHN analysis of several samples.

To demonstrate the breadth of this synthetic technique for accessing nanocrystalline binary intermetallics, we chose to focus on the *M*-Sn (*M* = Ag, Au, Co, Cu, Fe, Ni), Pt-*M*' (*M*' = Bi, Pb, Sb, Sn), and Co-Sb systems. Table 3.1 presents a summary of the reagents and temperatures necessary to form phase-pure intermetallics in these systems, and Figure 3.1 shows representative XRD data for the intermetallic products. XRD data for selected *M*-Sn phases are shown in Figure 3.1a. All of these compounds are pure phases, within the detection limits of our laboratory diffractometer,

Table 3.1 Details for the synthesis of nanocrystalline *M*-Sn, Pt-*M'*, and Co-Sb intermetallic powders.

Intermetallic Species	Reagents	Reaction Molarity in *M* (mM)	*M* : *M'* Reaction Ratio*	Intermetallic Phase Formation Temperature (°C)
Ag_4Sn	$AgNO_3$, Tin(II) 2-ethylhexanoate	4.4 mM in Ag	1.0 : 1.0	175 °C
Au_5Sn	$HAuCl_4•3H_2O$, Tin(II) 2-ethylhexanoate	4.2 mM in Au	1.0 : 1.0	175 °C
Co_3Sn_2, CoSn	$Co(OOCCH_3)_2•4H_2O$ $SnCl_2$	4.3 mM in Co	1.0 : 4.0	200 °C, 260 °C
Cu_6Sn_5, $Cu_{40.5}Sn_{11}$	$Cu(OOCCH_3)_2•H_2O$ $SnCl_2$	4.3 mM in Cu	1.0 : 5.0	125 °C, 275 °C
$FeSn_2$	$Fe(acac)_3$, $SnCl_2$	4.4 mM in Fe	1.0 : 5.9	125 °C
Ni_3Sn_4	$Ni(OOCCH_3)•xH_2O$ $SnCl_2$	5.2 mM in Ni	1.0 : 4.4	190 °C
PtBi	$Bi(NO_3)_3•5H_2O$ K_2PtCl_6	4.0 mM in Bi	1.0 : 1.0	220 °C
PtPb	$Pb(OOCCH_3)_2•3H_2O$ K_2PtCl_6	4.5 mM in Pb	1.1 : 1.0	150 °C
PtSb	$SbCl_3$, K_2PtCl_6	4.7 mM in Sb	1.0 : 1.0	200 °C
PtSn	$SnCl_2$, K_2PtCl_6	23.0 mM in Sn	4.3 : 1.0	230 °C
CoSb	$Co(OOCCH_3)_2•4H_2O$	5.7 mM in Co	1.0 : 3.0	175 °C
$CoSb_3$	$SbCl_3$	4.6 mM in Co	1.0 : 4.5	240 °C

* For *M*:Sn phases, *M* = (Ag, Co, Cu, Fe, Ni) and *M*' = Sn; for Pt-*M'* phases, *M* = Pt and *M*' = (Bi, Pb, Sb, Sn); for Co-Sb phases, *M* = Co and *M*' = Sb.

and agree well with simulated XRD patterns based on prior literature reports. Au_5Sn, a known superconductor with $T_c = 2$ K,[99] and Ag_4Sn can be stabilized at 175 °C. These alloys crystallize in the Mg structure type (hcp), which Ag, Au, and Sn do not adopt. Al_2Cu-type $FeSn_2$, which is an antiferromagnet with a known thickness dependence of T_N in thin films,[30] forms as a pure phase upon heating for 30 min at 130 °C. Monoclinic Ni_3Sn_4 forms at 195 °C, which is significant because of the potential for using

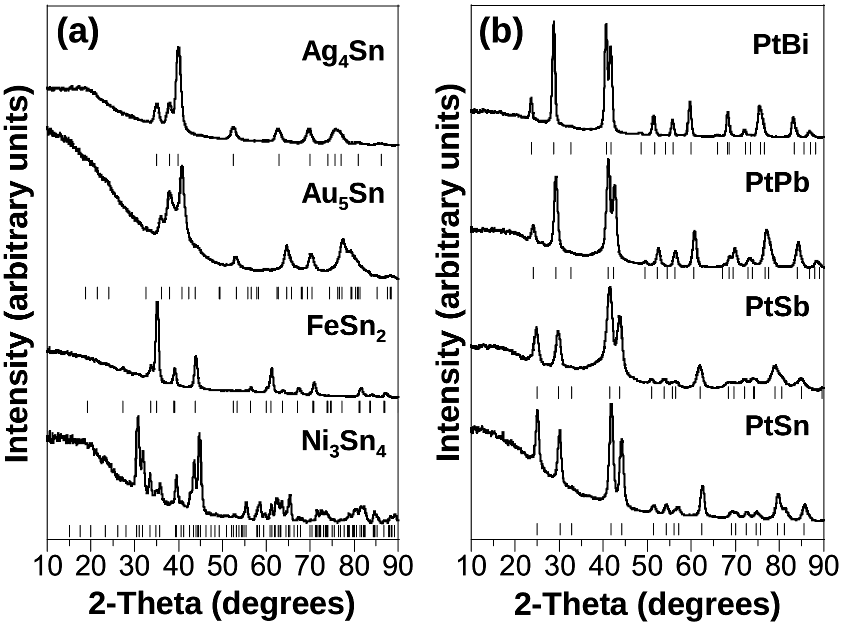

Figure 3.1 Powder XRD patterns for nanocrystalline intermetallics (a) *M*-Sn [Ag_4Sn, Au_5Sn, $FeSn_2$, Ni_3Sn_4] and (b) Pt-*M'* [PtBi, PtPb, PtSb, PtSn]. Tick marks below each pattern represent allowed reflections for each compound.

nanocrystalline Ni_3Sn_4 as an anode material in Li-ion batteries.[60] Nanocrystalline Ni_3Sn_4 was previously produced by ball milling for up to 30 hours,[60] and a direct solution route to a similar material may prove useful for battery applications.

Similarly, Pt-*M'* intermetallics can also be synthesized using this rapid low-temperature solution approach (Figure 3.1b). As expected based on their respective binary phase diagrams, PtBi, PtPb, PtSb, and PtSn adopt the NiAs structure type.[100] PtBi and PtSn, of interest for their catalytic properties,[4,9,101] form phase-pure intermetallics near 250 °C. PtPb has shown a superconducting transition with T_c = 7.2 K in layered thin films,[102] and we were able to access this phase at 165 °C. PtSb can be stabilized by 200 °C. In addition to the *M*-Sn and Pt-*M'* systems, other binary intermetallic systems

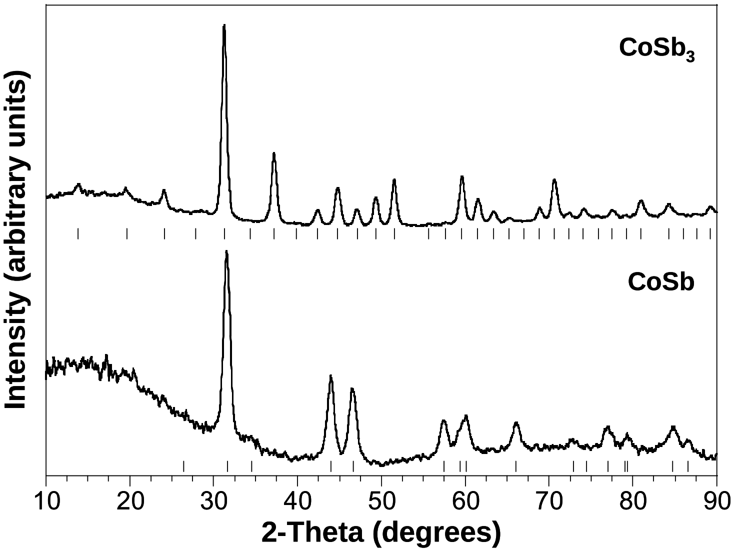

Figure 3.2 Powder XRD patterns for (top) CoSb$_3$ and (bottom) CoSb. Tick marks below each pattern represent allowed reflections for each compound.

can be accessed. For example, CoSb and CoSb$_3$ can both be accessed in the Co-Sb system (Figure 3.2). CoSb$_3$ is a well-known thermoelectric prototype,[26] and reports have shown enhanced thermoelectric properties as the particle size decreases.[31] Methods for making nanocrystalline CoSb$_3$, however, typically require ball milling or solvothermal reactions with reaction times of 72 h.[14]

The Co-Sb system (Figure 3.2) demonstrates that multiple phase-pure intermetallics can be accessed in the same system. However, in some cases, two distinct intermetallic compounds can be synthesized in a single reaction with a fixed nominal composition. For example, in the Cu-Sn system (Figure 3.3), a 1:5 ratio of Cu:Sn yields NiAs-type Cu$_5$Sn$_6$ at 125 °C and Cu$_{41}$Sn$_{11}$ at 275 °C. As the solvent temperature increases beyond 125 °C, more Cu is incorporated into the Cu$_5$Sn$_6$ lattice, and Cu$_{41}$Sn$_{11}$

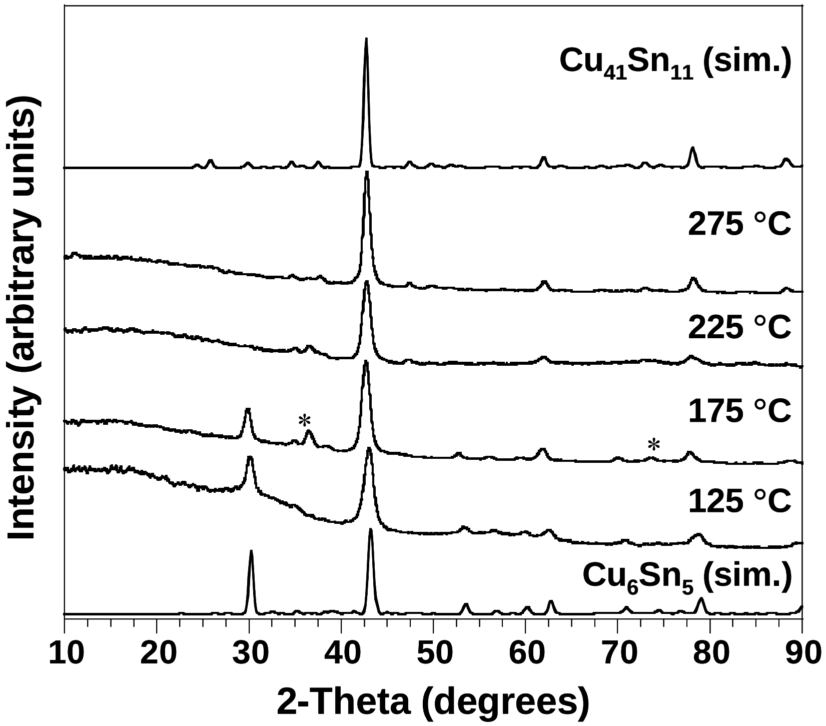

Figure 3.3 Powder XRD patterns for the products isolated as a function of heating temperature in the Cu-Sn system, along with simulated patterns (based on literature references) for (bottom) Cu_6Sn_5 and (top) $Cu_{41}Sn_{11}$. At 125 °C, the pattern matches that of Cu_6Sn_5. Upon further heating in the presence of tin, the pattern transforms to that expected for $Cu_{41}Sn_{11}$, indicating additional tin incorporation in the crystalline product. (The peaks near 36.5 and 73.7° 2θ in the intermediate-temperature samples, labeled with an asterisk (*), correspond to a Cu_2O impurity, which results from nanocrystalline Cu that has oxidized during sample handling under ambient conditions.)

begins to nucleate by 175 °C. As the temperature is raised further, more Cu is incorporated, and $Cu_{41}Sn_{11}$ becomes a pure phase.

A very similar reaction occurs in the Co-Sn system, as Co_3Sn_2 is stabilized at a lower temperature, while CoSn can be stabilized at a higher temperature. Figure 3.4 shows temperature-dependent XRD data for the Co-Sn system, along with simulated XRD data for Co_3Sn_2 and CoSn. The corresponding reaction is shown schematically in Figure 4a. As in the Cu-Sn system, the formation of Co_3Sn_2 *vs.* CoSn can be controlled

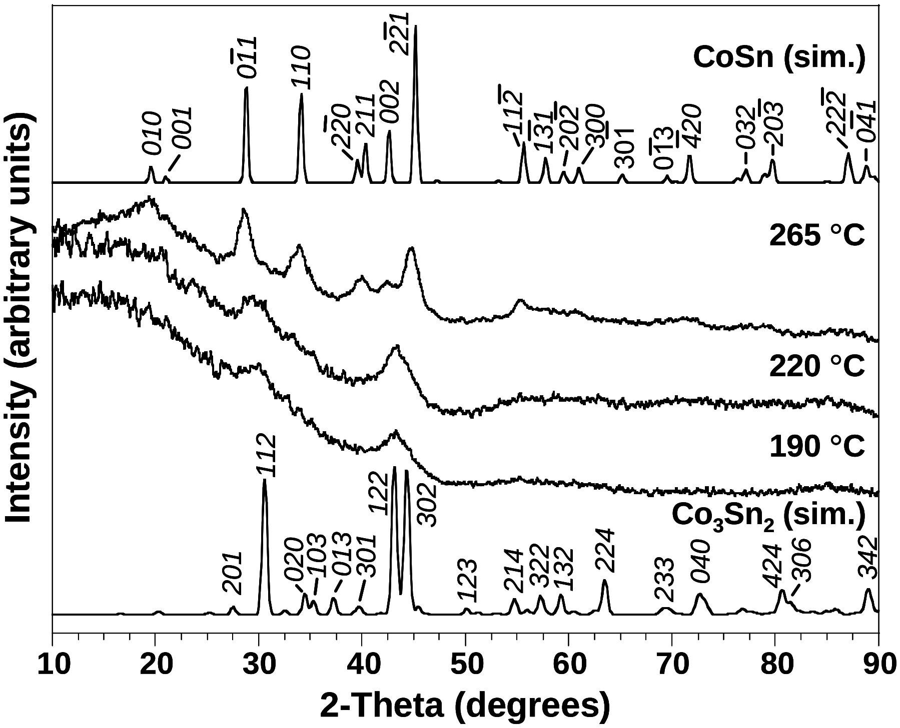

Figure 3.4 Powder XRD patterns for the products isolated as a function of heating temperature in the Co-Sn system, along with simulated patterns (based on literature references) for (bottom) Co_3Sn_2 and (top) CoSn. Between 190 and 200 °C, the pattern matches closely with that expected for Co_3Sn_2. Upon further heating in the presence of tin, the pattern transforms to that expected for CoSn, indicating additional tin incorporation in the crystalline product.

by temperature when the same ratio of reactants is used (1:4 for the Co-Sn system). At 190 °C, the solution with a nominal stoichiometry of Co_1Sn_4 forms a crystalline product that matches that of Co_3Sn_2. The peaks are broad, but the most intense peaks of Co_3Sn_2 match those observed for the sample heated to 190 °C. Furthermore, the SAED pattern for Co_1Sn_4 heated to 190 °C (Figure 3.5a) matches that expected for Ni_3Sn_2-type Co_3Sn_2, indicating that Co_3Sn_2 is indeed the crystalline phase, and the peak broadening in the XRD data is due to nanocrystalline domains. (This is confirmed by TEM micrographs

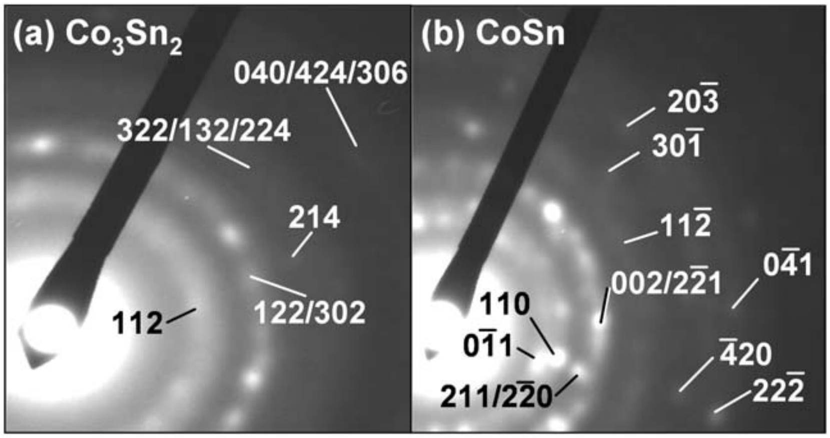

Figure 3.5 Selected-area electron diffraction patterns for nanocrystalline (a) Co_3Sn_2 and (b) CoSn.

of the particles, which will be discussed later.) Upon further heating of the nominal Co_1Sn_4 sample, the nanocrystalline Co_3Sn_2 phase converts to CoSn. The XRD pattern for nanocrystalline CoSn matches the simulated data, and the SAED pattern is also consistent with the formation of CoSn (Figure 3.5b). These data clearly support the idea that the formation of two distinct crystalline phases in the same system can be controlled entirely by temperature, and that this reactivity is facilitated by the nanocrystalline phases and the low-temperature solution environment. Such rapid low-temperature reactivity is unprecedented for bulk solid-state systems.

3.4 Study of phase formation in the Fe-Sn system

The solution-mediated reaction of the Fe-Sn system was studied in detail by XRD to gain insight into the reaction mechanism. A TEG solution of Fe and Sn salts in a 1:6 molar ratio was reduced at room temperature and subsequently heated, and aliquots

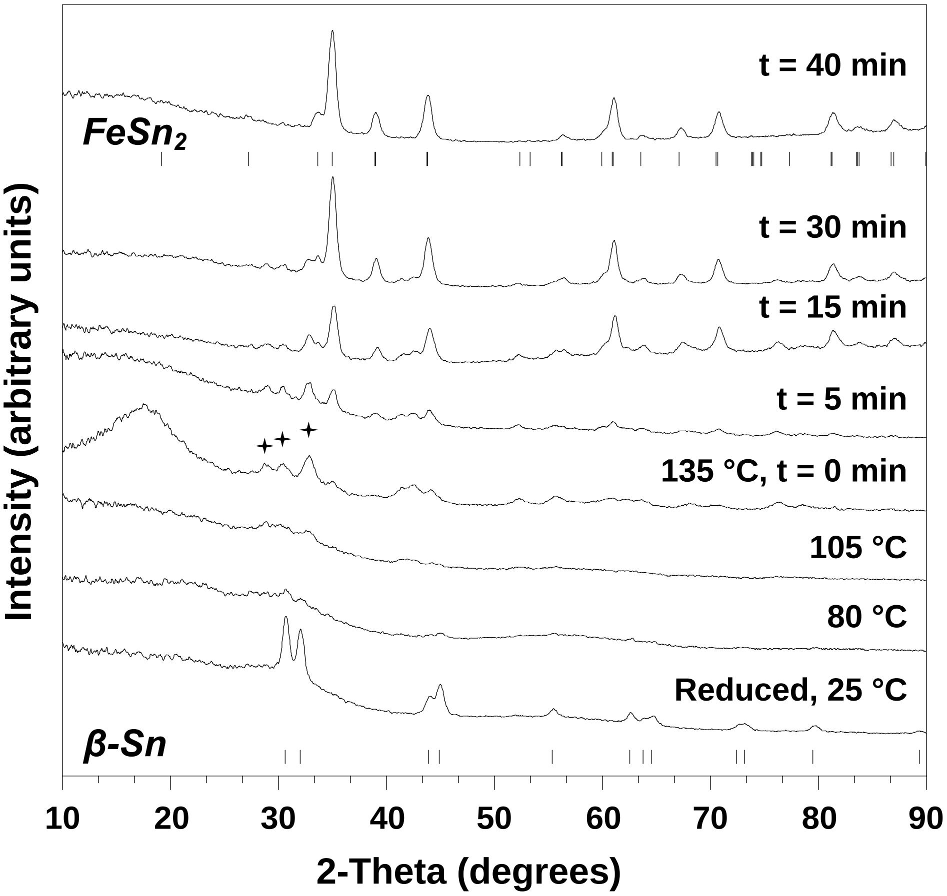

Figure 3.6 Powder XRD patterns for the products isolated as a function of heating temperature in the Fe-Sn system, along with tick marks representing the angles of reflections for *β*-Sn (bottom) and $FeSn_2$ (top). When heated to 135 °C, a new set of reflections can be seen from 29-33 degrees 2*θ* (marked by +) that do not match any reported phase in the Fe-Sn system. After heating at 135 °C for 40 min, the $FeSn_2$ intermetallic phase is formed and the crystalline intermediate is not observed.

of the reaction solution were taken at various temperatures and times during the reaction. The solids were precipitated from these aliquots and XRD analysis yielded very interesting results (Fig. 3.6). At low temperatures, *β*-Sn is observed, with no trace of Fe. As the reaction temperature increases, the broad pattern suggests that the particles in the colloidal suspension are amorphous, as Fe may be diffusing into the Sn lattice, and the

$FeSn_2$ intermetallic is formed after holding the reaction at 135 °C for 20 minutes. However, at roughly 100 °C a crystalline phase begins to appear which could not be matched to any known Fe or Sn species, including intermetallics and alloys, or any oxide, carbide, nitride, or hydride impurities. The crystalline phase continues to grow in intensity and sharpen until the reaction reaches about 130 °C, then the phase disappears over the course of about 15 minutes. The major reflections of the phase can be seen at 29, 31, and 33 degrees 2θ.

In an effort to synthesize the unknown intermediate in pure phase by XRD, a systematic study was conducted in which reagent concentrations (including Fe, Sn, and BH_4^-) and reduction temperatures were changed in co-reduction reactions. Solutions containing Fe:Sn ratios of 1:2, 1:4, and 1:6 were reduced at temperatures of 60, 80, and 100 °C and heated with aliquots drawn every 20 minutes. The reduction at high temperature was a change in the standard synthetic procedure, however it yielded the best results for the synthesis of the intermediate product. The results of the systematic study showed that the 1:4 ratio successfully formed the intermediate when reducing at 80 °C and heating for at least 1 hour, and the 1:6 ratio was successful when reducing at 80 and 100 °C and holding for at least 1 hour (Fig. 3.7). The 1:6 ratio seemed to be the most successful, although $FeSn_2$ impurities are clearly present when reduced and held at 100-125 °C, and the intermetallic phase becomes more prevalent with reaction time.

Further experiments with the 1:6 ratio showed that reducing at 80 °C and quickly heating to 125 °C produced the unknown intermediate seemingly phase-pure (Fig 3.8). Holding the reaction for even a few minutes at 125 °C resulted in the growth of $FeSn_2$,

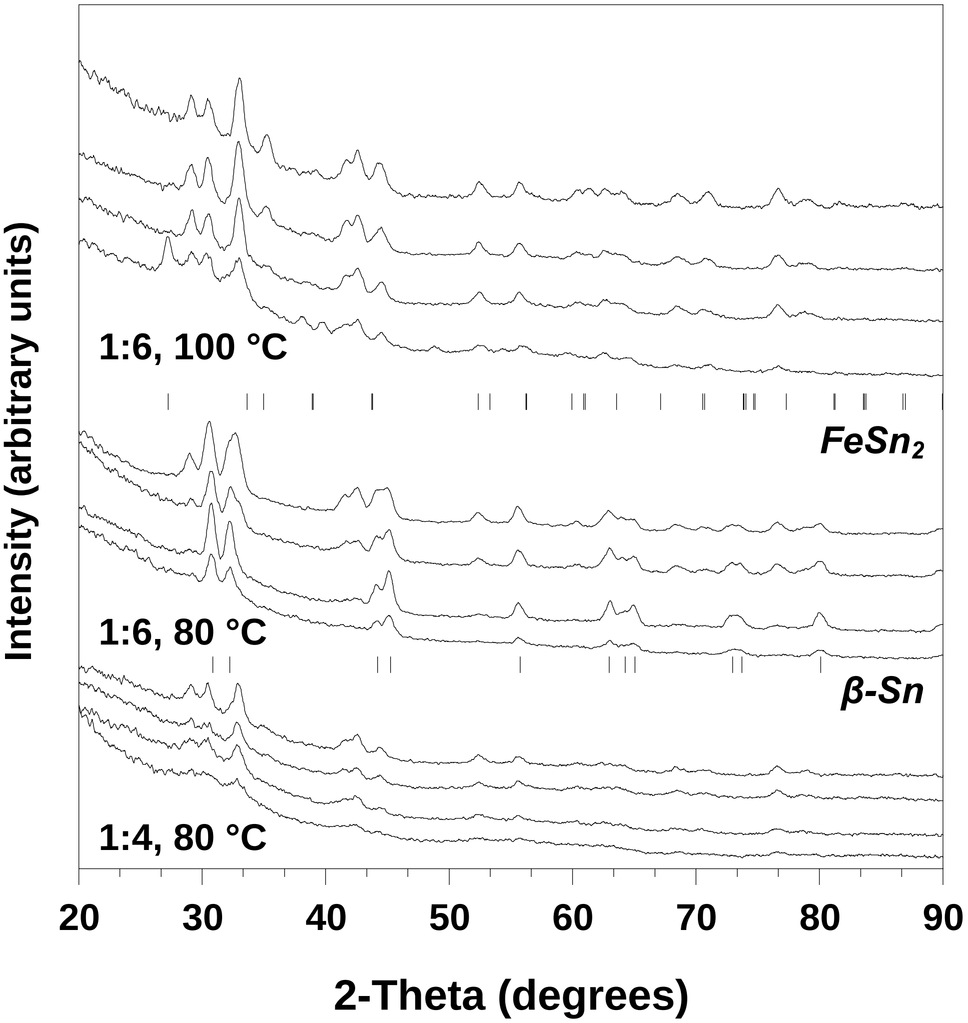

Figure 3.7 Powder XRD patterns for the products isolated as a function of molar ratio (Fe:Sn), reduction temperature, and heating time in the Fe-Sn system, along with tick marks representing the angles of reflections for *β*-Sn (bottom) and $FeSn_2$ (top). For each different reaction the XRD patterns correspond to the product isolated from 0.5 hr (bottom patterns) to 2 hr (top patterns) in 0.5 hr intervals.

so in order to form the intermediate phase-pure, it must be quenched when the reaction temperature reaches 125 °C. A large amount of what was believed to be the pure unknown phase was synthesized (XRD Fig. 3.9a, TEM Fig. 3.9b), and electron microprobe analysis was employed to extract analytical quality elemental analysis from

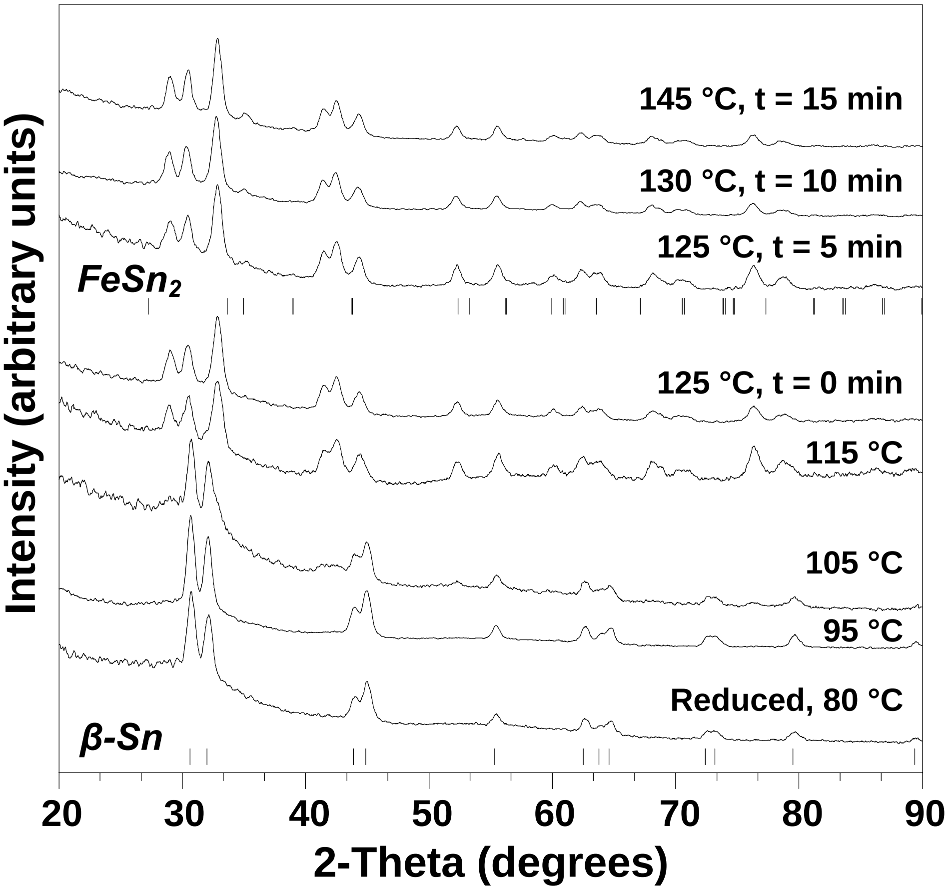

Figure 3.8 Powder XRD patterns for the products isolated as a function of heating temperature and time in the Fe-Sn system (1:6 molar ratio) which was reduced with $NaBH_4$ at 80 °C, along with tick marks representing the angles of reflections for *β*-Sn (bottom) and $FeSn_2$ (top). Quenching the product at 125 °C yields the intermediate phase-pure. Continued heating from 125-145 °C results in the nucleation of $FeSn_2$.

the product. From the backscattered electron micrsocopy image (Fig 3.10), we conclude that the sample is somewhat inhomogenous from the clear variation in contrast in different areas of the sample, corresponding to areas with different amounts of heavy (lighter contrast) and light (darker contrast) elements. Comparing the electron microscopy micrograph to the elemental analysis of the specific areas showed that although image contrast shifted, the atomic concentration of Sn, Cl and light elements

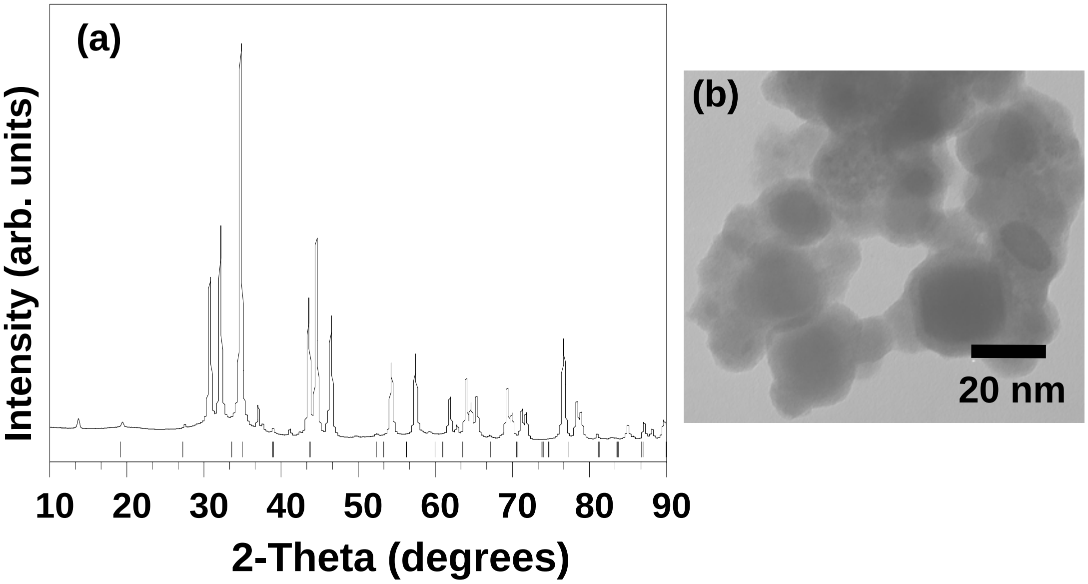

Figure 3.9 (a) Synchrotron diffraction of Fe-Sn intermediate isolated from the reduction of an Fe-Sn solution (1:6 molar ratio) at 80 °C, then heated and quenched immediately at 125 °C. Tick marks correspond to allowed reflections of FeSn2, showing that very little of the FeSn$_2$ intermetallic is present. (b) TEM image of Fe-Sn intermediate compound.

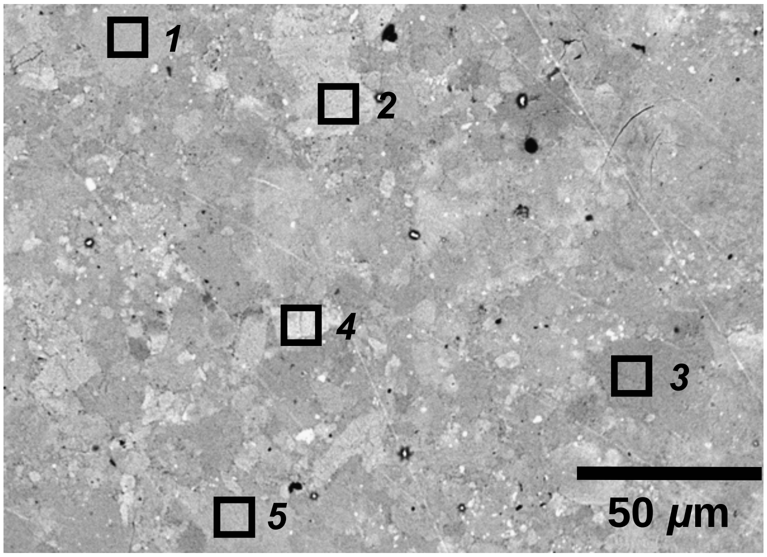

Figure 3.10 Backscattered electron image from electron microprobe analysis on Fe-Sn intermediate sample (Figure 3.9). The numbered boxes correspond to the areas in which elemental analysis was performed, with the results being listed in Table 3.2.

Table 3.2 Elemental composition of the Fe-Sn intermediate corresponding to different regions of the backscattered electron image (Fig. 3.10).

REGION		Sn	Fe	Cl	Undefined light element
1	Wt %	81.031	4.531	0.547	13.891
	At % (norm)	35.267	4.191	0.797	59.745
2	Wt %	81.897	4.649	1.082	12.372
	At % (norm)	37.626	4.540	1.665	56.169
3	Wt %	79.883	4.541	0.424	15.134
	At % (norm)	33.203	4.011	0.589	62.159
4	Wt %	82.828	4.607	0.778	11.787
	At % (norm)	39.126	4.625	1.231	55.018
5	Wt %	80.282	4.662	0.569	14.479
	At % (norm)	34.132	4.212	0.810	60.831

(B, C, N, O) varied slightly to significantly, while the concentration of Fe changed very little (Table 3.2). The atomic ratio of Sn to Fe varied only slightly from 8.1 to 8.5.

Through analysis of the XRD data with the help of Dr. N. Bhuvanesh, it was determined that the powder XRD pattern may be indexed to a single phase with a $P4_2/m$ space group and lattice constants of a = 3.0856 and c = 5.8890 (Fig 3.11). However, structure solution efforts did not yield chemically rational answers, even with the aid of the elemental analysis data. The large width of the peaks, which may be due to nanocrystalline domains or disorder in the structure, can make space group determination difficult. Initial attempts at annealing the product in a tube furnace to increase crystallinity and grain size were unsuccessful as the product decomposed into tin metal, tin- and iron-oxides, as well as some $FeSn_2$. It is known that iron-borides can form through the reduction of Fe^{2+} by BH_4^- (although Fe^{3+} was used in the modified polyol process),[103] so control experiments reducing Fe^{3+} and Sn^{2+} were done separately,

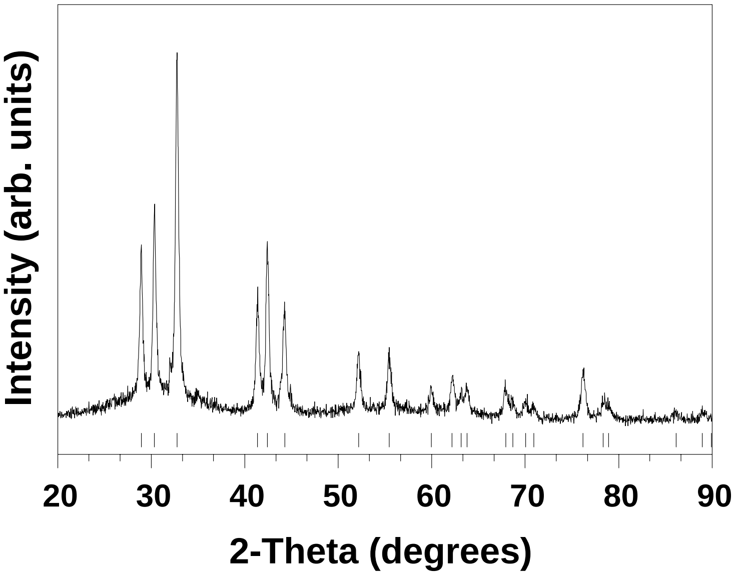

Figure 3.11 (a) Powder XRD of Fe-Sn intermediate reduced at 80 °C then heated and quenched immediately at 125 °C. Tick marks correspond to allowed reflections of $P4_2/m$ spacegroup with lattice constants $a = 3.0586$ and $c = 5.8890$ Å.

but the intermediate was not reproduced. Further attempts to increase the crystallinity of the intermediate by solution routes were unsuccessful.

3.5 Morphology of nanocrystalline intermetallics

While the low-temperature solution route has allowed us to access a variety of binary intermetallic compounds by exploiting the reaction conditions, we did not initially focus on controlling the morphology of the intermetallic products, although there is precedent for doing so in single-metal systems with this synthetic method.[2,33,35,38] We have found, however, that the as-synthesized products do exhibit interesting nanocrystalline morphologies. TEM micrographs for Co_3Sn_2, CoSn, $FeSn_2$, PtPb, and PtBi are shown in Figure 3.12. Both Co_3Sn_2 (200 °C) and CoSn (265 °C) appear to form

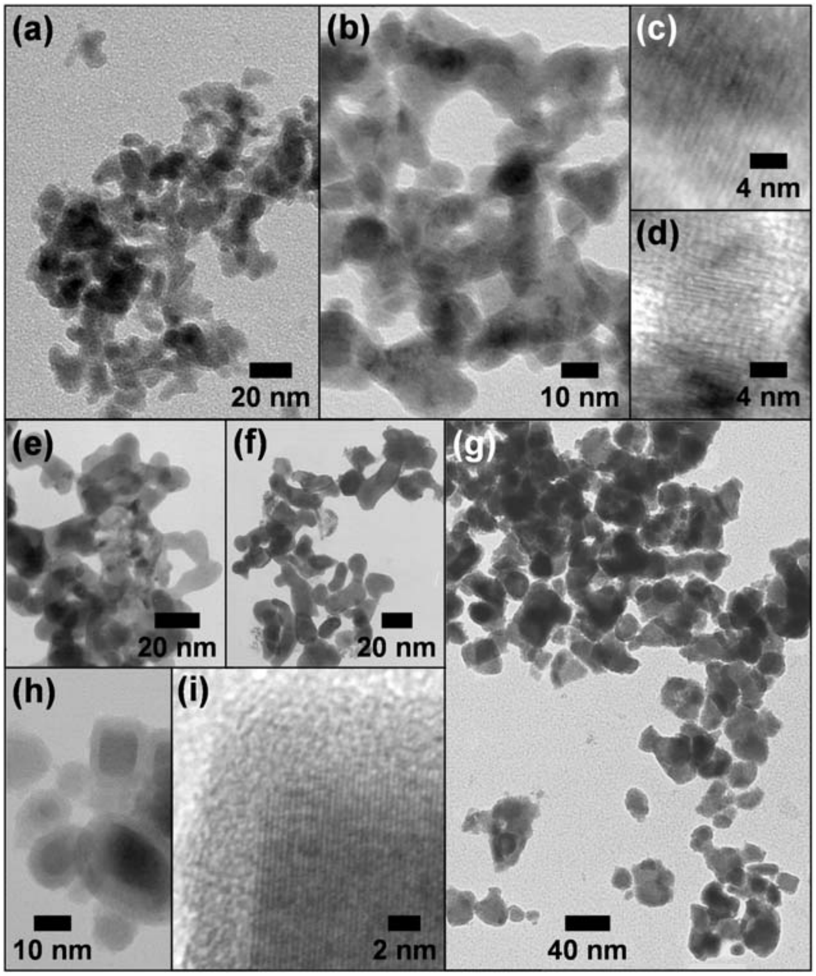

Figure 3.12 TEM micrographs for nanocrystalline (a) Co_3Sn_2, (b) CoSn, (c) Co_3Sn_2 (high resolution), (d) CoSn (high resolution), (e) PtPb, (f) PtBi, (g) $FeSn_2$ synthesized at 130 °C, and (h,i) Fe_1Sn_6 synthesized at 125 °C, showing the presence of a tin oxide shell surrounding a crystalline Fe-Sn core that shows lattice fringes.

highly irregular networks of fused particles. Lattice fringes (insets to Figures 3.12a and 3.12b) highlight the crystalline nature of the nanoparticles, but clearly show polycrystallinity with small domains. Qualitatively, particle sizes appear to range from 5 – 20 nm, while the crystalline domains appear to range in size from 3 – 15 nm. This is consistent with the broad peaks shown in the XRD data presented in Figure 3.4. PtPb powders synthesized at 165 °C consist of a mixture of spherical and irregular rod-like shapes with average particle sizes ranging from roughly 10 – 30 nm with resolvable lattice fringes. PtBi powders show much larger particles, most likely due to the higher temperature required to nucleate the intermetallic phase (240 °C).

$FeSn_2$ yields larger particles, with diameters that can exceed 50 nm. The $FeSn_2$ powders are highly irregular, much like those of the Co-Sn system. However, many of the $FeSn_2$ particles appear to have a core-shell structure. Because of the large excess of Sn required to yield the $FeSn_2$ intermetallic, our initial hypothesis was that the shell might be SnO_2. XPS was used to characterize the surface of the powder (Figure 3.13a). The Sn 3*d* peaks are clearly shifted away from standard Sn^0 values (marked by vertical lines). The higher binding energies indicate the presence of oxidized Sn. Either Sn^{2+} or Sn^{4+} could be present, since they are generally indistinguishable because of the large peak width and the small difference in binding energy between the two oxidation states.[96] Regardless, this provides good evidence that the shell is comprised of some SnO_x species. This phenomenon appears in the Co-Sn system as well, as Co_3Sn_2 annealed at 500 °C under Ar shows crystalline SnO_2 by XRD. This is consistent with the SAED pattern for Co_3Sn_2, which shows a wide, diffuse band that matches the most intense peaks for an amorphous tin oxide phase.

The DSC trace (Figure 3.13b) from a Fe-Sn reaction (1:6 initial molar ratio) quenched immediately when the temperature reached 125 °C (e.g. prior to complete crystallization of $FeSn_2$) shows several thermal events. A broad exotherm can be seen with peaks at 280 °C and 290 °C. A sample heated to 285 °C under flowing Ar revealed

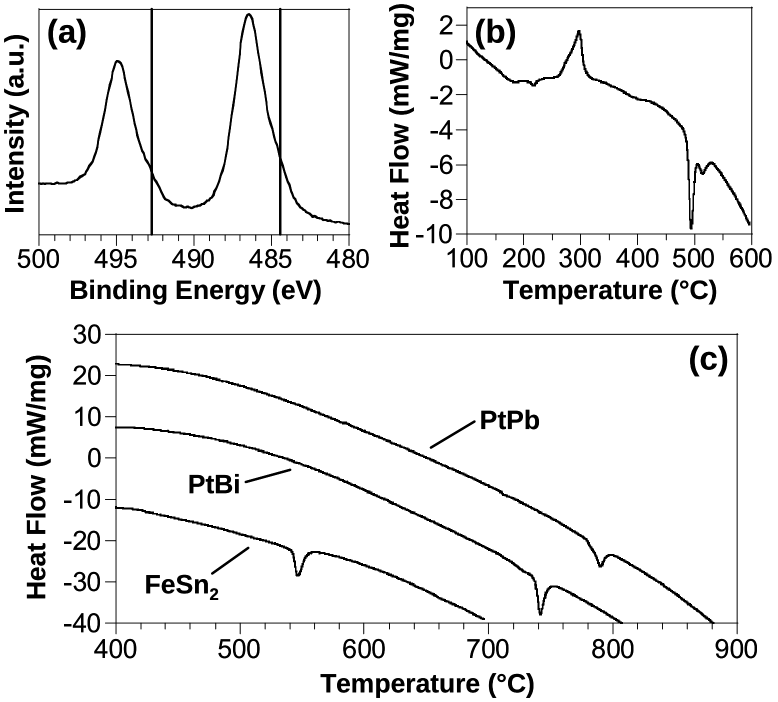

Figure 3.13 (a) XPS data for the Sn 3*d* peaks for $FeSn_2$ (vertical lines show the Sn $3d_{3/2}$ and $3d_{5/2}$ peaks for Sn^0); (b) DSC trace from a 1:6 Fe:Sn reaction quenched immediately when the temperature reached 125 °C, prior to complete crystallization of $FeSn_2$ (see text for interpretation of endotherms and exotherms; in the plot, exothermic is up); (c) DSC trace for $FeSn_2$ (phase pure, synthesized at 130 °C), PtPb, and PtBi.

a mixture of SnO and $FeSn_2$ by XRD, suggesting that the SnO_x shell is SnO rather than SnO_2. The higher-temperature endotherms most likely correspond to decomposition of $FeSn_2$ and SnO_x.[101] Additional DSC studies of intermetallic $FeSn_2$ (phase pure and crystalline, synthesized at 130 °C), PtPb, and PtBi, shown in Figure 3.13c, show disordering or decomposition endotherms at temperatures near or slightly lower than their bulk values as determined from their phase diagrams.[100]

Intermetallic powders obtained through traditional solid-state synthesis methods yield micron-sized (or larger) particles due to the sintering that is inherent at high-temperatures. Figure 3.14 shows representative SEM images of PtBi, $FeSn_2$, and CoSn powders synthesized using the polyol process. The nanocrystalline powders form spherical aggregates with diameters of 100 – 150 nm, and these aggregates tend to form densely packed monoliths. In all cases, the intermetallics made via the polyol process form dense nanocrystalline powders that are difficult to obtain using traditional methods.

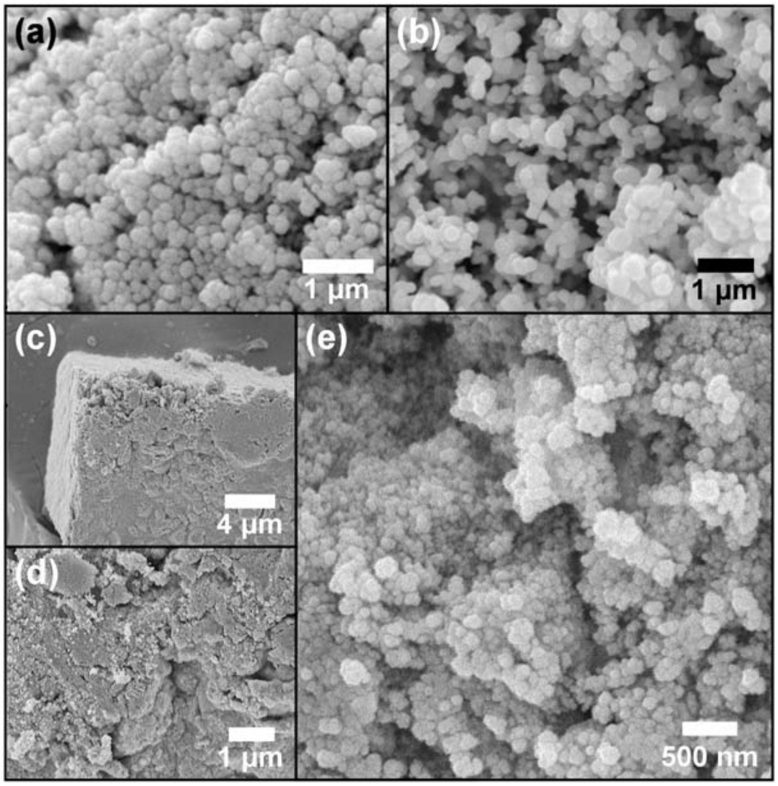

Figure 3.14 SEM micrographs of (a) PtBi, (b) $FeSn_2$, and (c,d,e) CoSn (three magnifications) nanocrystalline intermetallic powders.

3.6 Solution processing of nanocrystalline intermetallics

It is well known that metal nanocrystals and nanocrystalline powders synthesized using solution routes offer advantages over traditionally-synthesized bulk powders in terms of solution-based materials processing capabilities. For example, polyol-derived metal nanocrystals can be used to form thin films and patterned nanostructures on a variety of substrates,[46,105] and a variety of templated nanomaterials, including nanotubes,[106] inverse opals,[47,107] and hollow nanoscale capsules,[108] can be accessed using standard solution techniques. Because of the difficulty in obtaining solution-dispersible nanocrystalline intermetallic compounds, similar solution-processed intermetallic nanomaterials have remained rare. In Figure 3.15, we show that intermetallic $FeSn_2$ nanocrystals can be infiltrated into a polystyrene colloidal crystal and converted into a highly porous $FeSn_2$ inverse opal by dissolving the polymer template in toluene. Similar results can be obtained using other nanocrystalline intermetallics as precursors. Preliminary evidence also suggests that nanocrystalline intermetallic thin films are accessible using simple drop coating methods.

3.7 Summary

In this chapter, we demonstrate that the polyol process can be used to synthesize nanocrystalline powders of many late transition-metal and main-group metal intermetallic compounds. In some cases, multiple crystalline products can be accessed during the progression of a single reaction, suggesting unusually facile low-temperature solution-mediated reactivity of the nanocrystalline intermetallics. The polyol derived

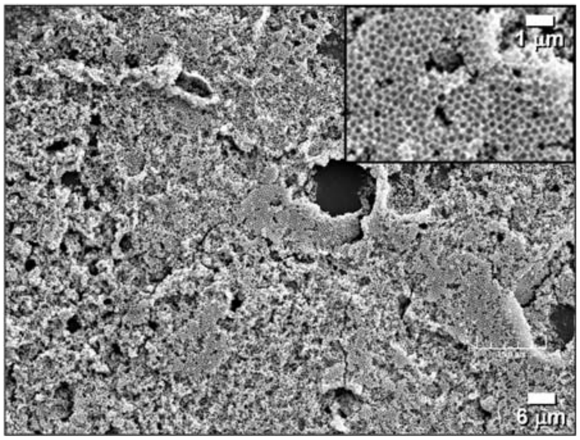

Figure 3.14 SEM micrograph of intermetallic $FeSn_2$ colloidal crystal replica synthesized by templating against a colloidal crystal of monodisperse 600 nm polystyrene spheres.

intermetallics form nanoscale crystallites that range in size from 5 to 100 nm, depending on the system and synthetic conditions, and are amenable to solution-processing capabilities, such as colloidal crystal templating. The successful synthesis of a large library of nanocrystalline intermetallics using the polyol process has several important implications. First, since the polyol process is known to yield exquisite control over nanocrystal shape and size,[34,36,39-41] it is reasonable to anticipate that future synthetic modifications will yield similar results. Such an accomplishment would provide access to a wide range of nanomaterials for advanced technological applications and would also facilitate careful size-dependent studies of many important physical phenomena. Second, intermetallic nanoparticles synthesized through this or related methods could prove useful for studies of catalysis and structure-activity relationships on high surface area intermetallic surfaces, providing that the surface chemistry can be appropriately modified and controlled. Third, many emerging applications will increasingly rely on nanocrystalline intermetallics for improved properties, e.g., ductility, hydrogen storage capacity, and thermoelectric efficiency,[109] and the synthetic route described in this work may provide a facile approach for accessing such nanomaterials. Fourth, solution-based routes are common for accessing nanocrystal-derived thin films and templated nanomaterials,[2,3,46-48] and these nanocrystalline materials could significantly expand the availability of intermetallic precursors for such applications. Finally, it is known that the polyol process can yield new and metastable structures not accessible using traditional methods.[42,44,45] The intermediate formed during the synthesis of $FeSn_2$ may be such an example, however the identity of the compound remains unknown. The work described here defines a wide range of intermetallic systems that are accessible using solution methods and opens the door to the discovery of new materials in these and related systems.

CHAPTER IV

SOLUTION SYNTHESIS OF NANOCRYSTALLINE *M"*-Zn INTERMETALLIC COMPOUNDS VIA CHEMICAL CONVERSION OF METAL NANOPARTICLE PRECURSORS*

4.1 Introduction

Alloys of zinc and the late transition metals comprise a diverse class of materials with a range of important structural, catalytic, and electronic properties. Most notably, zinc alloys are desirable materials for their mechanical hardness and corrosion resistance[61] and accordingly are widely used in industry for die casting and coatings. *M*-Zn intermetallic compounds are also important materials because of their advanced chemical and physical properties, such as catalytic production of H_2[62] and methanol,[63] magnetism,[64] shape-memory effects,[65-67] and tunable surface plasmon resonance (SPR) in colloids.[1] Intermetallic PdZn has shown promise as a catalyst for the steam reformation of methanol for the selective production of H_2 and CO_2, and PdZn is also suspected to be responsible for the high activity and selectivity of ZnO-supported Pd for the same reaction.[68] Similarly, a Cu-Zn alloy formed at the interface of ZnO-supported Cu is suspected to be an active phase for the synthesis of methanol from CO_2 and H_2.[69]

---

* Reprinted in part with permission from *Chem. Mater.*, *19* Cable, R. E.; Schaak, R. E. "Solution Synthesis of Nanocrystalline *M*-Zn (*M* = Pd, Au, Cu) Intermetallic Compounds via Chemical Conversion of Metal Nanoparticle Precursors," 4098, Copyright 2007 by the American Chemical Society.

Cu-Zn colloids have also been investigated for their optical properties, showing that the SPR band can be tuned over a 60 nm range by varying the alloy composition.[1]

Several strategies have been developed for preparing nanoscale zinc/transition metal alloys and intermetallic compounds. Top-down approaches such as ball-milling have successfully generated binary Zn intermetallics but require reaction times of 20 h or more.[68] Other approaches such as annealing a ZnO-supported transition metal in a reducing atmosphere,[67] electroplating,[70] and laser ablation of bulk *M*-Zn intermetallics[15] have yielded nanocrystalline materials, but phase-pure products are difficult to achieve, and particle size and morphology are essentially uncontrollable. Solution chemistry routes, which are widely employed for the morphology-controlled synthesis of metal and multimetal nanostructures, have also been used to access nanocrystalline *M*-Zn compounds. For example, β-CuZn has been synthesized from Cu(II) and Zn(II) salts.[71] However, a harsh and powerful reducing agent is required to reduce the zinc precursor. PdZn has been formed in a two-step reaction from the thermal decomposition of a heterobimetallic carboxylatebridged Pd-Zn species followed by reduction under H_2 in a furnace.[72] However, this requires the synthesis of a complex molecular precursor and provides little control over particle size and morphology. Polycrystalline Ni-Zn nanowires have also been synthesized using electrochemical deposition into porous anodic alumina templates.[64]

Building on recent synthetic achievements and mechanistic investigations involving nanocrystalline intermetallic compounds of the late transition metals,[42,45,77,78,80] we have been developing "conversion chemistry" approaches for synthesizing morphologically controlled intermetallic nanocrystals.[42,78] This strategy is based on the idea that preformed metal nanoparticles can serve as reactive precursors that can transform into derivative phases using low-temperature chemical reactions. Key examples include the formation of Ag_2Se by reaction of Se with solutions of $AgNO_3$,[110] the synthesis of metal phosphides by reacting metal nanoparticles with trioctylphosphine,[78,79] and the shape-controlled formation of M-Sn intermetallics (M = Fe, Co, Ni, Pd) by reaction of β-Sn nanocrystals with appropriate metal precursors under reducing conditions.[42] These processes generally involve a diffusion based mechanism, where a zero-valent metal precursor diffuses into the pre-existing metal nanoparticle. In many cases, the shape of the metal nanoparticle precursors can be retained in the final product, providing a potentially generalizable strategy for controlling the morphology of nanocrystals with two or more elements in a compositionally controllable manner. This approach, therefore, capitalizes on advances in the synthesis of single-metal nanoparticles and utilizes them as compositional, morphological, and sometimes structural precursors for the formation of more complex nanocrystals than are often achievable using direct methods. In particular, this approach may be a solution to the problem of incorporating electropositive metals or metals whose precursors are not easy to reduce into nanocrystals with the ability to simultaneously control their morphology. A generalized robust strategy for incorporating such metals into alloy and intermetallic nanocrystals may impact several areas of modern materials research that rely on these elements for their properties, including catalysis, structural materials, superconductivity, hydrogen storage, and magnetic materials.

In this chapter, we describe the application of this “conversion chemistry” approach to the formation of Zn-based intermetallic nanocrystals using chemistry that facilitates compositional, structural, and morphological control. We build on chemistry which reports Cu-Zn alloy and intermetallic nanocrystals of various compositions prepared via thermolysis of a specially prepared Cu(II) reagent with Et_2Zn.[1] Specifically, Zn-based intermetallics are synthesized in a one-pot reaction by adding diethyl zinc (Et_2Zn) or diphenyl zinc (Ph_2Zn) to preformed metal nanocrystals generated in situ. We also show that the chemistry that is developed for one system is portable to several others, providing evidence of generality. Finally, all of the reagents and precursors are commercially available, which is convenient but also important for generalizing the method to other systems in the future. The targets we chose cover a range of useful Zn-based intermetallic nanomaterials. Au-Zn intermetallics can have advanced structural properties, and we have prepared two different phases within this system, β'-AuZn and Au_3Zn[R1]. β'-AuZn is a known shape-memory material,[65,66] and there is evidence that Au_3Zn[R1] may also undergo reversible martensite transformation.[67] Cu-Zn alloys and intermetallics also have useful structural and corrosion resistant properties.[61] More recently, ZnO-supported Pd catalysts were found to be highly active for the selective production of H_2 and CO_2 via steam reformation of methanol,[62] while ZnO-supported Cu catalysts are active for the production of methanol from CO_2 and H_2.[63] In each case, a Cu- or Pd-Zn intermetallic or alloy is suspected to be responsible for the high activity and selectivity. Here we report the synthesis of nanocrystalline β_1-PdZn, γ-CuZn (Cu_5Zn_8), β'-AuZn, and Au_3Zn[R1] using a unified chemical conversion strategy that utilizes preformed Pd, Cu, and Au nanocrystals as precursors.

4.2 Experimental details

4.2.1 *Materials*

All chemicals were used as received and stored in a glovebox under Ar. The following solvents were used: $CH_3(CH_2)_{15}$-NH_2 (1-hexadecylamine, tech 90%, remainder mainly 1-octadecylamine), $CH_3(CH_2)_{17}NH_2$ (1-octadecylamine, 98%), and $CH_3(CH_2)_7$-NH_2 (1-octylamine, 99%). The following metal reagents were used: $AuCl_3$ (99.99%), $Au(OOCCH_3)_2$ (99.9%), $Cu(OOCCH_3)_2$ (anhydrous, 98%), $Pd_2(C_{17}H_{14}O)_3$ (Pd content 23.34%), $Zn(C_2H_5)_2$ (diethylzinc, nominally 15% w/w in hexane), and $(C_6H_5)_2Zn$ (diphenylzinc, 98+%). All chemicals were purchased from Alfa Aesar.

4.2.2 *Synthesis*

The synthetic method relies upon the thermal decomposition or reduction of zero-valent organometallic or metalsalt reagents in a hot organoamine solvent. In short, HDA or a mixture of HDA and ODA were heated in a 100 mL three-neck round-bottom flask under flowing Ar and magnetic stirring. The flask was outfitted with a condenser and thermometer adaptor with a gas inlet. A 1-octylamine solution of the transition metal precursor was injected into the hot organoamine solvent and allowed to age for various amounts of time before a small aliquot was removed in order to probe the reaction pathway. A 1-octylamine solution of Et_2Zn or diphenylzinc (Ph_2Zn) was then added to the reaction, and the temperature was increased if necessary and held at roughly 250 °C for 1 h. After the hour, the reaction was cooled to roughly 30 °C. All aliquots and final products were isolated by centrifugation after the addition of a 3:1 solution of toluene:ethanol and then washed several times with a 1:4 toluene:ethanol solution. After centrifugation, the supernatant solutions generally were completely colorless. This indicates nearly complete reaction of the Au, Cu, and Pd precursors, which were the limiting reagents.

PdZn. $Pd_2(C_{17}H_{14}O)_3$ (2 mL, 12.3 mM in 1-octylamine) was added to 5.1 g of HDA at 250 °C. After 25 min a small aliquot was taken followed by the quick addition of 1 mL of Et_2Zn (0.465 M in 1-octylamine). The solution was held at 250 °C for 1 h.

Cu_5Zn_8. $Cu(OOCCH_3)_2$ (2 mL, 25.1 mM in 1-octylamine) was quickly added to 5.1 g of HDA at 140 °C. After heating to 220 °C, the solution turns from light blue to yellow and then a rusty red/blue, indicating the formation of Cu^0 particles. After taking a small aliquot, 1 mL of Et_2Zn (0.412 M in 1-octylamine) was quickly added and the reaction was heated to 245-250 °C and held for 1 h.

AuZn. $Au(OOCCH_3)_2$ (2 mL, 24.7 mM in 1-octylamine) was quickly added to 5.4 g of HDA at 250 °C. The solution quickly turned pink then deep wine-red, indicating the formation of Au0 particles. After 10 min, the solution was cooled to 230 °C and 1 mL of Et_2Zn (0.619 M in 1-octylamine) was quickly added. The solution was heated back to 250 °C and held for 1 h and turned a dark black/purple color.

Au_3Zn. $AuCl_3$ (2 mL, 26.5 mM in 1-octylamine) was quickly added to 3.8 g of HDA and 1.0 g of ODA at 120 °C. The solution was slowly heated to 140 °C, and the

color changed from yellow to pink then deep wine-red, indicating the formation of Au^0 particles. After taking an aliquot, 1 mL of Ph_2Zn (0.206 M in 1-octylamine) was quickly added. The solution was heated to 225-230 °C and held for 1 h and turned a dark red/brown color.

4.2.3 *Characterization*

Powder X-ray diffraction (XRD) data were collected on a Bruker GADDS three-circle X-ray diffractometer using Cu Kα radiation. Transmission electron microscopy (TEM) images, selected area electron diffraction (SAED) patterns, and energy-dispersive X-ray analysis (EDS) were collected using a JEOL JEM-2010 TEM. Samples were prepared by sonicating the nanocrystalline metal or intermetallic powders in ethanol or toluene and dropping a small volume onto a carbon-coated copper or nickel grid. Optical spectroscopy was collected by an Agilent 8453 UV-visible spectrophotometer using quartz cuvettes.

4.3 Synthesis of nanocrystalline *M”*-Zn intermetallics

Long-chain organoamine solvents and zero-valent organometallic reagents have become widely used in the synthesis of metal nanoparticles and have been useful for controlling particle morphology in some systems.[2,111-114] However, rigorously controlling morphology in multimetal systems, while not unprecedented, is more challenging than in single-metal systems. When relying on the coreduction and/or decomposition of multiple metal reagents, it can be very difficult to find reaction conditions suitable for controlling the morphology of the final product. By utilizing a two-step process, we find that the morphology of the intermetallic *M"*-Zn product may be templated by the morphology of the single-metal nanoparticle precursors, which is much easier to control. Accordingly, our "conversion chemistry" route to *M"*-Zn intermetallics involves two distinct steps: the formation of transition metal nanocrystals by the thermolysis or reduction of commercially available reagents and their subsequent transformation into *M"*-Zn intermetallics upon reaction with organozinc reagents (e.g., Et_2Zn) in a hot organoamine solvent. Hot hexadecylamine (HDA) can liberate Zn(0) from Et_2Zn,[1] which can then diffuse into the nanocrystalline metal precursors, eliminating the need for strong reducing agents. (Et_2Zn is highly reactive and ZnO impurities are sometimes seen by us and others[1] even when using rigorously air-free conditions. However, these can be minimized or eliminated by employing careful synthetic techniques and possibly postsynthesis workup.) The organoamine solvent likely doubles as a surface stabilizing agent, which is consistent with the high particle solubility observed in nonpolar solvents like toluene and aggregation and precipitation in polar solvents such as ethanol.

The Pd-Zn system provides a representative example of the two-step synthetic pathway used to generate nanocrystalline *M"*-Zn intermetallics. Pd nanoparticles were first synthesized by injecting a 1-octylamine solution of tris-(dibenzylideneacetone)dipalladium(0) into HDA at 250 °C. After aging the dispersion for 30 min, a solution of Et_2Zn in 1-octylamine was quickly injected. The powder XRD patterns (Figure 4.1) for the Pd precursor and PdZn product, consistent with the

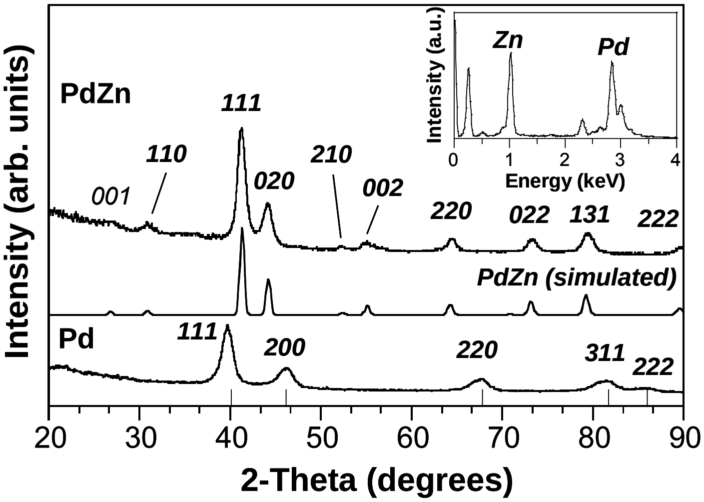

Figure 4.1 Powder XRD patterns of nanocrystalline Pd precursor and intermetallic PdZn formed after reaction with Et_2Zn. Tick marks correspond to the allowed reflections for Pd, and the simulated XRD pattern for PdZn confirms that the final product is AuCu-type PdZn. EDS (inset) confirms that both Pd and Zn are present in the final product in the expected 1:1 ratio.

simulated patterns for each phase, confirm that Pd nanocrystals were formed first and then converted to PdZn. A TEM micrograph of the Pd nanoparticles isolated from the reaction immediately before the addition of Et_2Zn is shown in Figure 4.2a, along with the accompanying selected area electron diffraction (SAED) pattern. The data confirm that the reaction pathway begins with the formation of Pd particles, which are then converted to PdZn. The Pd precursor is an interconnected network of nanocrystalline Pd particles with characteristic sizes that range from roughly 5 to 20 nm. The final PdZn product, formed from the reaction of the Pd precursor with Et_2Zn, retains the morphology defined by the precursor (Figure 4.2b). The interconnected network of PdZn particles grew to an upper-limit diameter of 30 nm. Such particle growth is expected and in fact is required by the addition of Zn to the Pd particles via a diffusion-

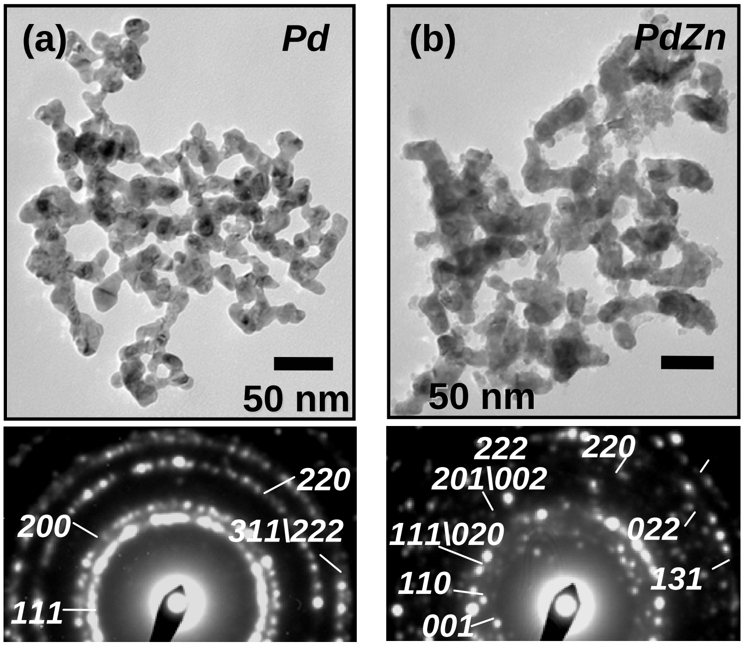

Figure 4.2 TEM micrographs and corresponding SAED patterns for (a) the nanocrystalline Pd precursor and (b) the intermetallic PdZn product after conversion. SAED patterns match those expected for Pd and PdZn (compare indexing with XRD data in Fig. 4.1).

based mechanism. Data from XRD, TEM, SAED (Figures 4.1 and 4.2), and EDS (Figure 4.1) collectively confirm the morphology-conserving chemical transformation of nanocrystalline Pd (fcc structure) into nanocrystalline β_1-PdZn (AuCu structure).

Intermetallic Cu-Zn nanocrystals can also be generated using similar chemistry. In this case, a solution of copper-(II) acetate was injected into hot HDA (140 °C) and the temperature was slowly raised to 220 °C. At this temperature, the solution starts to turn a rusty-red color, indicating the reduction of Cu^{2+} to Cu^{0} colloids. At high temperatures, organoamines are known to reduce metal salts, their reducing power resulting from the

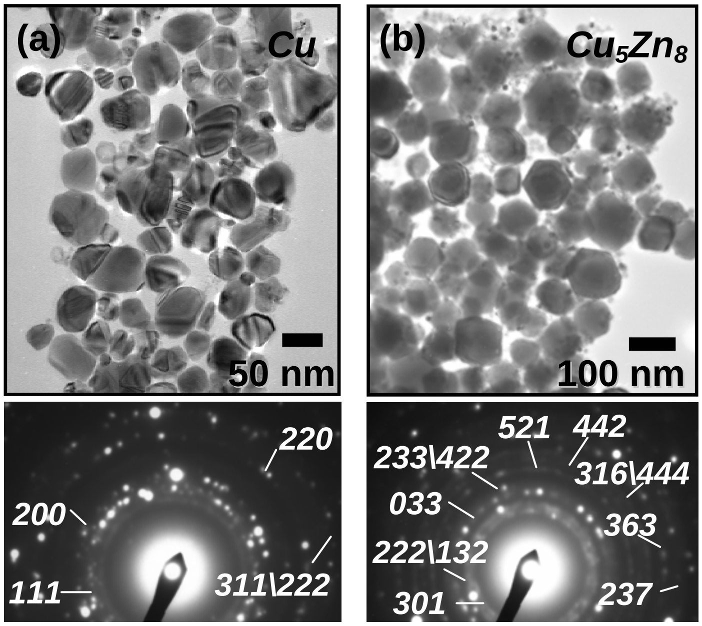

Figure 4.3 TEM micrographs and corresponding SAED patterns for (a) the nanocrystalline Cu precursor and (b) the intermetallic Cu_5Zn_8 product after conversion. SAED patterns match those expected for Cu and Cu_5Zn_8 (compare indexing with XRD data in Fig 4.4).

oxidation of the amine groups to nitriles.[114,115] TEM analysis of an aliquot taken from this solution reveals irregularly shaped, multifaceted nanocrystals ranging in size from roughly 20 to 60 nm (Figure 4.3a), and XRD and SAED confirm that these are Cu nanocrystals as expected. This morphology is similar to a previous report of Cu nanocrystals that were made in hot TOPO,[113] as well as a report of Cu nanocrystals being made in reverse micelles upon reduction by hydrazine.[116] Et_2Zn was added several minutes after the color change, and the solution was heated to 250 °C and held at that temperature for 1 h. The product is γ-Cu_5Zn_8 based on powder XRD (Figure 4.4) and SAED (Figure 4.3b), and EDS data confirm the correct composition (Figure 4.4).

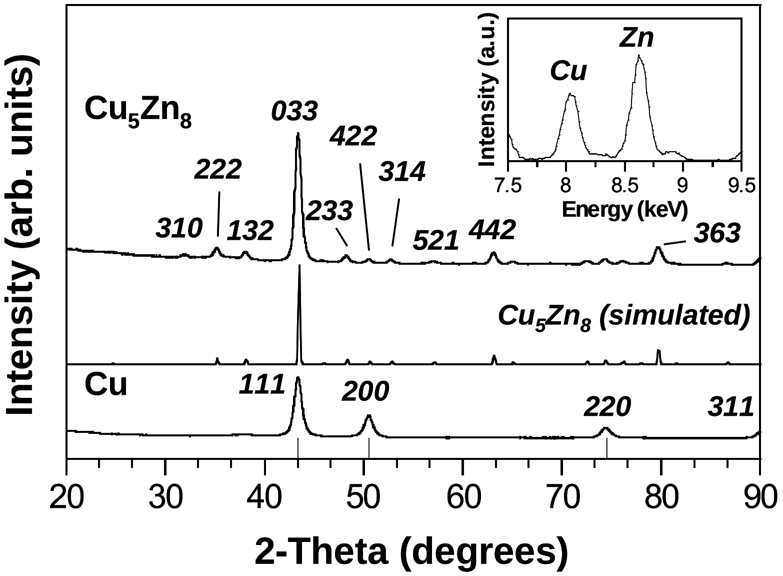

Figure 4.4 Powder XRD patterns of nanocrystalline Cu precursor and intermetallic Cu_5Zn_8 formed after reaction with Et_2Zn. Tick marks correspond to the allowed reflections for Cu, and the simulated XRD pattern confirms that the final product is Cu_5Zn_8. EDS (inset) confirms that Cu and Zn are present in the final product in a 37:63 ratio, which is close to that expected for Cu_5Zn_8.

TEM micrographs show that the Cu_5Zn_8 final product often consists of a bidisperse distribution of 10-15 and 70-100 nm particles that are quasispherical and multifaceted. A shell of lighter contrast, which is most likely ZnO, can be seen in all of the products but most easily in the smaller particles (Figure 4.5). The smaller particles are possibly the result of the low-temperature preparation of the Cu precursor particles discussed above. Because Et_2Zn is added to the reaction mixture a few minutes after the first signs of Cu reduction, the reduction may not be complete under these conditions. When the temperature is increased to 250 °C and existing particle growth is occurring, some of the remaining Cu(II) may be reduced to form very small Cu particles that react

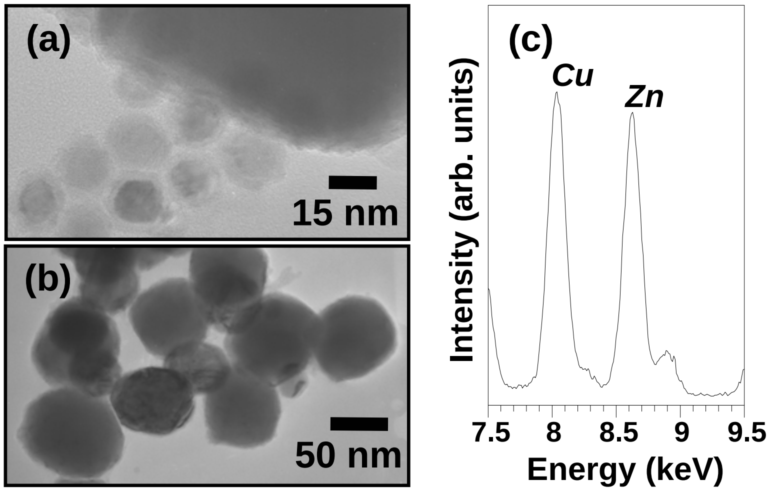

Figure 4.5 TEM micrographs showing (a) core/shell nanostructure in small and large particles of Cu_5Zn_8 product formed by converting Cu nanocrystals formed at lower temperatures (the shell is likely ZnO), and (b) Cu_5Zn_8 product converted from Cu nanocrystals formed at higher temperature, which minimizes small particles. EDS data for the Cu_5Zn_8 product in (b) shows the presence of both Cu and Zn.

to form Cu_5Zn_8. (There is no XRD, SAED, or EDS evidence for Cu or Zn metal in the final product.) Consistent with this hypothesis, the population of small particles can be minimized by modifying the reaction conditions. For example, injecting the copper(II) acetate at 250 °C followed by the addition of Et_2Zn after 20 min results in quasispherical Cu_5Zn_8 particles that range in size from 50 to 100 nm, as seen in Figure 4.5 along with the accompanying XRD and SAED patterns (Figure 4.6). The higher temperature addition of copper(II) acetate likely facilitates a more complete reduction of Cu(II), resulting in a more uniform Cu precursor particle population. This hypothesis is consistent with TEM images of the final product (Figure 4.5), as well as literature reports for solution routes to Cu and Cu-Zn nanocrystals.[1,76] No attempt was made to rigorously control the morphology or size dispersity of the Cu nanoparticle precursors

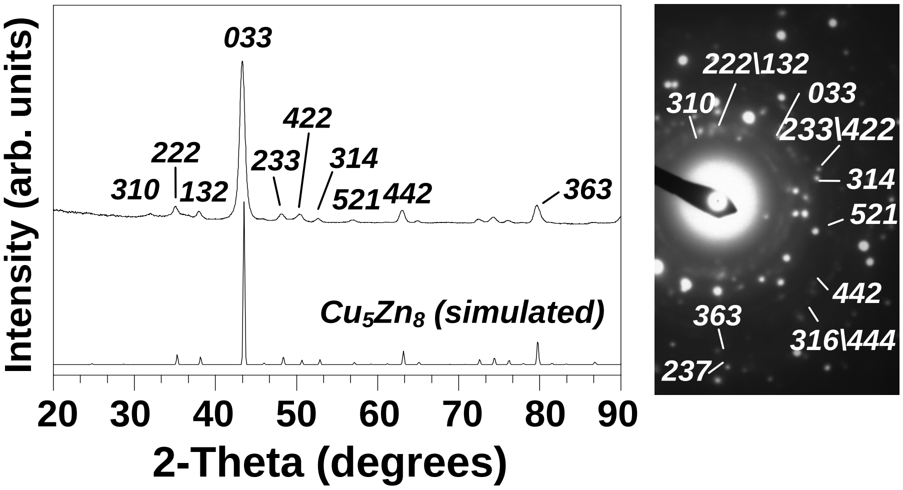

Figure 4.6 Powder XRD (top: experimental, bottom: simulated) and SAED of Cu_5Zn_8 product converted from Cu nanocrystals formed at high temperature (Fig. 4.5b,c). The product XRD and SAED patterns are consistent with the simulated Cu_5Zn_8 XRD pattern, and no ZnO is observed.

because Cu_5Zn_8 nanocrystals have been reported previously using other methods.[1,71,76] Rather, our focus was on establishing that the Cu_5Zn_8 phase can be synthesized using the same chemical conversion strategy that works for several other systems. However, literature methods exist for rigorously controlling the synthesis of Cu nanocrystals,[113,116,117] so it may be possible to access Cu_5Zn_8 nanocrystals with different sizes, size dispersities, and shapes using such nanocrystals as morphological templates.

For the Au-Zn system, care was taken to generate high quality Au nanocrystals as precursors in order to study the ability of this strategy to rigorously retain the morphology and size dispersity of the metal nanoparticle precursor in the *M*-Zn product. We find that two phases in the Au-Zn system are accessible using this general synthetic method. CsCl-type β'-AuZn can be synthesized by the reaction of Au nanoparticles

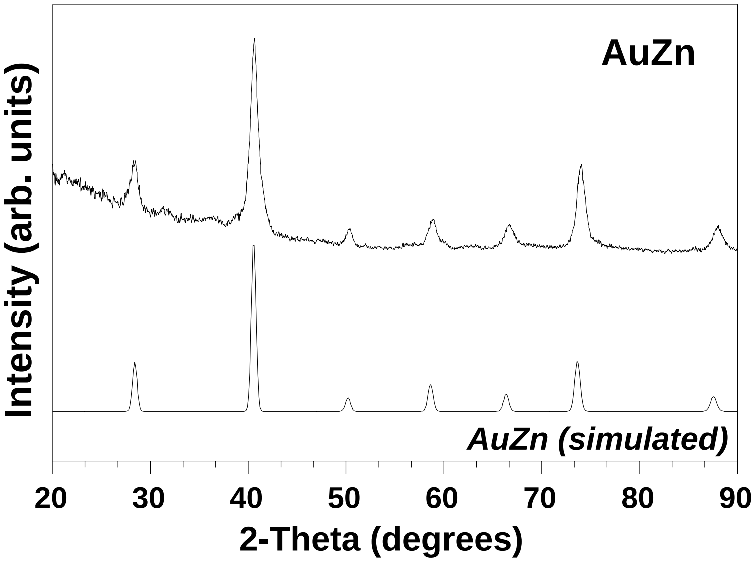

Figure 4.7 Powder XRD pattern of nanocrystalline intermetallic AuZn. A number of small peaks between 30° and 40° 2θ are due to a slight ZnO impurity in the product.

formed from gold(III) acetate with Et_2Zn in HDA at 250 °C (Figure 4.7). However, obtaining a phase pure product was very difficult. In contrast, the long-period ordered phase Au_3Zn[R1] can be routinely synthesized by using gold(III) chloride as the Au source. We found that that the final product phase depends on the reagent that is used in the synthesis. For example, Au_3Zn is the preferred phase when using $AuCl_3$ as the gold source, while AuZn is preferred when using Au(III) acetate.

A solution of $AuCl_3$ in 1-octylamine was injected into a mixture of HDA and 1-octadecylamine (ODA) at 130 °C. The solution slowly turns pink, then deep wine-red, which indicates the formation of Au nanoparticles. Powder XRD (Figure 4.8) and SAED (Figure 4.9a) confirm the formation of Au nanoparticles, and the TEM micrograph in Figure 4.9a shows that monodisperse 10 ± 1 nm Au particles formed from

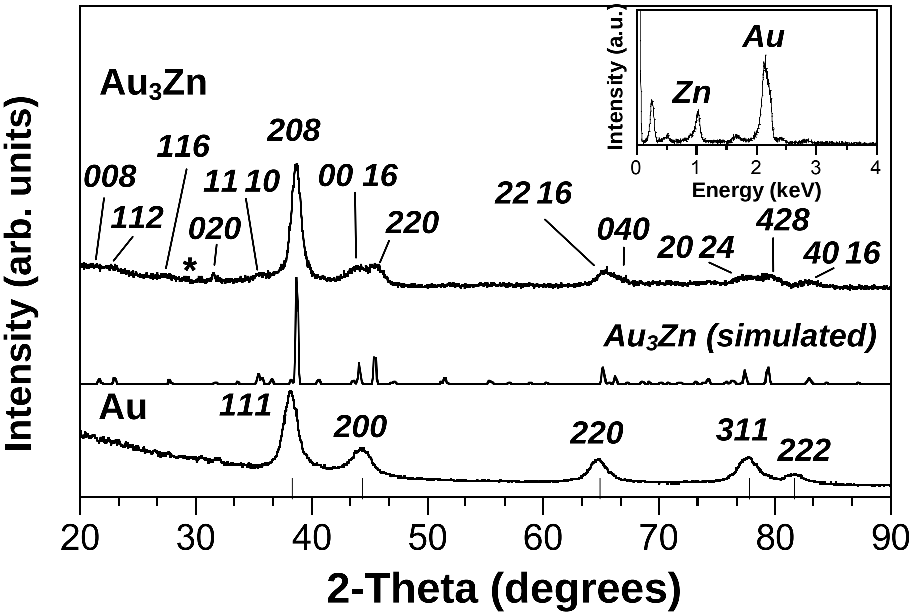

Figure 4.8 Powder XRD patterns of nanocrystalline Au precursor and intermetallic Au_3Zn formed after reaction with Ph_2Zn. Tick marks correspond to the allowed Au reflections, and the simulated XRD pattern for Au_3Zn confirms that the final product is Au_3Zn[R1]. EDS (inset) confirms that Au and Zn are present in the final Au_3Zn product in a 70:30 ratio, which is within the range of stability for the phase. A small ZnO impurity is labeled with an asterisk (*).

this reaction. Within a few minutes after the color change, a 1-octylamine solution of diphenyl zinc (Ph_2Zn) was quickly injected, and the reaction was aged at 240 °C for 1 h. Ph_2Zn was chosen as the zinc source for this reaction because it is a powder and more resistant to oxidation than Et_2Zn, and it allowed us to routinely produce phase-pure Au_3-Zn without any observable impurities.

Powder XRD confirms the formation of Au_3Zn[R1] from the reaction of Au nanoparticles with Ph_2Zn. The final Au_3-Zn particles retain the overall monodispersity and spherical morphology of the Au nanoparticle precursors, with the average size

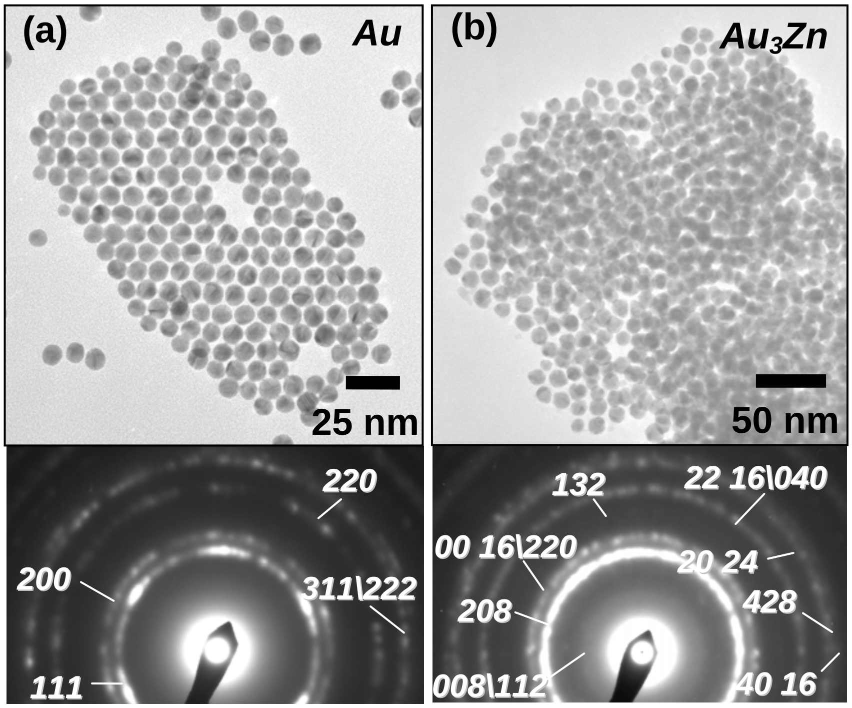

Figure 4.9 TEM micrographs and corresponding SAED patterns for (a) the Au nanocrystal precursor and (b) the intermetallic Au_3Zn product after reaction with Ph_2Zn. SAED patterns match those expected for Au and Au_3Zn (compare indexing with XRD data in Fig. 4.6).

increasing to approximately 11 ± 1.5 nm (Figure 4.9b). The particles become slightly faceted after the conversion, and this result was observed in the Cu-Zn system as well.[1] The SAED pattern for the Au_3Zn product was indexed (Figure 4.9b) and is consistent with the simulated Au_3Zn[R1] XRD pattern. EDS analysis shows that the composition is consistent with Au_3Zn as well (Figure 4.8).

4.4 Optical properties and shape anisotropy in Au_3Zn nanocrystals

Colloidal suspensions of the Au intermediate and Au_3Zn intermetallic product in toluene were analyzed by UV-visible spectroscopy (Figure 4.10). Au nanoparticles are well known to have a visible wavelength SPR band and it is highly likely that alloying with Zn will tune its position, in analogy to Cu-Zn systems that were reported previously.[1,71,76] The Au nanoparticle precursors absorb strongly with λ_{max} at 534 nm, which correlates well with the expected SPR peak position of similar Au nanoparticles in toluene.[114,118] The intermetallic Au_3Zn nanocrystals exhibit a significant blue-shift, withλ_{max} decreasing to 490 nm. This blue shift also occurs for Cu-Zn alloys and intermetallics with respect to pure copper.[1,71,76]

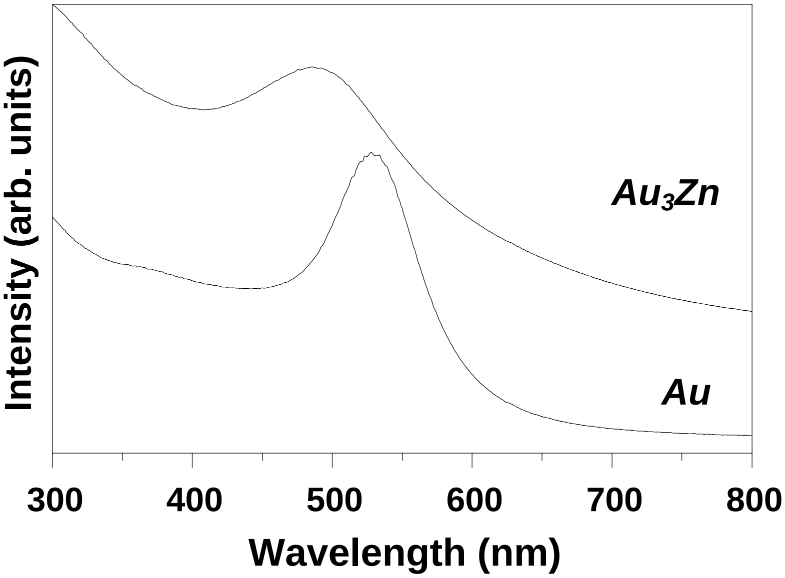

Figure 4.10 UV-visible absorption spectrum of (bottom) the Au precursor nanocrystals and (top) the Au_3Zn product nanocrystals after conversion. Both precursor and product were suspended in toluene.

Unlike many of the binary intermetallics we have focused on in the past, the *M*-Zn phases presented here are not line phases and as such are stable over a range of compositions. When working with Au_3Zn[R1], an interesting morphological change is seen when a higher concentration of the Zn reagent is used during synthesis. Starting from spherical Au particles, as seen in Figure 4.9a, the conversion to Au_3Zn using a higher Zn:Au ratio than used previously seems to induce an anisotropic particle growth, as the final product shows a significant population of particles with a “bicycle seat” morphology (Figure 4.11). While this tendency toward anisotropic morphology is slightly discernible in the Au_3Zn formed with less Zn reagent, preliminary evidence suggests that a larger concentration of Zn reagent results in more anisotropic particles and a higher degree of anisotropy. However, this typically also results in a larger amount of ZnO impurities in the sample.

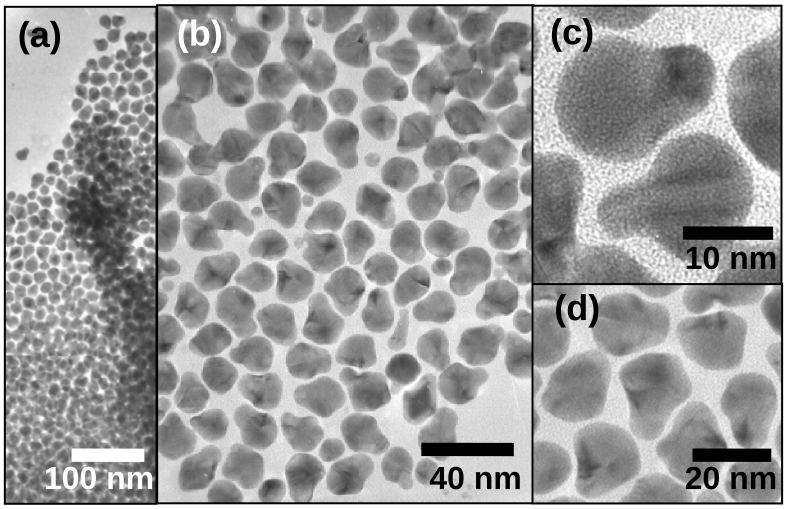

Figure 4.11 TEM images of anisotropic Au_3Zn nanoparticles with “bicycle seat” morphology formed using higher concentrations of Ph_2Zn (see the text for details).

4.5 Summary

We have demonstrated a general strategy for the solution-mediated synthesis of nanocrystalline zinc-based intermetallic compounds. Our approach, the result of ongoing investigations of reaction pathways in the synthesis of multimetal nanocrystals,[42,45,77,78,80] involves the low-temperature chemical conversion of preformed metal nanocrystals into intermetallics via reaction with zero-valent organozinc reagents such as Et_2Zn and Ph_2Zn. This strategy appears general, yielding morphologically controllable nanocrystalline intermetallics in the *M”*-Zn (*M”* = Au, Cu, Pd) systems using commercially available reagents. This work complements some nice chemistry reported by other groups[1,69,72] or the synthesis of nanocrystalline Zn-containing alloys and intermetallics, providing an alternative strategy that is both general and robust. While chemically related to some other strategies for generating *M*-Zn nanocrystals,[1,71,76] our studies rigorously identify and characterize the crucial role of metal nanoparticles as precursors that have a significant influence on the morphologies of the resulting *M”*-Zn nanocrystals and exploit this to generate a range of morphologies in several systems using standard reagents.

Zinc-based intermetallics are an important addition to the growing library of bimetallic compounds accessible as nanocrystals using straightforward solution routes. The *M”*-Zn intermetallics reported here, as well as other related compounds, have a range of useful structural, catalytic, and electronic properties, and the ability to access them as nanocrystals using a robust and unified strategy has the potential to expand their applications in these areas. For example, nanocrystalline shape memory alloys such as

AuZn could serve as precursors for elaborate nanostructured and microstructured actuators[117] formed via solution-mediated or infiltration-based templating (regardless of their morphology or regularity) followed by low-temperature annealing. Also, nanocrystalline materials can exhibit superplastic behavior,[120] and being able to incorporate additional physical properties such as magnetism or corrosion resistance into such materials may open doors to more advanced applications. The development of facile routes for synthesizing these compounds as nanocrystals is vital to advancing their incorporation into new materials, devices, and processes.

This chemical conversion pathway that results in the formation of *M”*-Zn intermetallic nanocrystals also is important for the realization of additional advances in the synthesis of complex nanocrystalline solids. First, this process represents a quick and easy route to morphologically controllable intermetallics comprised of metals that are difficult to reduce as salts without the use of strong reducing agents. Applying this strategy to additional systems could allow for the incorporation of many other hard-to-reduce metals into intermetallics that are otherwise difficult to synthesize as nanoscale solids using solution chemistry routes. Such capabilities would expand the range of accessible materials for applications in catalysis, superconductivity, magnetism, hydrogen storage, etc. Second, this method has the potential to accommodate rigorous control over particle size and morphology for intermetallic nanoparticles. There are several reports of single-metal nanocrystal systems for which size and shape control is achievable using organoamine solvents like those used here.[112-114] Our results demonstrate that these metal nanoparticles can be used as precursors to *M”*-Zn intermetallics with compelling evidence that morphology is preserved upon conversion to the intermetallic product. This capability is highly relevant for the development of new technologies involving catalysts, shape memory materials, and optically active nanomaterials, as well as fundamental scientific investigations of size-shape-property interrelationships in well-controlled nanomaterials.

CHAPTER V

REACTING THE UNREACTIVE: A TOOLBOX OF LOW-TEMPERATURE SOLUTION-MEDIATED REACTIONS FOR THE FACILE INTERCONVERSION OF NANOCRYSTALLINE INTERMETALLIC COMPOUNDS*

5.1 Introduction

Most inorganic solids are unreactive at low temperatures, requiring high temperatures to disrupt their long-range bonding networks and to overcome the solid-solid diffusion barrier that is necessary to mix the reactants. Bulk metallurgical solids, including alloys and intermetallic compounds, are especially inert. Indeed, many are known for their resistance to oxidation and corrosion, even at high temperatures.[113] However, the surfaces of metallurgical compounds may be quite reactive, often forming thin layers of passivating phases.[122] This implies that if the surface area of metallurgical compounds is greatly increased by forming nanocrystals, their reactivity may also be greatly increased, lending themselves to chemical transformation. To date, a few metals and semiconductors have been shown to exhibit enhanced reactivity as nanocrystals. For example, Co nanocrystals can be reacted to form Co oxides, sulfides, and selenides,[123] and CdSe quantum dots undergo reversible ion exchange with Ag^+ to form Ag_2Se.[124]

---

* Reprinted in part with permission from *J. Am. Chem. Soc., 128* Cable, R. E.; Schaak, R. E. "Reacting the Unreactive: A Toolbox of Low-Temperature Solution-Mediated Reactions for the Facile Interconversion of Nanocrystalline Intermetallics Compounds" 9588, Copyright 2006 by the American Chemical Society.

Previously we have shown that single-metal nanocrystals can serve as reactive precursors for the formation of more complex intermetallic and metal phosphide materials.[42,45,77,78,80] Reacting single metal nanocrystals (M = Au, Cu, Pd) with Et_2Zn in a hot coordinating solvent, we have successfully formed M-Zn intermetallic nanocrystals through a solid-solid diffusion mechanism.[77] Likewise, shape-controlled synthesis of M-Sn intermetallics (M = Fe, Co, Ni, Pd) has been achieved through the reaction of β-Sn nanocrystals with appropriate metal salt precursors and added reducing agents,[42] and metal phosphides can be formed by reacting single-metal nanoparticles with trioctylphosphine.[78] However, analogous studies with alloys and intermetallic precursors, which can be structurally and compositionally more complex, have not been reported. The ability to modify the composition and structure of metallurgical solids rationally and predictably would be important, as these parameters are fundamentally tied to their physical and chemical properties.

Here we extend our conversion chemistry approach to more structurally complex nanocrystal precursors. We show that nanocrystals of intermetallic compounds can undergo facile solution-mediated reactions to form derivative phases. Furthermore, these reactions are reversible, allowing stepwise and cyclic interconversion using a simple chemical process. We previously synthesized a library of nanocrystalline intermetallic compounds,[35,48] and here we show that these intermetallics can also be used as reagents for the low-temperature solution synthesis of other intermetallic phases, including some that are difficult to make using direct one-pot reactions.

5.2 Experimental details

5.2.1 *Materials*

The following metal reagents were used: $Cu(C_2H_3O_2)_2{\cdot}H_2O$ (98.0-102.0%), $HAuCl_4{\cdot}3H_2O$ (99.99%), K_2PtCl_6 (40.11% Pt), $Ni(acac)_2$, and $SnCl_2$ (anhydrous, 99% min.). The reducing agent (for the synthesis of the initial reagent), surface stabilizer, and solvent were $NaBH_4$ (98%), poly(vinyl pyrrolidone) (PVP, MW = 40 000 or MW = 630 000), and tetraethylene glycol (TEG, 99+%), respectively. All chemicals were purchased from Alfa Aesar and used as received.

5.2.2 *Intermetallic reagent synthesis*

The nanocrystalline intermetallic powders were synthesized by a modified polyol process, which has been previously reported.[34,46] An example synthesis of PtSn involved the sequential dissolving of 1.0500 g PVP (MW = 40 000) and 0.125 g K_2PtCl_6 in 150.0 mL of TEG by sonication and magnetic stirring. $SnCl_2$ (0.1052 g) was then dissolved by the same means. After the solution was vigorously stirred at room temperature under bubbling Ar for at least 1 hour, 45 mg of $NaBH_4$ freshly dissolved in 5 mL TEG was added slowly. Upon reduction, the solution turned a dark brown/black color, and was then heated to 245 °C and turns dark black. The solution is then removed from heat and allowed to cool under bubbling Ar.

Ni_3Sn_2 was synthesized by dissolving 35.0 mg $Ni(acac)_2$ in 30 mL TEG by sonication and magnetic stirring, followed by 95.3 mg $SnCl_2$ and 170 mg PVP (MW = 40 000). The solution was vigorously stirred at room temperature under bubbling Ar for

1.5 h, then then reduced by the slow addition of 1 mL of a freshly prepared 0.846 M solution of $NaBH_4$ in TEG. The reduced solution was heated to 215 °C, removed from heat and allowed to cool under bubbling Ar.

AuCu was synthesized similarly by dissolving 6.9 mg $Cu(C_2H_3O_2)_2{\cdot}H_2O$ in 40 mL of TEG by sonication and magnetic stirring, followed by 13.5 mg $HAuCl_4{\cdot}3H_2O$ and 103 mg PVP (MW = 630 000). The solution was vigorously stirred at room temperature under bubbling Ar for 30 min, then reduced by the slow addition of 20 mL of a freshly prepared 12.5 mM solution of $NaBH_4$ in TEG. The reduced solution was heated to 315 °C, removed from heat and allowed to cool under bubbling Ar. Powders were precipitated from solution by centrifugation and were washed thoroughly with ethanol.

5.2.3 *Interconversion synthesis*

Pt_3Sn was synthesized by first dispersing 10.7 mg of PtSn intermetallic powder in 20 mL TEG by sonication and magnetic stirring. After the dispersion was vigorously stirred at room temperature under bubbling Ar for at least 1 hour, it was heated to 125 °C, at which temperature 6.820 mL of a 10.0 mM solution of K_2PtCl_6 in TEG was slowly added. The dispersion was slowly heated to 260 °C and held at that temperature for 15 min, then removed from heat and allowed to cool under bubbling Ar. This Pt_3Sn product was converted back to PtSn by the same method outlined above, dispersing 4.9 mg Pt_3Sn powder in 20 mL TEG, stirring under Ar for 1 hour, heating to 120 °C, slowly adding a solution of 4.1 mg [3 molar equivalents] $SnCl_2$ in 2 mL TEG, and heating to 260 °C and holding for 30 min. The conversion of PtSn to $PtSn_2$ and back to PtSn was achieved by using this same method, with the following exceptions: $PtSn_2$ was synthesized from PtSn by reacting 3 molar equivalents of Sn^{2+} at 275-280 °C for 30 min. The $PtSn_2$ was converted back to PtSn by reacting with 1.5 molar equivalents of Pt^{4+} at 255 °C for 2 hours.

Ni_3Sn_2 was converted to Ni_3Sn_4 by first dispersing 7.0 mg Ni_3Sn_2 in 20 mL TEG by sonication and magnetic stirring. The dispersion was vigorously stirred at room temperature under bubbling Ar for 1 hour, and 97 mg PVP (MW = 40 000) was added and dissolved by stirring. The solution was heated to 185 °C and 19.7 mg [6 molar equivalents] $SnCl_2$ in 2 mL TEG was added. After 5 min, 3 mL of a 0.159 M $NaBH_4$ solution in TEG was added slowly. The heat was increased to 220 °C and held for 10 minutes, then removed from heat and allowed to cool under bubbling Ar.

AuCu was converted to $AuCu_3$ by first dispersing 2.2 mg AuCu in 15 mL TEG by sonication and magnetic stirring. After the dispersion was vigorously stirred at room temperature under bubbling Ar for 1 hour, it was heated to 125 °C and 3 molar equivalents of $Cu(C_2H_3O_2)_2\cdot H_2O$ in 2 mL TEG was added. The dispersion was slowly heated to reflux and held for 40 min, then removed from heat and allowed to cool under bubbling Ar. Powders were precipitated from solution by centrifugation and were washed thoroughly with ethanol.

5.2.4 *Characterization*

Powder X-ray diffraction (XRD) data were collected on a Bruker GADDS three-circle X-ray diffractometer using Cu Kα radiation. Transmission electron microscopy

(TEM) images, selected area electron diffraction (SAED) patterns, and energy-dispersive X-ray analysis (EDS) were collected using a JEOL JEM-2010 TEM. Samples were prepared by sonicating the nanocrystalline intermetallic powders in ethanol and dropping a small volume onto a carbon-coated nickel or copper grid.

5.3 Intermetallic interconversion in the Pt-Sn system

Nanocrystalline PtSn, Ni_3Sn_2, and AuCu were synthesized by $NaBH_4$ reduction of the appropriate metal salts in tetraethylene glycol (TEG), followed by heating to 245-310 °C, as described previously.[35,48] These nanocrystalline solids were then isolated by centrifugation, washed several times, and fully characterized by powder XRD, SAED, and EDS. Serving as out-of-the-bottle reagents, the nanocrystalline intermetallics were then redispersed in TEG and thermally reacted with metal salt solutions. No added surfactants or surface stabilizers were used, while only the conversion of Ni_3Sn_2 to Ni_3Sn_4 required added reducing agents.

Figure 5.1 shows an overview of the chemical transformations that can be accomplished using nanocrystalline PtSn as a solid-state reagent. In the first reaction, NiAs-type PtSn is successfully converted to CaF_2-type $PtSn_2$ by reacting nanocrystalline PtSn with a TEG solution of $SnCl_2$ at 280 °C for 40 min (Fig 5.2). It is clear that heating the PtSn dispersion in the presence of $SnCl_2$ to 225 °C does not produce a reaction, however further heating to 270 °C yields a mixture of PtSn and $PtSn_2$. Upon further heating to 280 °C, the reaction is complete and the product appears to be phase-pure $PtSn_2$ by XRD. While the XRD data convincingly support the conversion from PtSn to

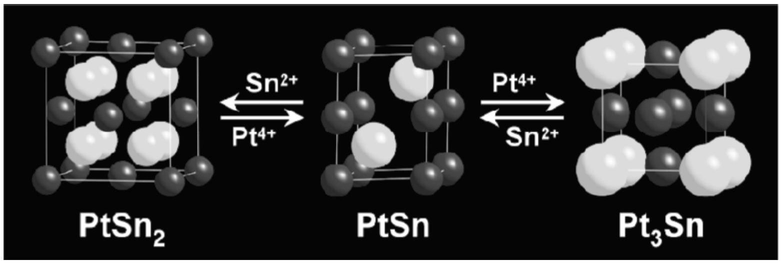

Figure 5.1 Schematic of the intermetallic interconversions that can be carried out using nanocrystalline PtSn as an out-of-the-bottle reagent.

PtSn2, the melting point of tin is 231 °C, and it is possible that molten tin could provide a localized flux to facilitate diffusion. Thus, we also studied the reaction of PtSn with Pt. PtSn can be converted to Cu_3Au-type Pt_3Sn by reacting nanocrystalline PtSn with K_2PtCl_6 at 260 °C for 20 min (Figure 5.3a). The diffraction pattern of Pt_3Sn has broad peaks; the small superlattice peaks at 22 and 32° 2θ, which are diagnostic of the 3:1 intermetallic, are not resolvable. However, annealing this product at 600 °C under Ar sinters the particles, making the ordering reflections resolvable. Comparison to the simulated XRD pattern for Pt_3Sn confirms that the 3:1 intermetallic was indeed formed (Figure 5.3b).

In addition to converting PtSn to $PtSn_2$ and Pt_3Sn at low temperatures, the reactions are reversible. The XRD data in Figure 5.4 show that $PtSn_2$, formed by the reaction of PtSn with $SnCl_2$, can be converted back to PtSn by reaction with K_2PtCl_6. Likewise, Pt_3Sn, formed by reacting PtSn with K_2PtCl_6, can be converted back to PtSn by reaction with $SnCl_2$ (Figure 5.3a). The ability to reversibly interconvert these intermetallics highlights the unusual reactivity inherent in nanoscale metallurgical systems and demonstrates the level of control over composition and structure that is

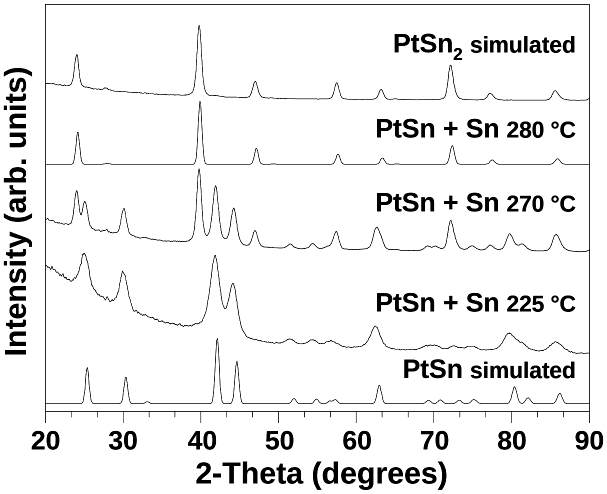

Figure 5.2 Powder XRD patterns of the reaction of nanocrystalline PtSn with a TEG solution of $SnCl_2$ as a function of temperature. At 225 °C, the product matches the PtSn simulated pattern (bottom), as no reaction has occurred. As the temperature increases, the $PtSn_2$ phase grows in, and at 280 °C the pattern matches the $PtSn_2$ simulation (top).

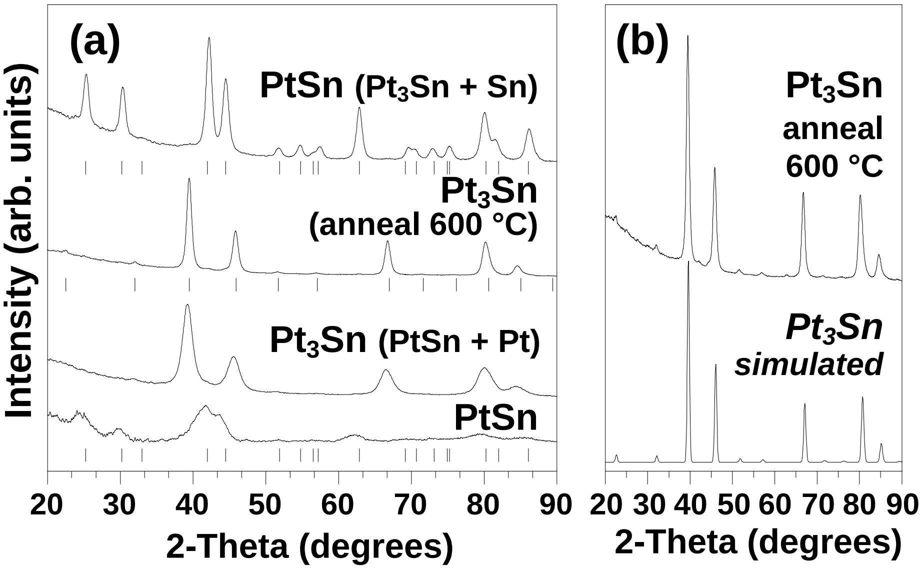

Figure 5.3 Powder XRD patterns showing (a) the conversion of PtSn to Pt_3Sn and the reverse reaction that converts Pt_3Sn to PtSn. The data shown are for sequential reactions, e.g., each reaction uses the previous product. Tick marks below each pattern represent the expected peak positions. (b) Pt_3Sn annealed at 600 °C to show the superlattice peaks located at about 23 and 33 degrees 2θ.

achievable using simple solution reactions.The XRD data in Figures 5.3 and 5.4 show that the peak widths decrease and, consequently, the particle sizes increase as the conversion reactions progress. The increase in particle size is necessary from a mass balance perspective, because each reaction involves the addition of more material to the nanocrystals. Sintering, caused by the high-temperature solution reaction, is also likely to play a role in particle growth.

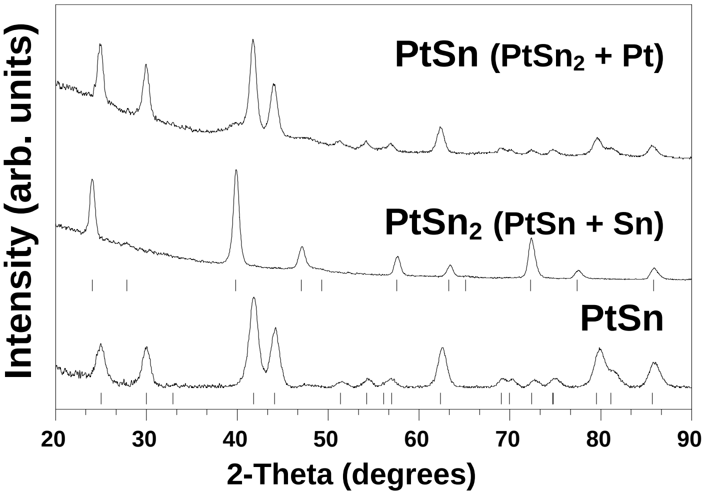

Figure 5.4 Powder XRD patterns showing the conversion of PtSn to $PtSn_2$ and the reverse reaction that converts $PtSn_2$ to PtSn. The data shown are for sequential reactions. Tick marks below each pattern represent the expected peak positions.

TEM images of the PtSn → Pt_3Sn → PtSn reaction sequence (Figure 5.5) provide additional insight into the progressive change in morphology and crystallite size, in addition to confirming the structures based on the SAED patterns. The nanoparticles of the PtSn reagent are approximately 2-5 nm (Figure 5.5a), which is consistent with the

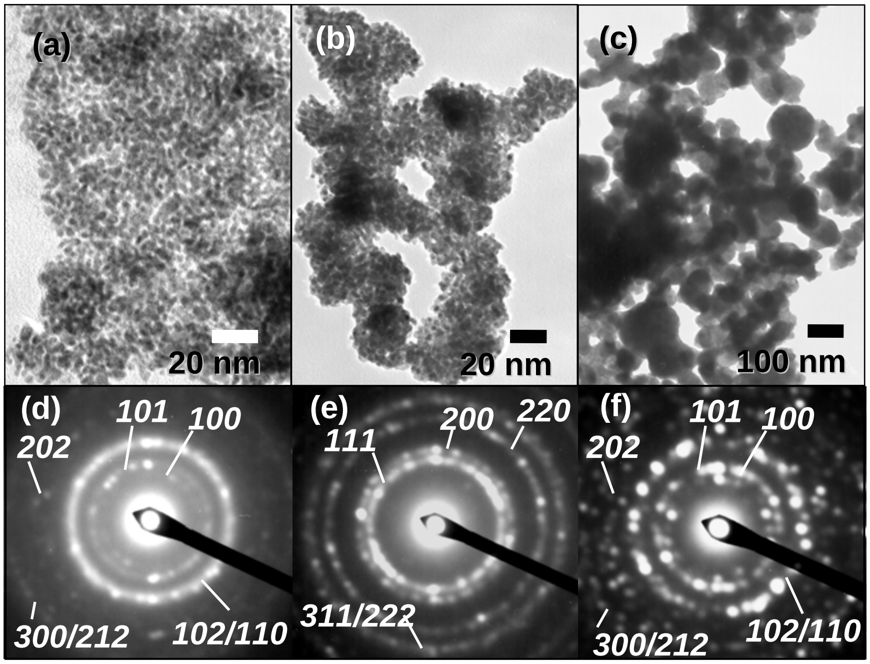

Figure 5.5 TEM micrographs and SAED patterns for (a) NiAs-type PtSn reagent, (b) Cu_3Au-type Pt_3Sn formed by reacting PtSn with K_2PtCl_6, and (c) NiAs-type PtSn formed by reacting Pt_3Sn with $SnCl_2$.

XRD data shown in Figure 5.3a. After conversion to Pt_3Sn, the particles grow to approximately 3-7 nm (Figure 5.5b), which is consistent with both the XRD data in Figure 3a and the expected volume expansion inherent in converting PtSn to Pt_3Sn.

Upon converting Pt_3Sn back to PtSn, the particle size increases dramatically (Figure 5.5c). The particle sizes are difficult to quantitate because of significant coalescence. However, when the TEM micrographs for Pt_3Sn (Figure 5.5b) and PtSn that were synthesized using Pt_3Sn as a reagent (Figure 5.5c) were compared, the PtSn particles appear to have formed from the coalescence of aggregates of smaller Pt_3Sn particles, perhaps facilitated by the reaction with low-melting tin. In addition to controlling the composition and crystal structure, this solution-mediated reaction appears to produce systematic increases in particle size, which implies that this approach could be useful for fine-tuning the morphological characteristics of nanocrystalline intermetallics.

5.4 Extension to other systems: Ni-Sn and Au-Cu

In an effort to generalize the approach, similar chemical transformation were attempted with the Ni-Sn and Au-Cu systems. Figure 5.6 shows XRD data for the conversion of $InNi_2$-type Ni_3Sn_2 to CoGe-type Ni_3Sn_4 in which a colloidal suspension of Ni_3Sn_2 with added $SnCl_2$ was reduced at 190 °C with $NaBH_4$. As expected, the XRD peaks of the product become more narrow upon reacting Ni_3Sn_2 with Sn, indicating particle growth, and after 20 minutes of heating at 190 °C the diffraction pattern is essentially unchanged and matches the Ni_3Sn_4 simulated pattern fairly well. Upon close inspection, there is a discrepancy in the peak intensities in the experimental and simulated patterns at about 44 and 45 degrees 2θ. The peak at 44 degrees in the experimental pattern is more intense than the peak at 45 degrees, which is the opposite of the relative intensities seen in the simulated pattern. This discrepancy could be the result of some unreacted Ni_3Sn_2 in the sample, which does have an intense set of peaks at 44 degrees. Unfortunately, this impurity would be very difficult to characterize without very high resolution XRD because of the overlapping reflection angles. Unlike

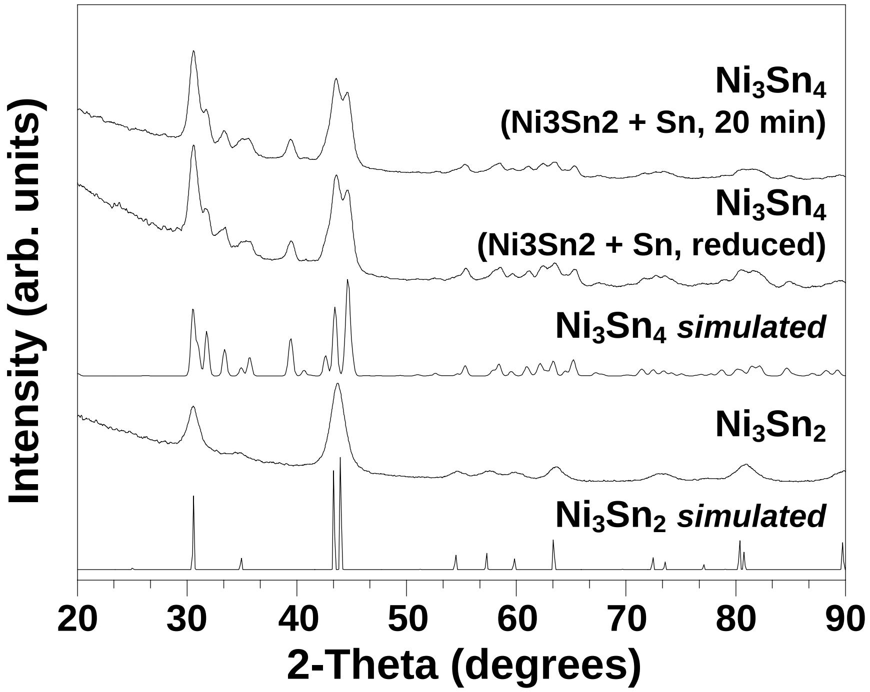

Figure 5.6 Powder XRD patterns showing the conversion of nanocrystalline Ni_3Sn_2 to Ni_3Sn_4 with the aid of $NaBH_4$. Simulated patterns for Ni_3Sn_2 (bottom) and Ni_3Sn_4 (top) are shown for reference.

the Pt-Sn system, conversion in the Ni-Sn system could not be achieved without the use of $NaBH_4$, and the conversion was not reversible.

Conversely, the Au-Cu system did behave similarly to the Pt-Sn system. Figure 5.7 shows XRD data for the nanocrystalline AuCu reagent as well as $AuCu_3$ that was formed by reacting AuCu with $Cu(C_2H_3O_2)_2 \bullet H_2O$ in TEG at ~315 °C without any added surface stabilizer or reducing agent. Interestingly, the peak width appears to increase upon conversion, which may suggest that the $AuCu_3$ product was less crystalline than the starting material, or that the addition of Cu fractured the starting particles. The conversion of AuCu to $AuCu_3$ is particularly important, as both Au and Cu are high-

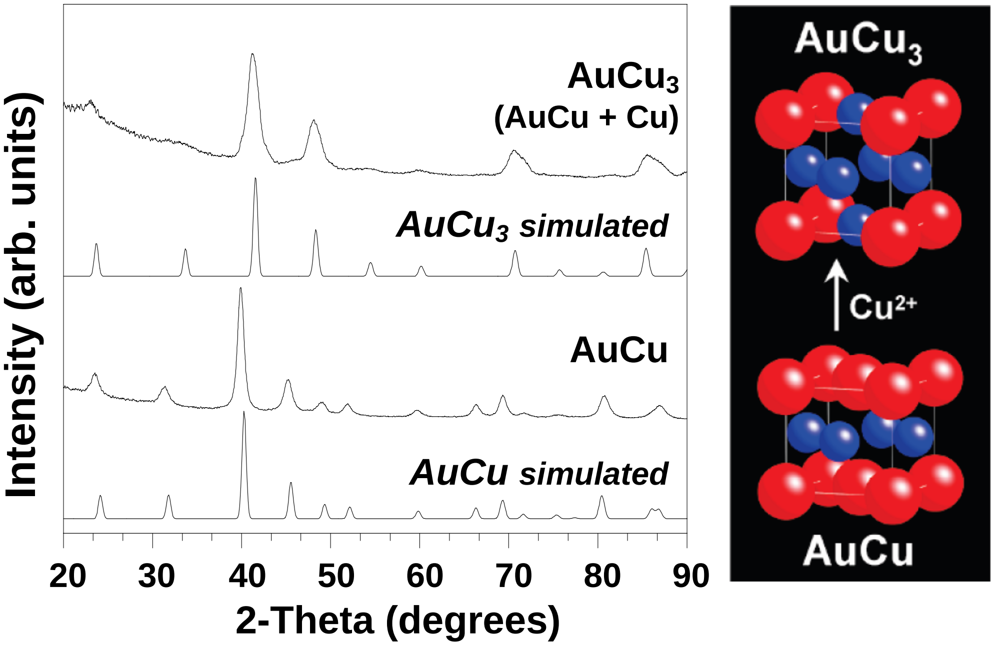

Figure 5.7 Powder XRD data and schematic for the conversion of nanocrystalline AuCu into $AuCu_3$ by reaction with $Cu(C_2H_3O_2)_2 \bullet H_2O$. The schematic shows the structural conversion, in which the large atoms are Au and the small are Cu.

melting metals (relative to Sn) and support the idea that the low-temperature diffusion is facilitated by the decreased particle size of the nanocrystals.

5.5 Summary

The discovery that nanocrystalline intermetallics undergo facile interconversion in solution has several important implications. First, it provides a robust toolkit for systematically modifying the compositions and structures of multi-metal nanocrystals, which could help fine-tune magnetic, optical, and catalytic properties and could possibly allow access to structures that are not accessible using traditional methods. Along those lines, while Pt_3Sn was readily accessible using nanocrystalline PtSn as a reagent, our attempts at synthesizing this compound using direct one-pot reactions failed up to this point. Thus, this conversion strategy produces nanocrystals of important compounds that are difficult to make by other methods. In particular, Pt_3Sn and related Pt-Sn alloys are emerging as important catalysts for fuel cell reactions,[9] and this strategy readily produces these materials as nanocrystals. Also, while the size dependence of the reactivity and details of the reaction mechanism have yet to be established, it may be possible to use this solution approach to interconvert nanoscale intermetallics formed by other methods, including ball milling and thin film deposition. Finally, this work adds to a growing toolbox of low-temperature reactions for accessing nanocrystalline alloys and intermetallics[23,42,45,47-79,125-128] and, as such, could aid in the formation of new and complex solids and challenge our thinking about the reactivity of materials traditionally considered as inert and unreactive.

CHAPTER VI

PATTERNED SURFACE DIRECTED ASSEMBLY: A VERSATILE APPROACH TO COLLOIDAL CRYSTAL MICROARRAYS AND TWO-DIMENSIONAL SUPERSTRUCTURES*

6.1 Introduction

Robust methods for directing the assembly of colloids are important for developing new materials with increasingly complex structures. Crystalline arrays of monodisperse spherical colloids (colloidal crystals) are particularly interesting as photonic band gap (PBG) materials, which hold promise for manipulating light in optical and optoelectronic devices.[129] To fully realize the potential of self-assembled colloidal crystals as PBG materials, it is necessary to control both the crystal structure and the surface patterning. Approaches such as epitaxial assembly,[130,131] controlled sedimentation,[132] convective selfassembly,[133,134] and field-induced alignment[135] are paving the way toward structural control in colloidal crystals. Likewise, techniques such as micromolding in capillaries (MIMIC),[136] template-directed assembly,[137,138] and chemical surface patterning[139] are yielding control over surface deposition and

---

* Reprinted in part with permission from *Langmuir, 20* Schaak, R. E.; Cable, R. E.; Leonard, B. M.; Norris, B. C. "Colloidal Crystal Microarrays and Two-Dimensional Superstructures: A Versatile Approach for Patterned Surface Assembly," 7293, Copyright 2004 by the American Chemical Society.

positioning. Using such methods, prototype on-chip PBG materials based on self-assembled colloidal crystals have been fabricated.[140]

An ideal approach for controlling the surface patterning of colloidal crystals will allow maximum flexibility of design while maintaining simplicity and ensuring generality. In this chapter, we demonstrate a simple and robust approach to colloidal assembly that is amenable to both large-scale on-chip patterning and micron-scale structural control. The idea is based on the spontaneous crystallization of spherical colloids into lithographically defined templates during a controlled dewetting process. As such, it integrates aspects of template-assisted self-assembly,[137] epitaxial assembly,[130,131] and MIMIC[136] into a novel new approach that is remarkably versatile and fast. Using this method, we can quickly and easily fabricate close-packed colloidal crystal microarrays of both silica and polystyrene spheres that range in size from 500 nm to 4.5 μm, and we can also access new colloidal crystal surface structures using epitaxial templates. In addition, we have investigated an alternative method for fabricating epitaxial templates which can access nanometer scale features without the high cost and complexity of electron-beam and x-ray lithography. The method combines the use of Nanosphere Lithography (NSL), a method in which a hexagonal array of metal dots can be deposited on a surface through the use of a colloidal crystal monolayer mask,[141] and anisotropic reactive ion etching.

Our colloidal deposition approach offers several distinct differences from other methods currently in use. First, it allows for *addressable patterning*, where colloidal crystal arrays comprised of different-sized spheres can be patterned on the same chip, rather than requiring the entire chip to be patterned with the same composition using other immersion-based techniques. This could be particularly useful for developing microaddressable multiwavelength photonic sensor films. Second, this approach is *materials general*, since it works for both polymer and silica spheres that range in size from visible to IR wavelengths. Finally, it allows for *rapid deposition within minutes*, which is useful for quickly screening both the optimal deposition conditions and the feasibility of surface template libraries and sphere sizes for generating desired surface structures and superlattices.

6.2 Experimental details

100-μm × 100-μm wells were fabricated using standard photolithography techniques. A 5-μm thick film of either positive (Microchem SU-8 2005) or negative (Shipley SC1827) photoresist was spincoated onto a glass slide that had been recleaned in an O_2 plasma. Exposure was made through a low-resolution photoreduced mask that was produced in-house. Micropegboard arrays (pillars of 2.6-5.0-μm diameter) were fabricated using negative resist and a commercially prepared mask. Polystyrene (PS) spheres were purchased from Interfacial Dynamics Corporation (Portland, OR). Monodisperse 550-nm SiO_2 spheres were synthesized using the Stober-Fink-Bohn method.[140] A 5 μL drop of a 4% aqueous suspension of 1.0-4.5-μm spheres was placed on a 10 × 10 array of microwells, and after 5-30 min was quickly dewetted using a Kim-Wipe. Multiple arrays on the same glass substrate were simultaneously treated.

Scanning electron microscope images were obtained at 15 kV using a JEOL JSM-6400 SEM. Prior to imaging, samples were coated with 50-nm of Au/Pd.

Periodic arrays of silicon pegs were made by combining nanosphere lithographic templating with anisotropic plasma etching. A volume of 7 μL of 4.5-μm PS spheres (diluted sixfold in methanol by volume) was dropcast on Si chips to create a monolayer of close-packed spheres. Following monolayer deposition, 50-nm of chromium was deposited on the chips in a BOC Edwards Auto 306 Metal Evaporation Chamber, and the PS spheres were later removed by sonication in CH_2Cl_2, leaving a hexagonal array of triangular Cr dots. To yield Si pegs, the silicon chips were then etched in a March Plasma Systems CS-1701 Reactive Ion Etcher with a CHF_3/O_2 plasma with the following parameters: 150 W, 100 mTorr, 20 standard cubic centimeters per minute (sccm) CHF_3, and 2 sccm O_2.

6.3 Colloidal crystal microarrays

To demonstrate the concept, shown schematically in Figure 6.1, 5 μL drops of an aqueous suspension of colloidal polystyrene spheres were placed on 10 × 10 arrays of 100-μm × 100-μm × 5-μm wells that had been lithographically patterned in photoresist on a glass substrate. The aqueous suspension beads up on the hydrophobic photoresist surface, and it can be easily dewetted by removing the solvent and excess spheres through capillary action into an absorbent laboratory cloth (Kim-Wipe). For the polystyrene spheres used in this study (1.0-4.5-μm), gravitational forces cause the spheres to settle into the wells. At the same time, the forces involved in the subsequent

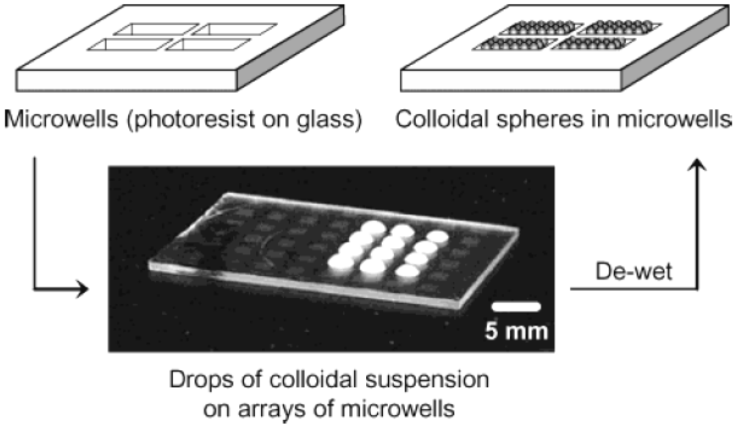

Figure 6.1 Schematic of the patterned assembly of colloidal crystal microarrays. The photograph of a representative sample shows a 38-mm × 25-mm glass substrate with 48 individual arrays, each of which contains a 10 × 10 microarray of 100-μm × 100-μm wells. A 5 μL aqueous suspension of 2.8-μm polystyrene spheres covers 12 of the 10 × 10 microwell arrays. Note that the schematic representations show only 4 individual microwells, a small subset of a single microarray, while the photograph shows 48 complete microarrays.

dewetting process help push the spheres into the surface depressions. After 20 min, the surface is quickly dewetted, and the spheres that remain in the wells crystallize into a close-packed monolayer. (Different suspensions can be placed on each individual microwell array, allowing complex multicomponent array systems on a single chip.)

Figure 6.2 shows a large array of microwells filled with colloidal crystal monolayers of 4.5-μm polystyrene spheres. The inset to Figure 6.2 shows empty wells for comparison. Optical micrographs of individual wells filled with crystallized 4.5-μm and 1.8-μm spheres are shown in Figures 6.3a and 6.3b, respectively. Scanning electron microscope (SEM) images of individual wells containing crystallized 4.5-μm and 2.8-μm spheres are shown in Figures 6.3c and 6.3d, respectively. In contrast to the monolayer shown in Figure 6.3a, the SEM image of a different sample of crystallized 4.5-μm

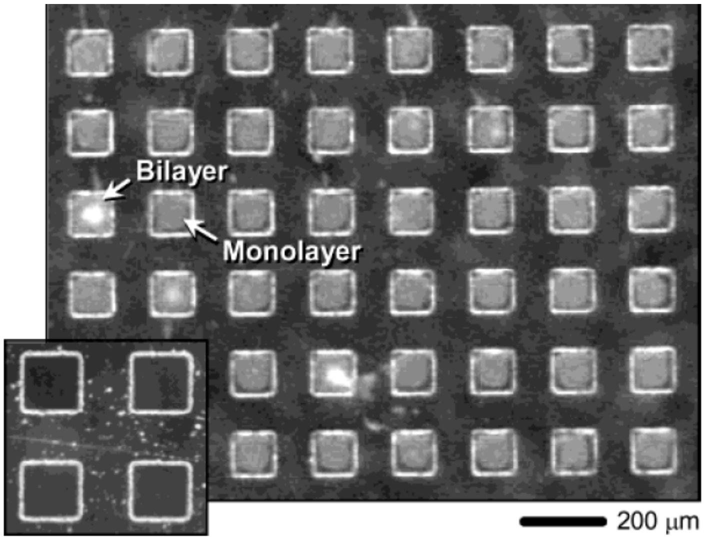

Figure 6.2 Darkfield optical microscope image of an array of 4.5-μm polystyrene spheres crystallized in 100-μm × 100-μm microfabricated wells. The difference between monolayer and bilayer regions is highlighted. Empty wells are shown for comparison in the inset.

spheres in Figure 6.3c shows a bilayer region in the center of the crystal. Similar bilayers are evident in some of the wells in Figure 6.2. The tendency to form bilayer regions increases with thicker photoresist and longer settling time prior to dewetting, which can be exploited to assemble multilayer colloidal crystal arrays. As expected from the nature of the rapid self-assembly process and the slight irregularities of the in-house template, multiple domains and defects are evident, although local crystalline order dominates the arrays.

After thermally interconnecting the polystyrene spheres by heating to 96 °C for 8 min,[137,143] the photoresist can be removed to yield self-supported monodisperse microarrays of colloidal crystals. Free-standing two-dimensional colloidal crystals

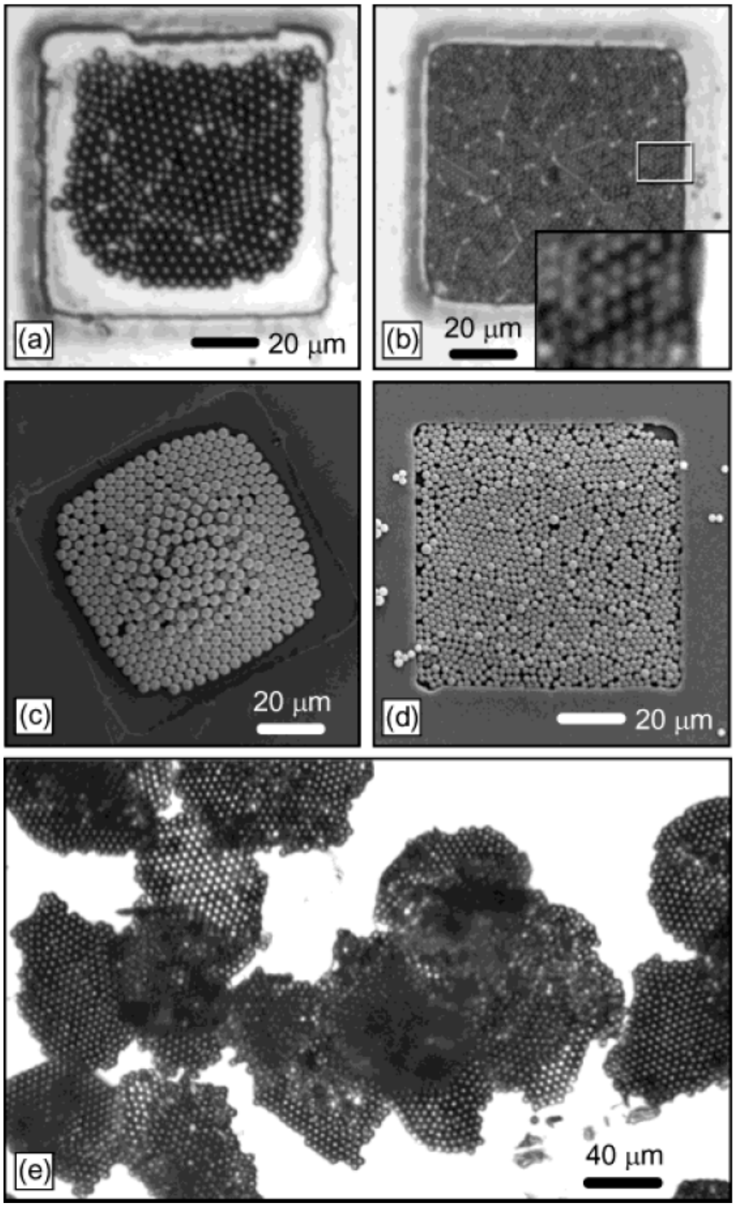

Figure 6.3 SEM images of colloidal superstructures. In (a), a graphite-structured lattice forms for d_{pillar} = 4.0-μm and d_{sphere} = 2.8-μm (photoresist pillars are dark gray, polystyrene spheres are light gray). The surface structure shown in (b) is a kagome lattice (photoresist pillars are light gray, polystyrene spheres are darker gray), which forms for d_{pillar} = 2.8-μm and d_{sphere} = 2.8-μm. A kagome sphere-on-sphere (eclipsed) bilayer pattern is shown in (c). Cubic (d), linear chain (e), and disordered (f) structures form for different ratios of sphere diameter to pillar diameter (see text for details).

can be obtained by lifting off the photoresist, sonicating the surface in ethanol for a few seconds, and drying the ethanolic suspension. The monodisperse colloidal crystals from several microarrays were concentrated by centrifugation at 1000 rpm, dried, and then transferred to a glass microscope slide to obtain the optical micrograph shown in Figure 6.3e. This process is analogous to the approach used by Xia *et al.*[137] to prepare free-standing colloidal clusters and one-dimensional chains. To our knowledge, the free-standing colloidal crystal slabs in Figure 6.3e represent the first example of discrete *two-dimensional* colloidal crystals, and they could potentially be useful as building blocks for more complex colloidal crystal assemblies.

To demonstrate that this simple patterning approach can be generalized to other types of materials, we also studied the crystallization of monodisperse silica spheres. An array of close-packed colloidal crystals assembled from an ethanol suspension of monodisperse 550-nm SiO_2 spheres is shown in Figure 6.4a, yielding results similar to those obtained for larger polystyrene spheres. In the case of submicron silica spheres, however, significant settling due to gravitational forces does not occur during the short time the colloidal suspension is in contact with the surface prior to dewetting. Interestingly, the silica spheres crystallize in the microwells after less than 5 min of exposure. In this case, it is likely that the hydrophilic interactions between the silica spheres and the glass substrate, combined with capillary forces and the repulsion between the hydrophobic photoresist and hydrophilic spheres and solvent, drive the surface patterning and subsequent crystallization. An SEM micrograph of a single microwell filled with crystallized silica spheres is shown in Figure 6.4b. The

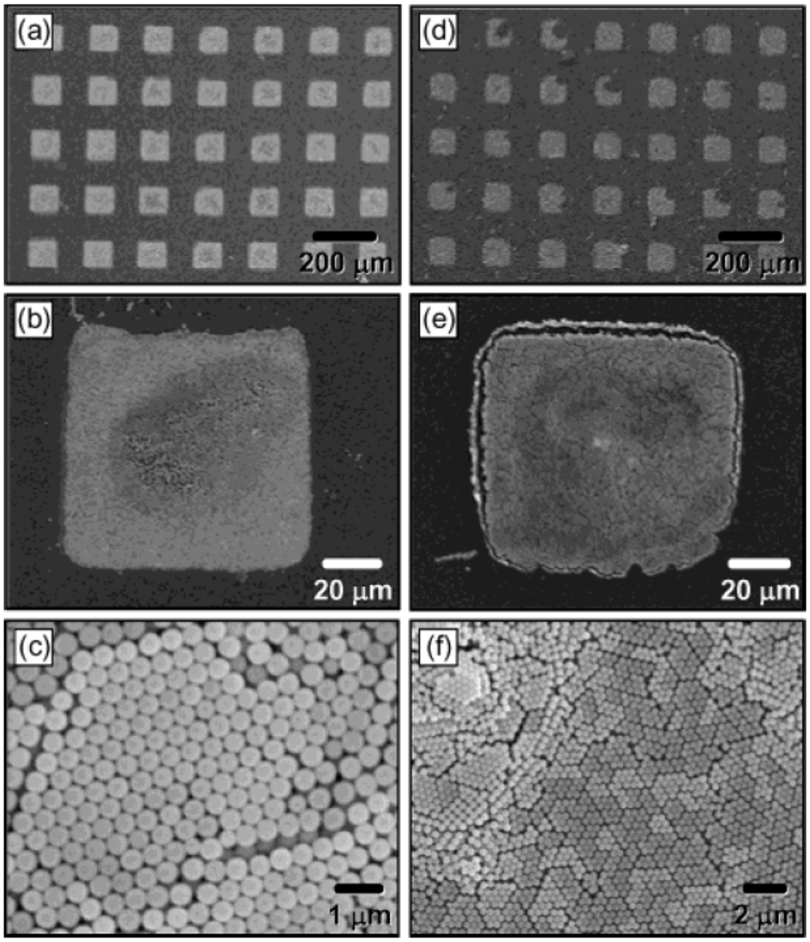

Figure 6.4 SEM images of microarrays of 550-nm SiO_2 spheres crystallized in 100-*μ*m × 100 *μ*m microfabricated wells. A large microarray is shown in (a), along with higher-resolution images in (b) and (c). Panel (d) shows a microarray after removal of the photoresist by heating to 600 °C, and (e) and (f) show higher resolution images. The thicknesses of the colloidal crystals range from 1 to 4 layers.

higher resolution image in Figure 6.4c confirms that the microwell consists of a close-packed colloidal crystal of 550-nm SiO_2 spheres. Multilayer regions are prevalent. Since the silica spheres are thermally stable, the photoresist can be removed by heating to 600 °C for 2 h, yielding a self-supported colloidal crystal microarray (Figure 6.4d).

Higher-magnification SEM images (Figure 6.4e,f) confirm that the microarrays remain intact, although some sintering and cracking is evident.

For both the polystyrene and silica microarrays, the domain sizes appear to be somewhat correlated to the ratio of the template dimensions (length, width, and depth) to the sphere sizes. For the largest polystyrene spheres (1.0-4.5-μm), average ordered domain sizes range from 5 × 5 spheres to 15 × 15 spheres in a 100-μm × 100-μm × 5-μm box. For the smaller silica spheres, the domain sizes are generally larger, often greater than 20 × 20 spheres.

6.4 Colloidal crystal superlattices

The concept of epitaxial template-directed colloidal crystallization was pioneered by Wiltzius and van Blaaderen to prepare oriented crystals and crystal structures that deviate from a close-packed lattice,[130,131] and Xia and co-workers used similar techniques to assemble size-controlled colloidal clusters[137] and oriented colloidal crystals.[144] To further demonstrate the versatility of our simple approach to colloidal surface patterning, we studied the epitaxial deposition of polystyrene spheres using a quick dewetting process. For a microfabricated array of 4.0-μm pillars of photoresist on glass, dewetting an aqueous suspension (4 wt %) of 2.8-μm polystyrene spheres ($d_{\text{sphere}} \approx 2/3\ d_{\text{peg}}$) after only 10 min of settling time yielded the two-dimensional graphite-type surface structure shown in Figure 6.5a. For 2.8-μm pillars ($d_{\text{sphere}} \approx d_{\text{peg}}$), the same process yielded the two-dimensional superstructure shown in Figure 6.5b. This superstructure is related to the kagome lattice, which is common in magnetically

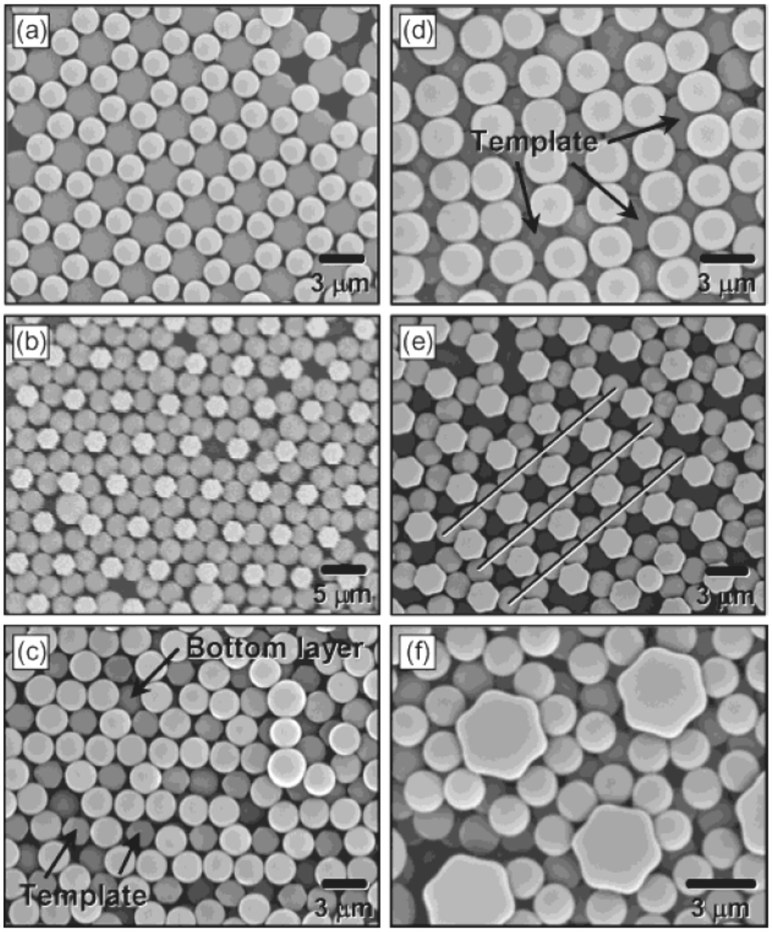

Figure 6.5 SEM images of colloidal superstructures. In (a), a graphite-structured lattice forms for d_{pillar} = 4.0-μm and d_{sphere} = 2.8-μm (photoresist pillars are dark gray, polystyrene spheres are light gray). The surface structure shown in (b) is a kagome lattice (photoresist pillars are light gray, polystyrene spheres are darker gray), which forms for d_{pillar} = 2.8-μm and dsphere = 2.8-μm. A kagome sphere-on-sphere (eclipsed) bilayer pattern is shown in (c). Cubic (d), linear chain (e), and disordered (f) structures form for different ratios of sphere diameter to pillar diameter (see text for details).

frustrated solids. Van Blaaderen *et al.*[131] observed a similar phase during layer-by-layer epitaxial self-assembly of submicron SiO_2 spheres. Our results indicate that such structures can form in minutes, rather than hours or days. Interestingly, deposition from a higher concentration of 2.8-μm spheres (8 wt %) yields an interesting eclipsed bilayer kagome structure (Figure 6.5c), where the second layer of spheres sits directly on top of the first layer. The fact that the bilayer adopts an eclipsed rather than a staggered conformation likely results from the rapid dewetting process, which dries the spheres before they have a chance to reach their equilibrium positions.

By adjusting the ratio of the template diameter to the sphere diameter, we are able to access other two dimensional colloidal superlattice structures. For example, for $d_{\mathrm{sphere}} \approx 3/4\ d_{\mathrm{peg}}$ a cubic superlattice forms in a distorted body-centered cubic arrangement (Figure 6.5d). For $d_{\mathrm{sphere}} \approx 4/5\ d_{\mathrm{peg}}$, a linear chain dominates the observed superlattice structures (Figure 6.5e). For spheres that are compared to the diameter of the template pillars ($d_{\mathrm{sphere}} \approx 1/2\ d_{\mathrm{peg}}$), a disordered multilayer structure forms and completely surrounds the pillars (Figure 6.5f).

An interesting open triangular lattice (Figure 6.6a, c) forms when 4.5-μm polystyrene spheres are dewetted from a pegboard array of 3.0-μm pillars ($d_{\mathrm{sphere}} \approx d_{\mathrm{peg}}$). Bilayer regions (Figure 6.6b, d) of tetrahedral geometry are also observed when dewetting from more concentrated colloidal suspensions. Such open, lower-symmetry colloidal crystal structures are of interest for their photonic properties.

We were also able to quickly form binary colloidal crystal structures, which remain rare because of the difficulty associated with controlling the uniform coassembly of multiple sphere sizes. Figure 6.6e shows evidence of an open binary superlattice, which was formed by first depositing an open hexagonal network of 4.5-μm spheres, as shown in Figure 6.6a, followed by depositing 2.4-μm spheres to fill in the spaces between the larger spheres. The resulting structure can be viewed as a superlattice of

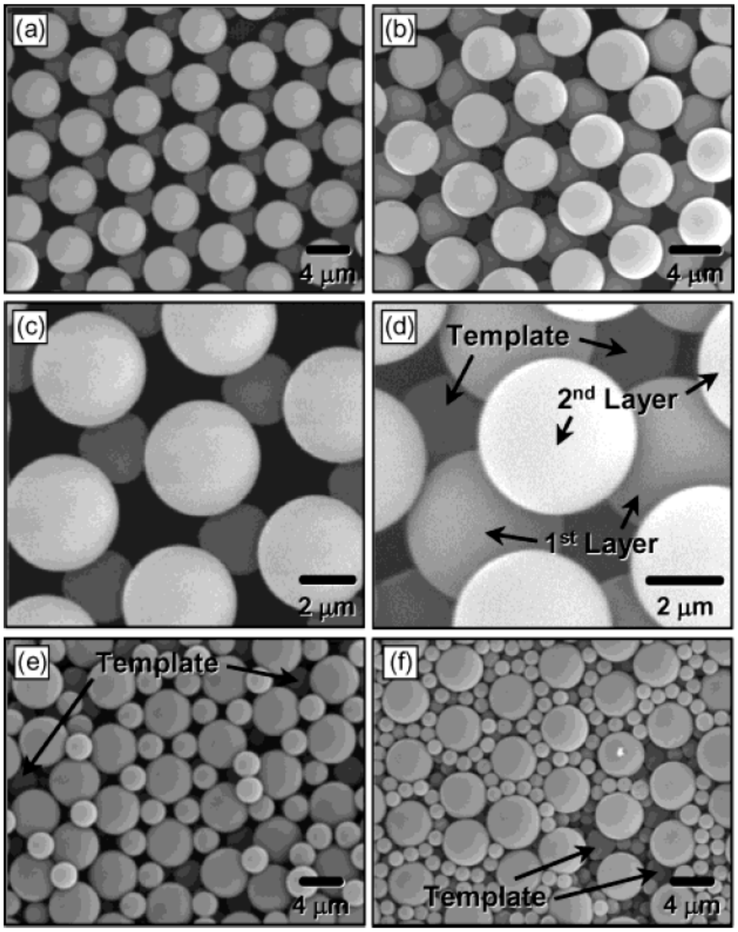

Figure 6.6 SEM images of open-structured colloidal superlattices. An open triangular monolayer lattice is shown in (a), which forms for d_{pillar} = 3.0-μm and d_{sphere} = 4.5-μm using a 4% colloidal suspension. A related bilayer structure forms for an 8% colloidal suspension (b). Enlarged views of (a) and (b) are shown in (c) and (d), respectively. A binary graphite/open hexagonal superstructure of 4.5-μm and 2.4-μm spheres is shown in (e), along with a related binary superlattice of 4.5-μm and 1.4-μm spheres (f).

both the open hexagonal and graphite structures, where the hexagonal network of 4.5-μm spheres serves as a template for the 2.4-μm spheres to crystallize in the graphite structure. When smaller spheres (1.4-μm) are used in the second deposition step, a random network of small spheres surrounds the open hexagonal network of larger spheres (Figure 6.6f). This binary superstructure is similar to that observed by Ozin *et al.* using a different technique.[134]

The superstructures in Figures 5 and 6 are representative of approximately 50% of the surface, and they typically appear in small domains of ca. 20 × 20 spheres. Significantly, larger domains have also been observed. Defect densities for the two-dimensional colloidal crystal superstructures are typically around 3/100 μm^2. At this point, only monolayer and bilayer superstructures have been assembled, although this approach could potentially yield thicker colloidal crystals by using more concentrated colloidal suspensions or sequential deposition techniques.

6.5 Periodic Si pillar arrays through nanosphere lithography

The use of epitaxial templates is highly desirable, however the fabrication of such templates using conventional photolithography has many limitations. Photolithographic techniques initially require the fabrication of an expensive mask which is generally made via electron-beam lithography. Using the conventional photolithographic tools available to us, features much smaller than 1-μm are difficult to achieve. In order to achieve smaller features, NSL has been developed in the van Duyne group.[141] A monolayer of close-packed 2.8-μm polystyrene colloidal spheres are assembled on a substrate and acts as the mask in this process as seen in Figure 6.7. A metal is subsequently evaporated onto this substrate, in this case Cr, covering the spherical particles and the holes between them. The spheres can be selectively removed, leaving a hexagonal array of triangular Cr dots on the substrate surface. Because we are

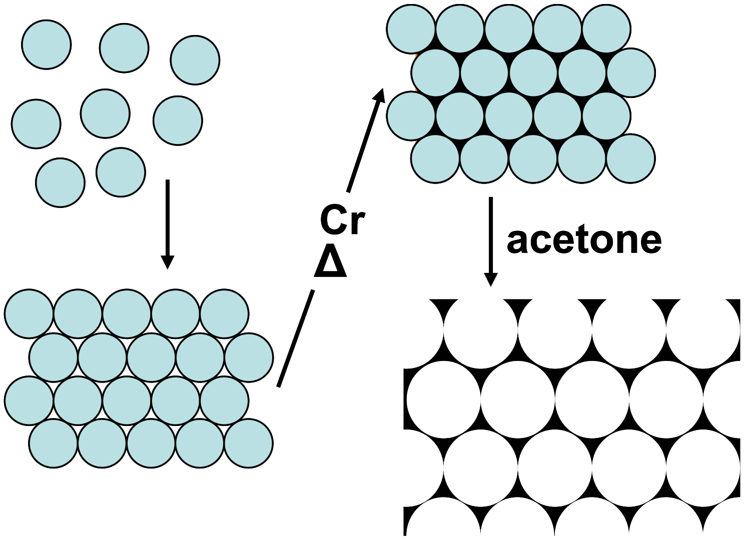

Figure 6.7 Schematic showing the process of creating a colloidal crystal mask for Nanosphere Lithography (NSL). Colloidal polystyrene spheres self assemble into a close-packed monolayer on a substrate. Chromium can subsequently be evaporated over the colloidal crystal mask, which can be removed by soaking in acetone, leaving a hexagonal periodic array of metal particles.

interested in colloidal crystal structures other than hexagonal close-packing, we envisioned the anisotropic etching of the hexagonal dot array on Si to create a hexagonal array of columns. This template may direct spheres to organize in a close-packed layer, with subsequent layers stacking directly on top of lower layers in an AAA fashion, as opposed to the ABABAB or ABCABC stacking of hexagonal and cubic close-packed structures (Figure 6.8).

The use of fluorinated reactive ion plasma to achieve an anisotropic etch is well documented,[145,146] and we used a mixture of CF_4 and O_2 as our process gases. By varying the etch power, pressure, and flow rates of the process gases, we were able to

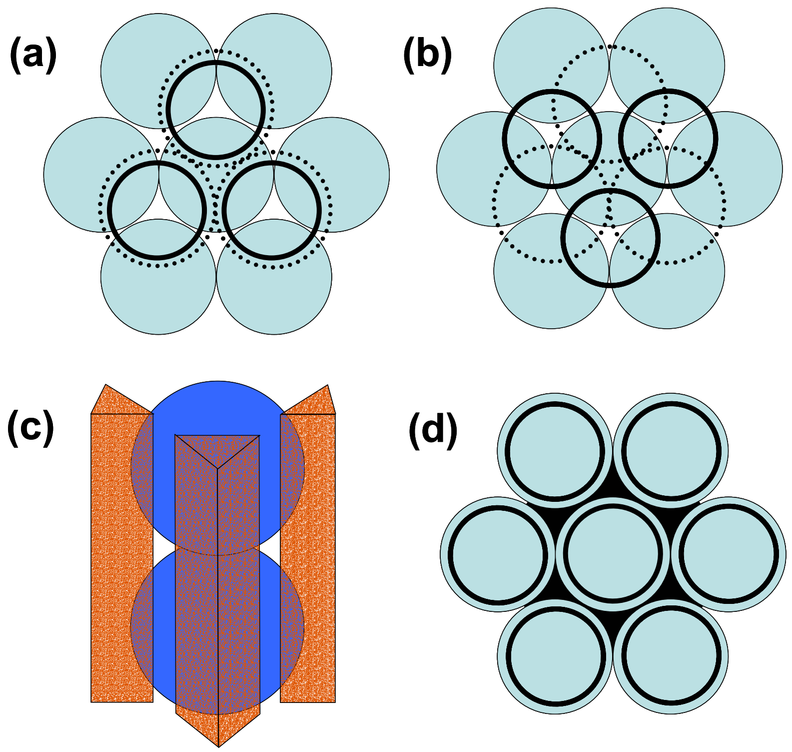

Figure 6.8 Schematic showing different packing structures of spheres formed by self assembly (a, b) and template-directed assembly (c, d). (a) shows the ABABAB sequence of the hexgonal close-packed structure in which the shaded spheres are the middle layer, the dotted spheres are the bottom layer, and the solid open spheres are the top layer which sit directly over the bottom layer. (b) shows the ABCABC structure of the cubic close-packed structure in which the bottom and top layers are staggered. (c) shows the side view of the stacking sequence of two spheres that have been deposited inside a hexagonal periodic pillar template, while (d) shows the top view of such a structure in which each successive layer of spheres sits directly over the previous layer.

achieve an anisotropic etch and produce low aspect-ratio features. Analyzing the etched surfaces, a pattern can be seen which is clearly templated by the monolayer of spheres (Figure 6.9a), and when the surface is tilted to 43 degrees (Figure 6.9b), the 3-dimensional nature of the surface features is apparent. It can be seen that the quality of the final surface pattern reflects the quality of the initial monolayer, so great care must

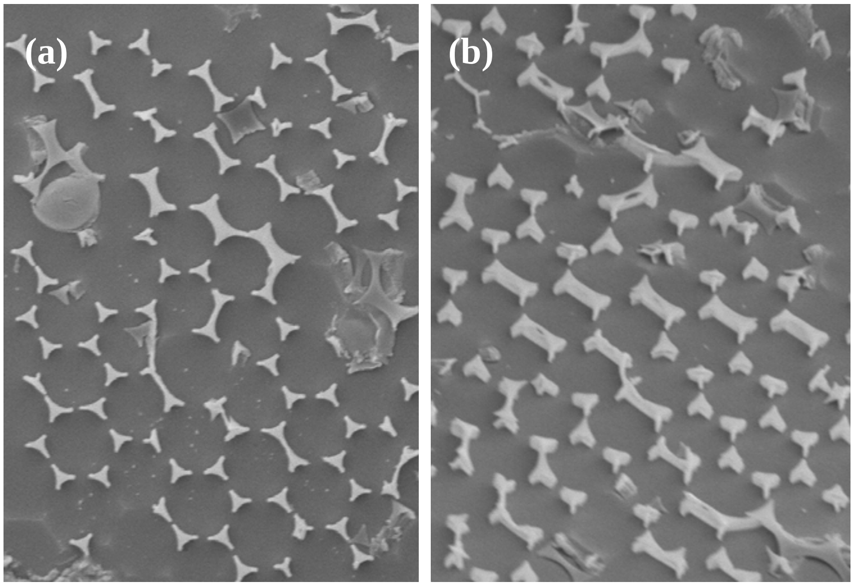

Figure 6.9 SEM images of surfaces patterned by nanosphere lithograpy (NSL) and reactive ion etching (RIE). Micrograph (a) shows a top-down view of the pattern etched into the surface with the hexagonal periodic arrays of short pillars. By tilting the surface to 43 degrees, the 3-dimensional nature of the template can be observed.

be taken in preparing a high-quality monolayer mask. 2.8-μm spheres were re-deposited onto the patterned surface, and as expected the spheres sit preferentially in the spherical sites in the template (Figure 6.10). A binary superlattice similar to that seen in Fig. 6.6e can be made using this NSL template. Initially, a layer of 2.8-μm spheres is deposited on the surface and sit in the spherical template sites. A layer of 1.4-μm spheres was deposited next, and as in Fig 6.6e, it is clear that the hexagonal structure of the 2.8-μm spheres are templating the structure of the 1.4-μm spheres into a graphite structure (Figure 6.11). While the density of the binary superlattice is not high, no attempt has been taken to optimize the process and changing some simple variables such as colloidal concentration and volume would likely improve the density.

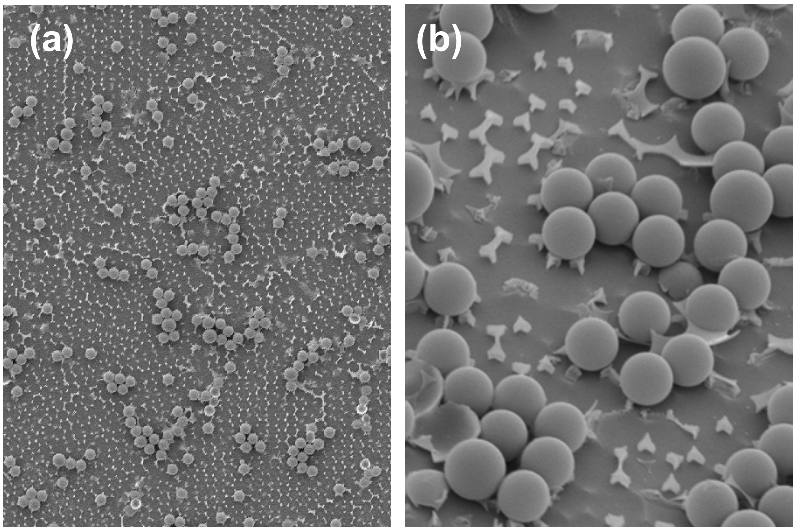

Figure 6.10 SEM images of the NSL/RIE patterned surface upon which 2.8-μm spheres have been re-deposited. Micrograph (a) shows a top-down view of the surface, while (b) is a tilted view which shows the spheres sitting preferentially in the spherical sites in the template.

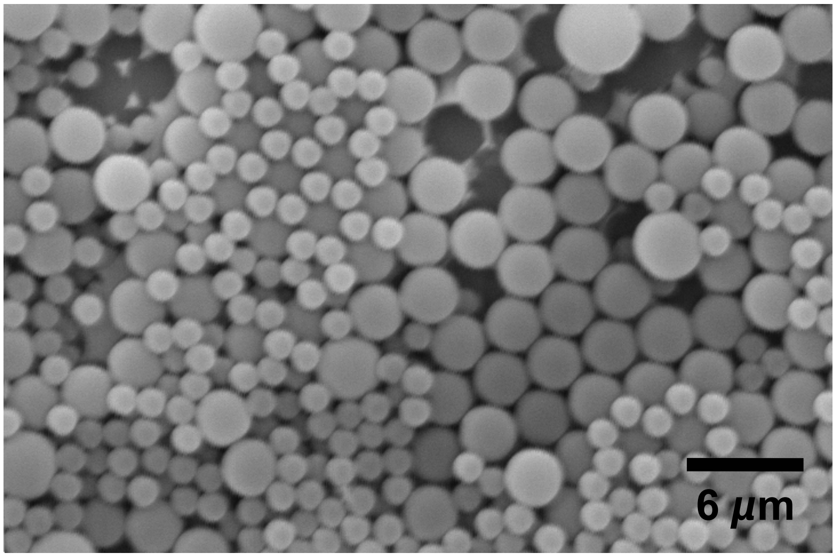

Figure 6.11 SEM images of the NSL/RIE patterned surface upon which a bidisperse population of spheres has been deposited. 2.8-μm spheres were first allowed to crystallize into the templated spherical sites, which were followed by the deposition of 1.4-μm spheres. It can be seen that the bottom colloidal crystal layer is templating the 1.4-μm spheres into a graphite-like structure as also observed in Fig. 6.6

6.5 Summary

We have described a simple approach to colloidal surface patterning that is both fast and versatile. Since this approach relies on dewetting from a lithographically templated surface, it is general in terms of colloid size and material, and thus yields colloidal crystal microarrays and structured superlattices of any desired composition. Microarray deposition occurs in minutes, so high throughput fabrication is possible. Furthermore, since the contents of each array of microwells are dependent upon the contents of the μL-scale drop of colloidal suspension placed above it, multiple compositions could be included on a single chip, which is not possible using other immersion-based deposition techniques. For example, a single-chip size-staged array (with colloidal crystals containing different sizes of spheres in each 10 × 10 array of microwells) could serve as an interesting addressable photonic film through replication with a polymer,[147] or even as a multichannel size-selective membrane for microfiltration applications. While the domain sizes and polycrystallinity of the microarrays will clearly limit the utility of this approach for fabricating high-quality photonic devices, its ability to quickly form addressable multicomponent arrays with controlled structure and size could reasonably be exploited for optical and sensing applications that are defect-tolerant.

CHAPTER VII

GENERAL CONCLUSIONS

This dissertation has described our development of solution-mediated synthetic techniques to access nanocrystalline alloy and intermetallic compounds, as well as our novel approach to the template-directed self-assembly of spherical colloids. The nanomaterials we have synthesized are dispersible in solution, and accordingly may be used with known solution processing techniques such as spin-coating and template directed assembly. As devices continue to shrink, these nanomaterials may be highly relevant for technological development. The synthetic methods we developed and described herein comprise a solid-state reaction toolbox that allows us to rationally design experiments and predict reaction products in some of the proof-of-concept systems studied. Hopefully, future research will show this reaction toolbox to be applicable to a wider range of solids. This is a significant advance for the solid-state chemist, as few rational and predictable synthetic methods to access inorganic compounds have been reported, and such knowledge may lead to the property-tailored synthesis of desirable materials.

In the course of these studies, three main synthetic techniques have shown utility for the facile, low-temperature synthesis of nanocrystalline alloy and intermetallic materials from solution. In each case, we show that materials with useful chemical and physical properties can be accessed, several of which have previously been shown to have size-dependent properties. We have shown that nanocrystalline composites and alloys can be formed in solution via the nanocomposite method. We show that this method provides good control over the composition of the final product, as determined by powder XRD. We also show that the composition and structure of the final product can be influenced significantly by the surface stabilizing agent used. Specifically, PSS and PVP stabilizers produce phase-separated nanocomposites, PEO, PEG and P2E2O appear to produce single-phase alloys (within the resolution of the X-ray diffraction data). Upon annealing, the latter three stabilizing agents produce materials with compositions closest to the nominal stoichiometry. These materials have exhibited good catalytic activity for the synthesis of vinyl acetate (VA) from acetic acid and ethylene, the direct synthesis of H_2O_2 from H_2 and O_2 gases,[47] and CO oxidation. We have shown that our nanomaterials can be supported, an important feature for heterogenous catalysts, and these supported materials show higher catalytic activity for VA synthesis than when unsupported.

Nanocrystalline Au-Pd materials can also be produced by the modified polyol method. Au and Pd chloride salts can be co-reduced by $NaBH_4$ at room temperature in high-boiling glycol solutions, and refluxing these solution after reduction yields single-phase alloy materials. The solvent used has been observed to affect the final product, as diethyleneglycol produced more Au rich alloys, while triethyleneglycol produced alloys much closer to the nominal stoichiometry of $AuPd_4$. We have also determined that the use of the polymeric surface stabilizer PVP promotes alloy formation in agreement with other literature reports.[88]

Our modified polyol method has also been very successful for the synthesis of nanocrystalline binary intermetallic compounds.[48] We have produced several Sn-based intermetallics with transition metals (Au, Ag, Co, Cu, Fe, Ni), as well as several Pt-based intermetallics with main-group metals (Bi, Pb, Sb, Sn). Many of the Sn-based intermetallics have properties which are technologically relevant, and may be useful materials for magnetic, superconducting, and battery anode applications.[22,60,95-97] Likewise, the Pt-based intermetallics have shown great promise as catalytic materials, showing improved activity and poisoning resistance compared to pure Pt.[4] In addition, both CoSb and $CoSb_3$ can be synthesized as nanocrystals, and the latter compound is a known thermoelectric material with size-dependent properties.[31] Because the modified polyol method is a low-temperature process, it can be useful for producing new and metastable compounds.[42,45] During the synthesis of $FeSn_2$, we have shown that we can isolate an unknown crystalline intermediate. Although we have been unable to determine the structure of the intermediate, the fact that we can routinely produce the intermediate seemingly phase-pure is a testament to the utility of our modified polyol process in the formation of new and low-temperature phases.

The third method, the organometallic route, was developed to address the problem that our modified polyol process is not compatible with highly electropositive metals. In order to overcome this problem, the organometallic route utilizes zero-valent organometallic reagents which require no reduction prior to integration into an intermetallic compound. We became interested in Zn-based intermetallic compounds with structural,[61] shape-memory,[65-67] and catalytic properties.[68,69] By reacting appropriate zero-valent organometallic or metal salt reagents with Zn(0) organometallic precursors (Et_2Zn or Ph_2Zn), we have successfully formed several *M*-Zn (*M* = Au, Cu, Pd) intermetallic compounds.[77] These compounds were created using conversion chemistry in which elemental *M* nanoparticle precursors were synthesized first, then reacted *in-situ* with Et_2Zn or Ph_2Zn. TEM studies of the single-metal precursors and final *M*-Zn intermetallics show that while particles sizes grow as expected, morphology may be preserved in the course of the conversion. This method can also allow for nice control over particle size and morphology,[2,111-114] which accordingly may translate to shape- and size- controlled intermetallic nanocrystals.

Extending the conversion chemistry we have established, we show that structurally complex nanocrystals can serve as reactive precursors.[80] Initial results indicated that PtSn nanocrystals may be converted to nanocrystalline $PtSn_2$ via reaction with Sn^{2+} in a glycol solution. It is important to note that this conversion occurs through a traditional polyol process without the aid of added surface stabilizers or reducing agents. We also show that PtSn can be reacted with Pt^{4+} to form Pt_3Sn, a compound that we had previously been unable to make directly using our modified polyol process. More surprisingly, we find that these reactions are cyclic; nanocrystalline $PtSn_2$ powders formed from PtSn can be isolated, analyzed, and then dispersed in solution and reacted with Pt^{4+} to yield PtSn. This reaction can also reversibly convert PtSn to Pt_3Sn. In addition, we show that this process can be used to convert AuCu to $AuCu_3$. Ni_3Sn_2 may also be converted to Ni_3Sn_4, however the reaction requires reduction with $NaBH_4$. These results show that this conversion of structurally complex nanocrystalline precursors is more general that we anticipated.

In order to efficiently use nanomaterials in devices, strategies are needed to control their self-assembly. With this in mind, we have developed a simple and robust approach to colloidal assembly using μm scale polystyrene and silica spheres.[81] By dropcoating colloidal suspensions onto lithographically templated square wells followed by controlled dewetting, we have formed free-standing two-dimensional close-packed colloidal crystal building blocks. In addition, we can use epitaxial templates to form interesting structures with a monodisperse particle population, and even more interesting colloidal crystal structures can be formed with a bidisperse particle population. We have also shown that nanosphere lithography may be combined with reactive ion etching to create an epitaxial template which can produce interesting bidisperse colloidal crystal structures. Overall, our template-directed self-assembly can allow for rapid crystallization, which is useful for quickly screening both the optimal deposition conditions and the feasibility of surface template libraries and sphere sizes for generating desired surface structures and superlattices.

The breadth of the synthetic work presented in this dissertation has several important implications. The methods we have developed show that nanocrystalline alloy and intermetallic compounds can be formed quickly in solution at low temperatures. These compounds cover a diverse range of elements and many have known useful chemical and physical properties. We have shown that they have catalytically active surface chemistries, and that they can be supported for use at heterogeneous catalysts.

Exquisite control over single-metal nanocrystal shape and size can be achieved using both the polyol[34,36,39-42] and organometallic routes,[2,111-114] and through the conversion chemistry we have established, shape- and size-controlled alloy and intermetallic nanocrystals may be accessible. Such an accomplishment would provide access to a wide range of nanomaterials for advanced technological applications and would also facilitate careful size-, shape-, and structure-dependent studies of many important physical phenomena. Finally, continued studies may lead to the marriage of our synthetic and template-directed self-assembly developments, making our nanocrystalline materials viable for integration into new technologies and devices.

REFERENCES

1. Hambrock, J.; Schröter, M. K.; Birkner, A.; Wöll, C.; Fischer, R. A. *Chem. Mater.* **2003**, *15*, 4217-4222.

2. Sun, S.; Murray, C. B.; Weller, D.; Folks, L.; Moser, A. *Science* **2000**, *287*, 1989-1992.

3. Sun, S.; Anders, S.; Thomson, T.; Baglin, J. E. E.; Toney, M. F.; Hamann, H. F.; Murray, C. B.; Terris, B. D. *J. Phys. Chem. B* **2003**, *107*, 5419-5425.

4. (a) Casado-Rivera, E.; Gal, Z.; Angelo, A. C. D.; Lind, C.; DiSalvo, F. J.; Abruna, H. D. *Chem. Phys. Chem.* **2003**, *4*, 193-199; (b) Casado-Rivera, E.; Volpe, D. J.; Alden, L.; Lind, C.; Downie, C.; Vazquez-Alvarez, T.; Angelo, A. C. D.; DiSalvo, F. J.; Abruna, H. D. *J. Am. Chem. Soc.* **2004**, *126*, 4043-4049; (c) Oana, M.; Hoffmann, R.; Abruna, H. D.; DiSalvo, F. J. *Surf. Sci.* **2005**, *574*, 1-16.

5. Shevchenko, E. V.; Talapin, D. V.; Schnablegger, H.; Kornowski, A.; Festin, Ö.; Svedlindh, P.; Hasse, M.; Weller, H. *J. Am. Chem. Soc.* **2003**, *125*, 9090-9101.

6. (a) Burda, C.; Chen, X.; Narayanan, R.; El-Sayed, M. A. *Chem. Rev.* **2005**, *105*, 1025-1102. (b) Eustis, S.; El-Sayed, M. A. *Chem. Soc. Rev.* **2006**, *35*, 209-217. (c) Orendorff C. J.; Sau T. K.; Murphy C. J. *Small* **2006**, *2*, 636-639.

7. (a) Kagan, C. R.; Murray, C. B.; Bawendi, M. G. *Science*, **1995**, *270*, 1335-1338. (b) Collier, C. P.; Saykally, R. J..; Shang, J. J.; Henrichs, S. E.; Heath, J. R. *Science* **1997**, *277*, 1978-1981. (c) Redi, F. X.; Cho, K.-S.; Murray, C. B.; O’Brien, S. *Nature* **2003**, *423*, 968-971.

8. (a) Ozin, G. A.; Yang, S. M. *Adv. Funct. Mater.* **2001**, *11*, 95-104. (b) Arsenault, A. C.; Miguez, H.; Kitaev, V.; Ozin, G. A.; Manners, I. *Macromol. Symp.* **2003**, *196*, 63-69.

9. (a) Schubert, M. M.; Kahlich, M. J.; Feldmeyer, G.; Huttner, M.; Hackenberg, S.; Gasteiger, H. A.; Behm, R. J. *Phys. Chem. Chem. Phys.* **2001**, *3*, 1123-1131. (b) Dupont, C.; Jugnet, Y.; Loffreda, D. *J. Am. Chem. Soc.* **2006**, *128*, 9129-9136.

10. Stowell, C. A.; Korgel, B. A. *Nano Lett.* **2005**, *5*, 1203 -1207.

11. (a) Narayanan, R.; El-Sayed, M. A. *J. Am. Chem. Soc.* **2004**, *126*, 7194-7195. (b) Narayanan, R.; El-Sayed, M. A. *Nano Lett.* **2004**, *4*, 1343-1348.

12. Muralidhar, G.; Massoth, F. E.; Shabtai, J. *J. Catal.* **1984**, *85,* 44-52.

13. Koch, C. C.; Whittenberger, J. D. *Intermetallics* **1996**, *4*, 339-355.

14. (a)Bai-Lin, Yu.; Xin-Feng, T.; Qiong, Q.; Qing-Jie, Z. *Acta Physica Sinica* **2004**, *53*, 3130-3135; (b) Xie, J.; Zhao, X.B.; Cao, G.S.; Zhao, M.J.; Su, S.F. *J. Power Sources* **2005**, *140*, 350–354.

15. Pithawalla, Y. B.; El-Shall, M. S.; Deevi, S. *Scripta Mater.* **2003**, *48*, 671-676.

16. (a) Onda, A.; Komatsu, T.; Yashima, T. *J. Catal.* **2001**, *201*, 13-21; (b) Komatsu, T.; Inaba, K.; Uezono, T.; Onda, A.; Yashima, T. *Appl. Cat. A* **2003**, *251*, 315-326; (c) Onda, A.; Komatsu, T.; Yashima, T. *J. Catal.* **2003**, *221*, 378-385.

17. Hobbs, K. L.; Larson, P. R.; Lian, G. D.; Keay, J. C.; Johnson, M. B. *Nano Lett.* **2004**, *4*, 167 -171.

18. Moison, J. M.; Houzay, F.; Barthe, F.; Leprince, L.; André, E.; Vatel, O. *Appl. Phys. Lett.* **1994**, *64*, 196-198.

19. (a) Heinrichs, B.; Delhez, P.; Schoebrechts, J. P.; Pirard, J. P. *J. Catal.* **1997**, *172*, 322-335. (b) Guczi, L.; Borko, L.; Schay, Z.; Bazin, D.; Mizukami, F. *Catal. Today* **2001**, *65*, 51-57. (c) Hutlova, A.; Niznansky, D.; Rehspringer, J. L.; Estournes, C.; Kurmoo, M. *Adv. Mater.* **2003**, *15*, 1622-1625.

20. Wright, J. D.; Sommerdijk, A. J. M. *Sol-Gel Materials: Chemistry and Applications*; Gordon and Breach: Amsterdam, 2001.

21. (a) Heibel, M.; Kumar, G.; Wyse, C.; Bukovec, P.; Bocarsly, A. B. *Chem. Mater.* **1996**, *8*, 1504-1511; (b) Vondrova, M.; Majsztrik, P. W.; Gould, S.; Bocarsly, A. B. *Chem. Mater.* **2005**, *17*, 4755-4757.

22. Rehbein, M.; Epple, M.; Fischer, R. D. *Solid State Sci.* **2000**, *2*, 473-488

23. Bahnemann, D. W.; Kormann, C.; Hoffman, M. R. *J. Phys. Chem.* **1987**, *91*, 3789-3798.

24. Wagner, R. S.; Ellis, W. C. *Appl. Phys. Lett.* **1964**, *4*, 89-90.

25. Liu, C. T. *Mater. Chem. Phys.* **1995**, *42*, 77-86.

26. (a) Morelli, D. T.; Caillat, T.; Fleurial, J.-P.; Borshchevsky, A.; Vandersande, J.; Chen, B.; and Uher, C. *Phys. Rev. B* **1995**, *51*, 9622-9628; (b) Sharp, J.W.; Jones, E.C.; Williams, R. K.; Martin, P.M.; B.C. Sales. *J. Appl. Phys.* **1995**, *78*, 1013-1018.

27. Ullakko, K.; Huang, J. K.; Kantner, C.; O’Handley, R. C.; Kokorin, V. V. *Appl. Phys. Lett.* **1996**, *69*, 1966-1968.

28. (a) Cava, R.J.; Takagi, H.; Batlogg, B.; Zandbergen, H.W.; Krajewski, J.J.; Peck, W.F.; Vandover, R.B.; Felder, R.J.; Siegrist, T.; Mizuhashi, K.; Lee, J.O.; Eisaki, H.; Carter, S.A.; Uchida, S. *Nature* **1994**, *367*, 146-148; (b) He, T.; Huang, Q.; Ramirez, A.P.; Wang, Y.; Regan, K.A.; Rogado, N.; Hayward, M.A.; Haas, M.K.; Slusky, J.S.; Inumara, K.; Zandbergen, H.W.; Ong, N.P.; Cava, R.J. *Nature* **2001**, *411*, 54-56.

29. (a) Kirchheim, R.; Mutschele, T.; Keininger, W.; Gleiter, H.; Birringer, R.; Koble, T. D. *Mater. Sci. Eng.* **1988**, *99*, 457-462; (b) Kamakoti, P.; Sholl, D. S. *J. Membrane Sci.* **2003**, *225*, 145-154.

30. Kuncser, V.; Doi, M.; Sahoo, B.; Stromberg, F.; Keune, W. *J. Appl. Phys.* **2003**, *94*, 3573-3581.

31. Toprak, M. S.; Stiewe, C.; Platzek, D.; Williams, S.; Bertini, L.; Müller, E., Gatti, Zhang, Y.; Rowe, M.; Muhammed, M. *Adv. Funct. Mat.* **2004**, *14*, 1189-1196.

32. West, A. R. *Solid State Chemistry and Its Applications*; Wiley: Chichester, England, 1984.

33. Williams, J. R.; Johnson, D. C. *Inorg. Chem.* **2002**, *41*, 4127-4130.

34. Wiley, B.; Sun, Y.; Mayers, B.; Xia, Y. *Chem. Eur. J.* **2005**, *11*, 454-463.

35. Sra, A. K.; Ewers, T. D.; Schaak, R. E. *Chem. Mater.* **2005**, *17*, 758-766.

36. Sun, Y.; Mayers, B.; Herricks, T.; Xia, Y. *Nano Lett.* **2003**, *3*, 955-960.

37. Seo, W. S.; Shim, J. H.; Oh, S. J.; Lee, E. K.; Hur, N. H.; Park, J. T. *J. Am. Chem. Soc.* **2005**, *127*, 6188-6189.

38. Park, J.; Lee, E.; Hwang, N.-M.; Kang, M.; Kim, S. C.; Hwang, Y.; Park, J.-G.; Noh, H.-J.; Kim, J.-Y.; Park, J.-H.; Hyeon, T. *Angew. Chem. Int. Ed.* **2005**, *44*, 2872-2877.

39. Hoefelmeyer, J. D.; Niesz, K.; Somorjai, G.; Tilley, T. D. *Nano Lett.* **2005**, *5*, 435-438.

40. Kim, F.; Connor, S.; Song, H.; Kuykendall, T.; Yang, P. *Angew. Chem. Int. Ed.* **2004**, *43*, 3673-3677.

41. Sun, Y.; Wiley, B.; Li, Z.-Y.; Xia, Y. *J. Am. Chem. Soc.* **2004**, *126*, 9399-9406.

42. Chou, N. H.; Schaak, R. E. *J. Am. Chem. Soc.* **2007**, *129*, 7339-7345.

43. Dinega, D. P.; Bawendi, M. G. *Angew. Chem. Int. Ed.* **1999**, *38*, 1788-1791.

44. Zhao, Y.; Zhang, Y.; Zhu, H.; Hadjipanayis, G. C.; Xiao, J. Q. *J. Am. Chem. Soc.* **2004**, *126*, 6874-6875.

45. (a) Leonard, B. M.; Bhuvanesh, N. S. P.; Schaak, R. E. *J. Am. Chem. Soc.* **2005**, *127*, 7326-7327. (b) Leonard, B. M.; Schaak, R. E. *J. Am. Chem. Soc.* **2006**, *128*, 11475-11482.

46. (a) Kurihara, L. K.; Chow, G. M.; Schoen, P.E. *Nanostruct. Mater.* **1995**, *5*, 607-613; (b) Chow, G. M.; Kurihara, L. K.; Kemner, K. M.; Schoen, P. E.; Elam, W. T.; Ervin, A.; Keller, S.; Zhang, Y. D.; Budnick, J.; Ambrose, T. J. *Mater. Res.* **1995**, *10*, 1546-1554; (c) Yin, H.; Chow, G. M. J. *Mater. Res.* **2003**, *18*, 180-187.

47. Schaak, R. E.; Sra, A. K.; Leonard, B. M.; Cable, R. E.; Bauer, J. C.; Han, Y.-F.; Means, J.; Teizer, W.; Vasquez, Y.; Funck, E. S. *J. Am. Chem. Soc.* **2005**, *127*, 3506-3515.

48. Cable, R. E.; Schaak, R. E. *Chem. Mater.* **2005**, *17*, 6835-6841.

49. Sra, A. K.; Schaak, R. E. *J. Am. Chem. Soc.* **2004**, *126*, 6667-6672.

50. Teng, X.; Yang, H. J. *J. Am. Chem. Soc.* **2003**, *125*, 14559-14563.

51. Firth, J. G. *Trans. Faraday Soc.* **1966**, *62*, 2566-2576.

52. Rylander, P. N. *Catalytic Hydrogenation in Organic Synthesis*; Academic Press: London, 1979.

53. Venezia, A. M.; La Parola, V.; Nicloli, V.; Deganello, G. *J. Catal.* **2002**, *212*, 56-62.

54. Nakamura, S.; Yasui, T. *J. Catal.* **1971**, *23*, 315-320.

55. National Library of Medicine HSDB, *Vinyl Acetate (CASRN: 108-05-4)*, http://toxnet.nlm.nih.gov/cgi-bin/sis/search/f?./temp/~Enmjxs:1:manf (accessed 09/12/2007).

56. (a) Fievet, F.; Lagier, J.P.; Blin, B.; Beaudoin, B.; Figlarz, M. *Solid State Ionics* **1989**, *32/33*, 198-205; (b) Ducamp-Sanguesa, C.; Herrera-Urbina, R.; Figlarz, M. *Solid State Ionics* **1993**, *63-65*, 25-30.

57. (a) Toshima, N.; Kushihashi, K.; Yonezawa, T.; Hirai, H. *Chem. Lett.* **1989**, *10*, 1769-1772; (b) Toshima, N.; Harada, M.; Yamazaki, Y.; Asakura, K. J. *Phys. Chem.* **1992**, *96*, 9927-9933; (c) Toshima, N.; Yonezawa, T. *New J. Chem.* **1998**, 1179-1201.

58. (a) Murray, C. B.; Kagan, C. R.; Bawendi, M. G. *Annu. Rev. Mater. Sci.* **2000**, *30*, 545-610; (b) Murray, C. B.; Sun, S.; Gaschler, W.; Doyle, H.; Betley, T. A.; Kagan, C. R. *IBM J. Res. Dev.* **2001**, *45*, 47-56.

59. Teng, X.; Yang, H. *Nano Lett.* **2005**, *5*, 885-891.

60. Amadei, I.; Panero, S.; Scrosati, B.; Cocco, G.; Schiffini, L. *J. Power Sources* **2005**, *143*, 227–230.

61. Budinski, K. G. *Engineering Materials: Properties and Selection*, 4th ed.; Prentice Hall: Englewood Cliffs, NJ, 1992; pp 603-608.

62. (a) Iwasa, N.; Masuda, S.; Ogawa, N.; Takezawa, N. *Appl. Catal. A* **1995**, *125*, 145-157. (b) Iwasa, N.; Mayanagi, T.; Masuda, S.; Takezawa, N. *React. Kinet. Catal. Lett.* **2000**, *69*, 355-360. (c) Karim, A.; Conant, T.; Datye, A. *J. Catal.* **2006**, *243*, 420-427.

63. Fujitani, T.; Nakamura, J. *Appl. Catal. A* **2000**, 191, 111-129.

64. Liu, L.; Tian, H.; Xie, S.; Zhou, W.; Mu, S.; Song, L.; Liu, D.; Luo, S.; Zhang, Z.; Xiang, Y.; Zhao, X.; Ma, W.; Shen, J.; Li, J.; Wang, C.; Wang, G. *J. Phys. Chem. B* **2006**, *110*, 20158-20165.

65. Beck, A.; Jan, J. P.; Pearson, W. B.; Templeton, I. M. *Philos. Mag.* **1963**, *8*, 351.

66. Pops, H.; Massalski, T. B. *T. Metall. Soc. AIME* **1965**, *233*, 728.

67. Hisatsune, K.; Takuma, Y.; Tanaka, Y.; Udoh, K.; Morimura, T.; Hasaka, M. *Sol. St. Commun.* **1998**, *106*, 509-512.

68. (a) Ding, C.; Jihua, C.; Hongge, Y.; Zhenhua, C. *Mater. Sci. Eng. A* **2007**, *444*, 1-5. (b) Andrade-Gamboa, J.; Gennari, F. C.; Arneodo Larochette, P.; Neyertz, C.; Ahlers, M.; Pelegrina, J. L. *Mater. Sci. Eng. A* **2007**, *447*, 324-331.

69. Penner, S.; Jenewein, B.; Gabasch, H.; Klötzer, B.; Wang, D.; Knop-Gericke, A.; Schlögl, R.; Hayek, K. *J. Catal.* **2006**, *241*, 14-19.

70. Jušėkėnas, R.; Pakštas, V.; Sudavičius, A.; Kapočius, V.; Karpavičienė, V. *Appl. Surf. Sci.* **2004**, *229*, 402-408.

71. Suzuki, N.; Ito, S. *J. Phys. Chem. B* **2006**, *110*, 2048-2086.

72. Tkachenko, O.P.; Stakheev, A. Y.; Kustov, L. M.; Mashkovsky, I. V.; van den Berg, M.; Grünert, W.; Kozitsyna, N. Y.; Dobrokhotova, Z. V.; Zhilov, V. I.; Nefedov, S. E.; Vargaftik, M. N.; Moiseev, I. I. *Catal. Lett.* **2006**, *112*, 155-161.

73. (a) Bogdanović, B.; Claus, K. -H.; Gürtzen, S.; Spliethoff, B.; Wilczok, U. *J. Less-Common Met.* **1987**, *131*, 163-172. (b) Abe, O.; Tsuge, A. *J. Mater. Res.* **1991**, *6*, 928-934. c) Jones, D. J.; Rozière, J.; Aleandri, L. E.; Bogdanović, B.; Huckett, S. C. *Chem. Mater.* **1992**, *4*, 620-625. (d) Schwab, S. T.; Paul, P. P.; Pan, Y. -M. *Mater. Sci. Eng.* **1995**, *A202*, 197-200. (e) Lu, Q.; Hu, J.; Tang, K.; Qian, Y.; Zhou, G.; Liu, X. *Solid State Ionics* **1999**, *124*, 317-321. (f) Damle, C.; Gopal, A.; Sastry, M. *Nano. Lett.* **2002**, *2*, 365-368. (g) Pithawalla, Y. B.; Deevi, S. *Mater. Res. Bull.* **2004**, *39*, 2303-2316. (h) Ma, J.; Du, Y. *J. Alloy Compd.* **2005**, *395*, 277-279.

74. Haber, J. A.; Gunda, N. V.; Balbach, J. J.; Conradi, M. S.; Buhro, W. E. *Chem. Mater.* **2000**, *12*, 973-982.

75. Bönnemann, H.; Brijoux, W.; Hofstadt, H. -W.; Ould-Ely, T.; Schmidt, W.; Waßmuth, B.; Weidenthaler, C. *Angew. Chem. Int. Ed.* **2002**, *41*, 599-603.

76. Cokoja, M.; Parala, H.; Schröter, M.-K.; Birkner, A.; van den Berg, M. W. E.; Grünert, W.; Fischer, R. A. *Chem. Mater.* **2006**, *18*, 1634-1642.

77. Cable, R. E.; Schaak, R. E. *Chem. Mater.* **2007**, *19*, 4098-4104.

78. (a) Henkes, A. E.; Vasquez, Y.; Schaak, R. E. *J. Am. Chem. Soc.* **2007**, *129*, 1896-1897.

79. Chiang, R.-K.; Chiang, R.-T. *Inorg. Chem.* **2007**, *46*, 369-371.

80. Cable, R. E.; Schaak, R. E. *J. Am. Chem. Soc.* **2006**, *128*, 9588-9589.

81. Schaak, R. E.; Cable, R. E.; Leonard, B. M.; Norris, B. C. *Langmuir* **2004**, *20*, 7293-7297.

82. (a) Guczi, L.; Beck, A.; Horvath, A.; Koppany, Zs.; Stefler, F.; Frey, K; Sajo, I.; Geszti, O.; Bazin, D.; Lynch, J. *J. Molec. Catal. A* **2003**, *204-205*, 545-552. (b) Yang, Y.; Saoud, K. M.; Abdelsayed, V.; Glaspell, G.; Deevi, S.; El-Shall, M. S. *Catal. Commun.* **2006**, *7*, 281-284.

83. Han, Y.-F.; Wang, J.-H.; Kumar, D.; Yan, Z.; Goodman, D. W. *J. Catal.* **2005**, *232*, 467-475.

84. Han, Y.-F.; Kumar, D.; Sivadinarayana, C.; Clearfield, A.; Goodman, D. W. *Catal. Lett.* **2004**, *94*, 131-134.

85. Chen, M.; Kumar, D.; Yi, C.-W.; Goodman, D. W. *Science* **2005**, *310*, 291-293.

86. Chinta, S.; Lunsford, J. H. *J. Catal.* **2004**, *225*, 249-255.

87. Villars, P., Calvert, L. D., Eds. *Pearson's Handbook of Crystallographic Data for Intermetallic Phases*, 2nd ed.; ASM International: Materials Park, OH, 1991.

88. Vasquez, Y.; Sra, A. K.; Schaak, R. E. *J. Am. Chem. Soc.* **2005**, *127*, 12504-12505.

89. Hirai, H.; Nakao, Y.; Toshima, N. *J. Macromol. Sci.-Chem.* **1979**, *A13*, 727-750.

90. Nagai, A.; Takahashi, A.; Komatsu, T.; Nakagawa, T. *Polymer J.* **1988**, *20*, 609-614.

91. Dissanayake, D. P.; Lunsford, J. H. *J. Catal.* **2002**, *206*, 173-176.

92. Han, Y.-F.; Lunsford, J. H. *Catal. Lett.* **2005**, *230*, 313-316.

93. (a) Turkevich, J.; Hillier, J.; Stevenson, P. C. *Disc. Faraday Soc.* **1951**, *11*, 55-75. (b) Frens, G. *Nature Phys. Sci.* **1973**, *241*, 20-22.

94. (a) Grover, G. S.; Chaudhari, R. V. *Chem Eng. J.* **1986**, *32*, 93-99. (b) Macleod, N.; Keel, J. M.; Lambert, R. M. *Appl. Catal. A* **2004**, *261*, 37-46.

95. (a) Sauthoff, G. *Intermetallics*; Wiley: New York, 1995. (b) Cahn, R. W. *Contemp. Phys.* **2001**, *42*, 365-375.

96. Orlando, T. P.; McNiff, E. J.; Foner, S.; Beasley, M. R. *Phys. Rev. B* **1979**, *19*, 4545-4561.

97. Van Dover, R. B.; Gyorgy, E. M.; Cava, R. J.; Krajewski, J. J.; Felder, R. J.; Peck, W. F. *Phys. Rev. B* **1993**, *47*, 6134-6137.

98. Mitzi, D. B.; Kosbar, L. L.; Murray, C. E.; Copel, M.; Afzali, A. *Nature* **2004**, *428*, 299-303.

99. Hamilton, D. C.; Raub, C. J.; Matthias, B. T.; Corenzwit, E.; Hull, G. W. *J. Phys. Chem. Solids* **1965**, *26*, 665-667.

100. *Binary Alloy Phase Diagrams*; Massalski, T. B., Ed.; ASM International: Materials Park, OH, 1996.

101. Song, S.Q.; Zhou, W.J.; Zhou, Z.H.; Jiang, L.H.; Sun, G.Q.; Xin, Q.; Leontidis, V.; Kontou, S., Tsiakaras, P. *Int. J. Hydrogen Energy* **2005**, *30*, 995-1001.

102. Hauser, J. J.; Theuerer, H. C.; Werthamer, N. R. *Phys. Rev.* **1964**, *136*, A637-A641.

103. Wells, S.; Charles, S. W.; MØrup, S.; Linderoth, S.; van Wonterghem, J.; Larsen, J.; Madsen, M. B. *J. Phys.: Condens. Matter* **1989**, *1*, 8199-8208.

104. Themlin, J.-M.; Chtaïb, M.; Henrard, L.; Lambin, P.; Darville, J.; Gilles, J.-M. *Phys. Rev. B* **1992**, *46*, 2460-2466.

105. Guo, Q.; Teng, X.; Yang, H. *Adv. Mater.* **2004**, *16*, 1337-1341.

106. Sehayek, T.; Lahav, M.; Popovitz-Biro, R.; Vaskevich, A.; Rubinstein, I. *Chem. Mater.* **2005**, *17*, 3743-3748.

107. Jiang, P.; Bertone, J. F.; Colvin, V. L. *Science* **2001**, *291*, 453-457.

108. Caruso, F. *Chem. Eur. J.* **2000**, *6*, 413-419.

109. (a) Birringer, R. *Mater. Sci. Eng. A* **1989**, *117*, 33-43. (b) Gleiter, H. *Prog. Mater. Sci.* **1989**, *33*, 223-315.

110. Gates, B.; Wu, Y. Y.; Yin, Y. D.; Yang, P. D.; Xia, Y. N. *J. Am. Chem. Soc.* **2001**, *123*, 11500-11501.

111. (a) Puntes, V. F.; Zanchet, D.; Erdonmez, C. K.; Alivisatos, A. P. *J. Am. Chem. Soc.* **2002**, *124*, 12874-12880. (b) Chaudret, B. *C. R. Phys.* **2005**, *6*, 117-131.

112. (a) Hou, Y.; Gao, S. *J. Mater. Chem.* **2003**, *13*, 1510-1512. (b) Shao, H.; Huang, Y.; Lee, H.-S.; Suh, Y. J.; Kim, C.-O. *J. Appl. Phys.* **2006**, *99*, 08N702. (c) Wu, H. P.; Ge, M. Y.; Yao, C. W.; Wang, Y. W.; Zeng, Y. W.; Wang, L. N.; Zhang, G. Q.; Jiang, J. Z. *Nanotechnology* **2006**, *17*, 5339-5343.

113. Hambrock, J.; Becker, R.; Birkner, A.; Weiß, J.; Fischer, R. A. *Chem. Commun.* **2002**, 68-69.

114. Hiramatsu, H.; Osterloh, F. E. *Chem. Mater.* **2004**, *16*, 2509-2511.

115. (a) Clarke, T. G.; Hampson, N. A.; Lee, J. B.; Morley, J. R.; Scanlon, B. *Tetrahedron Lett.* **1968**, *54*, 5685-5688. (b) Capdevielle, P.; Lavigne, A.; Sparfel, D.; Baranne-Lafont, J.; Cuong, N. K.; Maumy, M. *Tetrahedron Lett.* **1990**, *31*, 3305-3308.

116. Salzemann, C.; Lisiecki, I.; Urban, J., Pileni, M. P. *Langmuir* **2004**, *20*, 11772 – 11777.

117. (a) Tanori, J.; Pileni, M. P. *Langmuir* **1997**, *13*, 639-646. (b) Pileni, M. P.; Gulik-Krzywicki, T.; Tanori, J.; Filankembo, A.; Dedieu, J.C. *Langmuir* **1998**, *14*, 7359-7363. (c) Ren, X.; Chem, D.; Tang, F. *J. Phys. Chem. B* **2005**, *109*, 15803-15807. (d) Wang, Y.; Chen, P.; Liu, M. *Nanotech.* **2006**, *17*, 6000-6006. (e) Zhou, G.; Lu, M.; Yang, Z. *Langmuir* **2006**, *22*, 5900-5903.

118. Jana, N. R.; Gearheart, L.; Murphy, C. J. *Langmuir* **2001**, *17*, 6782-6786.

119. (a) Ullakko, K. *J. Mater. Eng. Perform.* **1996**, *5*, 405-409. (b) Huang, W. *Mater. Design* **2002**, *23*, 11-19. (c) Fu, Y.; Du, H.; Huang, W.; Zhang, S.; Hu, M. *Sensor. Actuat. A-Phys.* **2004**, *112*, 395-408.

120. McFadden, S. X.; Mishra, R. S.; Valiev, R. Z.; Zhilyaev, A. P.; Mukherjee, A. K. *Nature* **1999**, *398*, 684-686.

121. (a) Liu, C. T.; Stringer, J.; Mundy, J. N.; Horton, L. L.; Angelini, P. *Intermetallics* **1997**, *5*, 579-596. (b) Stoloff, N. S.; Liu, C. T.; Deevi, S. C. *Intermetallics* **2000**, *8*, 1313-1320.

122. (a) Brady, M. P.; Wrobel, S. K.; Lograsso, T. A.; Payzant, E. A.; Hoelzer, D. T.; Horton, J. A.; Walker, L. R. *Chem. Mater.* **2004**, *16*, 1984-1990. (b) Cheng, F. T.; Shi, P.; Man, H. C. *Mater. Lett.* **2005**, *59*, 1516-1520.

123. Yin, Y.; Rioux, R. M.; Erdonmez, C. K.; Hughes, S.; Somorjai, G. A.; Alivisatos, A. P. *Science* **2004**, *304*, 711-714.

124. Son, D. H.; Hughes, S. M.; Yin, Y.; Alivisatos, A. P. *Science* **2004**, *306*, 1009-1012.

125. Haber, J. A.; Gunda, N. V.; Balbach, J. J.; Conradi, M. S.; Buhro, W. E. *Chem. Mater.* **2000**, *12*, 973-982.

126. (a) Schlecht, S.; Budde, M.; Kienle, L. *Inorg. Chem.* **2002**, *41*, 6001-6005. (b) Schlecht, S.; Erk, C.; Yosef, M. *Inorg. Chem.* **2006**, *45*, 1693-1697.

127. Roychowdhury, C.; Matsumoto, F.; Mutolo, P. F.; Abruna, H.; DiSalvo, F. J. *Chem. Mater.* **2005**, *17*, 5871-5876.

128. Karkamkar, A. J.; Kanatzidis, M. G. *J. Am. Chem. Soc.* **2006**, *128*, 6002-6003.

129. (a) Li, Z.-Y.; Wang, J.; Gu, B.-Y. *Phys. Rev. B* **1998**, *58*, 3721-3729. (b) Xia, Y.; Gates, B.; Li, Z.-Y. *Adv. Mater.* **2001**, *13*, 409-413. (c) Yang, S. M.; Miguez, H.; Ozin, G. A. *Adv. Funct. Mater.* **2002**, *12*, 425-431.

130. Van Blaaderen, A.; Ruel, R.; Wiltzius, P. *Nature* **1997**, *385*, 321-324.

131. Velikov, K. P.; Christova, C. G.; Dullens, R. P. A.; van Blaaderen, A. *Science* **2002**, *296*, 106-109.

132. Bartlett, P.; Ottewill, R. H.; Pusey, P. N. *Phys. Rev. Lett.* **1992**, *68*, 3801-3804.

133. Jiang, P.; Bertone, J. F.; Hwang, K. S.; Colvin, V. L. *Chem. Mater.* **1999**, *11*, 2132-2140.

134. Kitaev, V.; Ozin, G. A. *Adv. Mater.* **2003**, *15*, 75-78.

135. Hayward, R. C.; Saville, D. A.; Aksay, I. A. *Nature* **2000**, *404*, 56-59.

136. Kim, E.; Xia, Y.; Whitesides, G. M. *J. Am. Chem. Soc.* **1996**, *118*, 5722-5731.

137. Yin, Y.; Lu, Y.; Gates, B.; Xia, Y. *J. Am. Chem. Soc.* **2001**, *123*, 8718-8730.

138. Yang, S. M.; Ozin, G. A. *Chem. Commun.* **2000**, 2507-2508.

139. (a) Aizenberg, J.; Braun, P. V.; Wiltzius, P. *Phys. Rev. Lett.* **2000**, *84*, 2997-3000. (b) Zheng, H.; Rubner, M. F.;Hammond,P. T. *Langmuir* **2002**, *18*, 4505-4510. (c) Lee, I.; Zheng, H.; Rubner, M. F.; Hammond, P. T. *Adv. Mater.* **2002**, *14*, 572-577.

140. Vlasov, Y. A.; Bo, X.-Z.; Sturm, J. C.; Norris, D. J. *Nature* **2001**, *414*, 289-293.

141. Hulteen, J. C.; Treichel, D. A.; Smith, M. T.; Duval, M. L.; Jensen, T. R.; Van Duyne, R. P. *J. Phys. Chem. B* **1999**, *103*, 3854-3863.

142. Stober, W.; Fink, A.; Bohn, E. *J. Colloid Interface Sci.* **1968**, *26*, 62.

143. Mazur, S.; Beckerbauer, R.; Buckholz, J. *Langmuir* **1997**, *13*, 4287.

144. Yin, Y.; Li, Z.-Y.; Xia, Y. *Langmuir* **2003**, *19*, 622-631.

145. Legtenber, R.; Jansen, H.; de Boer, M.; Elwenspoek, M. *J. Electrochem. Soc.* **1995**, *142*, 2020-2027.

146. Mansano, R. D.; Verdonck, P.; Maciel, H. S. *Sensors and Actuators A* **1998**, *65*, 180-186.

147. Jiang, P.; Huang, K. S.; Mittleman, D. M.; Bertone, J. F.; Colvin, V. L. *J. Am. Chem. Soc.* **1999**, *121*, 11630-11637.

VITA

Robert E. Cable

17821 Oak Forest Dr.
Tyler, TX 75762
rob.cable@gmail.com

EDUCATION

Ph.D., Chemistry, Texas A&M University, December 2007

B.A., Chemistry, Knox College, June 2002

PUBLICATIONS

Cable, R. E.; Schaak, R. E. *Chem. Mater.* **2007**, *19*, 4098-4104.

Cable, R. E.; Schaak, R. E. *J. Am. Chem. Soc.* **2006**, *128*, 9588-9589. [Featured in *Nature* "Research Highlights," July 27, 2006]

Henkes, A. E.; Bauer, J. C.; Sra, A. K.; Johnson, R. D.; Cable, R. E.; Schaak, R. E. *Chem. Mater.* **2006**, *18*, 567-571.

Cable, R. E.; Schaak, R. E. *Chem. Mater.* **2005**, *17*, 6835-6841.

Schaak, R. E.; Sra, A. K.; Leonard, B. M.; Cable, R. E.; Bauer, J. C.; Han, Y.-F.; Means, J.; Teizer, W.; Vasquez, Y.; Funck, E. S. *J. Am. Chem. Soc.* **2005**, *127*, 3506-3515.

Ewers, T. D.; Sra, A. K.; Norris, B. C.; Cable, R. E.; Cheng, C. H.; Shantz, D. F.; Schaak, R. E. *Chem. Mater.* **2005**, *17*, 758-766.

Schaak, R. E.; Cable, R. E.; Leonard, B. M.; and Norris, B. C. *Langmuir* **2004**, *20*, 7293-7297.

HONORS AND AWARDS

Outstanding Oral Presentation, IUCCP, Texas A&M University

President - Phi Lambda Upsilon Honorary Chemical Society, 2006-2007

Welch Fellowship Recipient, Texas A&M University Chemistry Dept.